

Analysis of Shear Wave Generation by Decoupled and Partially Coupled Explosions

Jeffrey L. Stevens
G. Eli Baker
Heming Xu

Science Applications International Corp.
10260 Campus Point Drive
San Diego, CA 92126

Final Report

31 July 2009

APPROVED FOR PUBLIC RELEASE; DISTRIBUTION IS UNLIMITED.



AIR FORCE RESEARCH LABORATORY
Space Vehicles Directorate
29 Randolph Rd
AIR FORCE MATERIEL COMMAND
HANSCOM AFB, MA 01731-3010

NOTICES

Using Government drawings, specifications, or other data included in this document for any purpose other than Government procurement does not in any way obligate the U.S. Government. The fact that the Government formulated or supplied the drawings, specifications, or other data does not license the holder or any other person or corporation; or convey any rights or permission to manufacture, use, or sell any patented invention that may relate to them.

This report was cleared for public release and is available to the general public, including foreign nationals. Qualified requestors may obtain copies of this report from the Defense Technical Information Center (DTIC) (<http://www.dtic.mil>). All others should apply to the National Technical Information Service.

AFRL-RV-HA-TR-2009-1061 HAS BEEN REVIEWED AND IS APPROVED FOR PUBLICATION IN ACCORDANCE WITH ASSIGNED DISTRIBUTION STATEMENT.

//signature//

ROBERT J. RAISTRICK
Contract Manager

//signature//

Domenic Thompson, Maj, USAF, Acting Chief
Battlespace Surveillance Innovation Center

This report is published in the interest of scientific and technical information exchange, and its publication does not constitute the Government's approval or disapproval of its ideas or findings.

REPORT DOCUMENTATION PAGE

Form Approved
OMB No. 0704-0188

Public reporting burden for this collection of information is estimated to average 1 hour per response, including the time for reviewing instructions, searching existing data sources, gathering and maintaining the data needed, and completing and reviewing this collection of information. Send comments regarding this burden estimate or any other aspect of this collection of information, including suggestions for reducing this burden to Department of Defense, Washington Headquarters Services, Directorate for Information Operations and Reports (0704-0188), 1215 Jefferson Davis Highway, Suite 1204, Arlington, VA 22202-4302. Respondents should be aware that notwithstanding any other provision of law, no person shall be subject to any penalty for failing to comply with a collection of information if it does not display a currently valid OMB control number. **PLEASE DO NOT RETURN YOUR FORM TO THE ABOVE ADDRESS.**

1. REPORT DATE (DD-MM-YYYY) 07-30-2009		2. REPORT TYPE Final Report		3. DATES COVERED (From - To) 01-25-2006 to 07-30-2009	
4. TITLE AND SUBTITLE Analysis of Shear Wave Generation by Decoupled and Partially Coupled Explosions				5a. CONTRACT NUMBER FA8718-06-C-0007	
				5b. GRANT NUMBER	
				5c. PROGRAM ELEMENT NUMBER 62601F	
6. AUTHOR(S) Jeffry L. Stevens, G. Eli Baker and Heming Xu				5d. PROJECT NUMBER 1010	
				5e. TASK NUMBER SM	
				5f. WORK UNIT NUMBER A1	
7. PERFORMING ORGANIZATION NAME(S) AND ADDRESS(ES) Science Applications International Corp. 10260 Campus Point Drive San Diego, CA 92126				8. PERFORMING ORGANIZATION REPORT NUMBER	
9. SPONSORING / MONITORING AGENCY NAME(S) AND ADDRESS(ES) Air Force Research Laboratory 29 Randolph Rd. Hanscom AFB, MA 01731-3010				10. SPONSOR/MONITOR'S ACRONYM(S) AFRL/RVBYE	
				11. SPONSOR/MONITOR'S REPORT NUMBER(S) AFRL-RV-HA-TR-2009-1061	
12. DISTRIBUTION / AVAILABILITY STATEMENT Approved for Public Release; Distribution Unlimited.					
13. SUPPLEMENTARY NOTES					
14. ABSTRACT We compare near field and local seismograms from partially and fully decoupled chemical and nuclear explosions, and water-filled cavity nuclear explosions, with seismograms from tamped explosions in the same source location, and compare records of a centered and an offset explosion in a spherical cavity, all to identify and characterize shear waves generated by decoupled explosions. We numerically model the shear wave generation due to hydrofracturing, opening of pre-existing cracks, asymmetric nonlinear deformation outside the cavity due to only partial decoupling, offset of the source within the cavity, ellipticity of the cavity, and a flat-floored cavity (due to recrystallization of melted salt), and compare the simulations with observations. We also model an offset source analytically to investigate the effect of longer lasting reverberations. The observations and modeling indicate that partially and fully decoupled explosions generate significant shear wave energy at the source through various source asymmetries, including offset of the source and aspherical cavity shape.					
15. SUBJECT TERMS Decoupled explosions, Explosion source generated shear waves					
16. SECURITY CLASSIFICATION OF:			17. LIMITATION OF ABSTRACT	18. NUMBER OF PAGES	19a. NAME OF RESPONSIBLE PERSON
a. REPORT UNC	b. ABSTRACT UNC	c. THIS PAGE UNC			SAR
19b. TELEPHONE NUMBER (include area code)					

Table of Contents

1. Summary.....	1
2. Introduction.....	1
3. Seismic Wave Generation by a Non-isotropic Explosion Source	3
3.1 Introduction.....	3
3.2 General solution for variable pressure applied to spherical cavity	4
3.3 Solution for an offset explosion source	5
3.4 Spherically symmetric calculation of the pressure field from an explosion in air....	6
3.5 Conservation of momentum.....	6
3.6 Variable arrival time	7
3.7 Variable amplitude.....	9
3.8 Axisymmetric calculation of an offset explosion in a cavity.....	10
3.9 Multiple reverberations	12
3.10 Discussion and Conclusions	16
4. SV Generation by a Vertically Offset Explosion in a Spherical Cavity.....	20
4.1 Introduction.....	20
4.2 Data	20
4.3 Analysis.....	22
4.4 Modeling.....	25
4.4.1 Shear wave generation by nonlinear deformation	25
4.4.2 Shear wave generation by reverberations within the cavity	27
4.5 Discussion and Conclusions	28
5. An Analysis of Shear Waves Generated by the Sterling Explosion	30
5.1. Introduction.....	30
5.2 Review of salt material properties	32
5.3 Numerical simulations of the Salmon explosion	33
5.4 Numerical simulation of the Sterling event	37
5.5 P and S spectra and waveforms from the Sterling event	40
5.6 Discussion and Conclusions	45
6. Generation of Shear Waves from Explosions in Water-Filled Cavities	46
6.1. Introduction.....	46
6.2 Data.....	47
6.3 Identification of shear waves in the records	49
6.4 Origin and Characteristics of the spectral peak	53
6.5 The spectral peak distinguishes whether S is scattered from P	54
6.6 Initial S travel time curve is consistent with source generation.....	55
6.7 Size and depth of the explosion S-wave source.....	56
6.8 Shear Wave Source Modeling	59
6.8.1 Introduction.....	59
6.8.2 Nonlinear Modeling of Source Asymmetries	59
6.8.3 Explosions within a spherical cavity.....	60
6.8.4 Asymmetrical cavity calculations	62
6.8.5 Fracture calculations	64
6.8.6 Analytic Offset source calculations	65
6.8.7 Point force, tangential data and more prominent S2.....	66

6.8.9 Summary of Conclusions from Calculations	68
6.9 Discussion	68
6.10 Conclusions.....	69
7. Israeli Oron Decoupling Explosions.....	70
7.1 Introduction: Source Parameters, Previous Work, and Local Spectra.....	70
7.2 Identifying the shear waves: Particle traces and record sections.....	73
7.3 Analysis of the P and S waves: P, SV, and SH spectra	83
7.4 Analysis of the P and S waves: Comparison of waveforms	87
7.5 Waveform Modeling.....	94
7.6 Conclusions.....	97
8. Conclusions.....	98
9. References.....	99

Figures

Figure 1. The explosion is offset by a distance d from the center of the cavity.	5
Figure 2. Pressure time history from 0.38 kt explosion in air at distances of 12-22 m.	6
Figure 3. Spectra (left) and waveforms (right) of the monopole and two dipole terms for the angle dependent arrival time with angle independent amplitude described in the text. The dipole terms scale approximately by d/c in msec, where d is the offset from center and c is the shock velocity at the boundary.	9
Figure 4. Spectra (left) and waveforms (right) of the monopole and two dipole terms for the angle dependent amplitude variation described in the text.	10
Figure 5. Pressure contours from left to right at 1.5, 2.0 and 2.5 msec. Dashed circle on the contour plot shows the cavity wall; the star shows the explosion location.	11
Figure 6. Pressure time histories at 5 points inside the cavity next to the wall. Zero degrees is in the direction of the explosion offset toward the bottom of the grid. Left figure shows the first 3.5 msec of the right figure.	12
Figure 7. Radial and vertical velocity waveforms low pass filtered at 200 Hz at a distance of 40 meters from the cavity center.	12
Figure 8. Pressure pulses at zero degrees and 180 degrees for the multiple reverberation example.	13
Figure 9. Far field P and S waveforms (top) and spectra (bottom) generated by the pressure pulses in Figure 8.	14
Figure 10. Composition of spectra at 3 angles: 45 degrees (top left), 90 degrees (top right) and 135 degrees (bottom).	15
Figure 11. Configuration of Kirghizia explosions at the center and upper edge of a spherical cavity.	17
Figure 12. Calculated P and S spectra at 90 degrees (horizontally) from the offset source configuration shown in Figure 11.	17
Figure 13. Vertical (left) and radial (right) components of data from the centered and offset Kirghizia explosions filtered from 2-8 Hz (top) and 8-14 Hz (bottom), scaled by the maximum vertical component amplitude. Increased shear waves are apparent in the higher frequency seismograms from the offset source.	18
Figure 14. Configuration of the centered (left) and off-center (right) 1 ton explosions sources in the spherical cavity. The explosive source is on scale relative to the cavity size.	21
Figure 15. Vertical component acceleration spectra of the centered (black) and off-center (dashed) explosions at 5 km.	22
Figure 16. Three component seismograms of the centered (black) and off-center (red) explosion at 2-8 Hz (top row) and 8-14 Hz (lower row), scaled by the maximum vertical component amplitude to account for decoupling. P waves are aligned at zero.	23
Figure 17. Vertical (solid) and Hilbert transformed radial (dashed) records of the off-center explosion at 8-14 Hz. The additional phase in the off-center records has retrograde motion.	23
Figure 18. Ratios of P (solid) and S waves (dashed) of the off-center to the centered amplitude spectra (right). Spectra are averages of the radial and vertical components.	24
Figure 19. Ratio of off-centered to centered explosion S spectra. The ratio is normalized by the off-centered to centered explosion P spectra to account for decoupling. Spectra are averages of the radial and vertical components.	25

Figure 20. Nonlinear yield regions (right column) for the centered (upper row) and off-center (lower row) explosions.....	26
Figure 21. Radial synthetic seismograms at 5 km, at 1-20 Hz (left) and 95-115 Hz (2 nd from right) for the off-center (solid) and centered (dashed) explosions, ratios of off-center to centered explosion S (dashed) and P (solid) amplitude spectra (2 nd from left), and the ratio of the off-centered to centered explosion S spectra normalized by the off-centered to centered explosion P spectra to account for decoupling. Off-center and centered synthetic seismograms are on the same scale within each plot.....	27
Figure 22. Synthetic far field P (left) and S (right) waves at different incidences from the vertical, due to amplitude variations resulting from the proximity of the offset source shown in Figure 14 to different locations on the cavity wall. Records are filtered from 1 to 40 Hz.....	28
Figure 23. Synthetic far field P (solid) and S (dashed) spectra due to amplitude variations around the cavity resulting from the offset source shown in Figure 14.....	28
Figure 24. Locations of near field strong motion instruments. This figure is reproduced from the paper by Healy et al (1971). The shot depth is 828m.	34
Figure 25. Comparison between the observations (solid lines) and numerical synthetics (dashed lines) at 9 stations. The top traces are tangential velocity and the bottom traces are radial velocity in each location. Note the good agreement between the observations and synthetics at the surface location and near the shot point. Spall at E-6-S is seen in both observations and simulations.....	35
Figure 26. Nonlinear regions generated by the Salmon explosion. Left: yield region extending to 1000m; right: Regions of tensile cracking around the cavity and the free surface (spall).....	36
Figure 27. Interaction between the air shock and the salt calculated from STELLAR at 2.627msec. Left: particle velocity vectors. Middle: pressure contours. The maximum pressure is 2.8kbar at 7m below the salt floor. Right: plastic work distribution. The maximum plastic work incurred is about 5×10^6 ergs/cm ³ at the pool floor, corresponding to the yield surface of 680bars. The higher plastic work indicates the higher yield surface (material hardening).....	38
Figure 28. Observed (red) and synthetic (black) waveforms at near-cavity locations in salt. The top curve in each plot represents the tangential component and the bottom curve represents the radial component. The blue vertical bars denote the theoretical SV arrival time ($v_s=2550$ m/s). The waveforms have been lowpass filtered below 100Hz. The agreement on P wave arrivals and amplitudes is striking, and the agreement on S wave arrivals and amplitudes is better for the shot-level locations and below than for above shot-level stations. The synthetics show less complexity than the observations.....	39
Figure 29. Left: nonlinear deformation distribution due to the Sterling explosion. The dashed line circle is drawn to highlight, by contrast, the asphericity of the yield region. Middle: tensile crack distribution due to the Sterling explosion. Tensile cracks open only near the cavity wall. No spall is observed in the calculation. Right: locations where dynamic fractures could occur.	40
Figure 30. P waveforms (top) and spectra (bottom) from the observations (left column) and nonlinear calculations (right column). The radial P waveforms are aligned at their predicted arrival times given a velocity of 4.6 km/s, and filtered from 3 – 100 Hz. In each waveform plot the top, the top, middle and bottom sets of seismograms correspond to	

receivers above, at and below the shot level. In the observed P spectra (bottom left), the thick line indicates the prediction for a spherically symmetrical case. All the records are scaled to the most distant location by using $Q_p=200$ and corrected for geometrical spreading. 42

Figure 31. S waveforms (top) and SV spectra (bottom) obtained from the observations (left column) and nonlinear calculations (right column). SV acceleration waveforms (tangential components) are aligned at the predicted arrival times given a velocity of 2.55km/s, filtered from 3 – 100 Hz. In each waveform plot, the top, middle and bottom seismograms correspond to receivers above, at and below the shot level. In the observed S spectra (bottom left) superimposed is the predicted spectrum using the scaling relationship between P and S waves as discussed in the text. All the records are scaled to the most distant location by using $Q_s=50$ for S after geometrical spreading correction. Records at the same level or similar incidence have similar waveforms from the initial S throughout the coda, indicating that the bulk of the energy is coming directly from the source. Note that the corner frequency of the observed S waves is higher than that of the P waves in both the observations and the synthetics. 43

Figure 32. P and S spectra (left) and velocity waveforms (right) from a point explosion source offset from the center of a 17 meter cavity at 90 degrees from the offset direction. 44

Figure 33. Vertical (solid) and Hilbert transformed radial (dashed) velocity records at 7.8 km, filtered from 5 -10 Hz, for three water-filled cavity explosions (upper three) plus the 27 Kt tamped explosion (bottom). Absolute times are not known, so traces are aligned with the first arrival set at 0.0 seconds. Alignment of the Hilbert transformed radial with the vertical identifies the local S_g phase as a higher mode R_g phase. 49

Figure 34. Record sections for the water-filled cavity explosions from 1 to 3 km (top), and from 1 to 9 km (bottom). Dashed lines show the 2.05 km/s group velocity (assuming a P-velocity of 4.25 km/sec) corresponding to the S arrivals. 50

Figure 35. Overlain Hilbert transformed radial (dashed) and vertical (solid) velocity records at 1.71 km of the 0.01 Kt explosion (left) and particle motion up to the S-P time (middle) and after the S-P time (right). 50

Figure 36: Radial (left) and vertical (right) spherical explosion (top) and CLVD (center) synthetics and data from the 0.35 Kt explosion (bottom) at 7.8 km. Vertical bars in the real data plots indicate the limits of the P (near the base of the plot) and S (near the top, approximately 3 to 4 seconds) windows used to estimate spectra. The explosion synthetic represents the response of the structure to a spherically symmetric source, and the CLVD is the first approximation to the non-spherical components of the source. 51

Figure 37: Overlain vertical (solid) and Hilbert transformed radial velocity records of the 0.01 Kt explosion at 7.8 km, filtered from 5 to 10 Hz. The first and second S arrivals (labeled S1 and S2) and the coda are delimited by vertical bars along the upper plot boundary. 52

Figure 38: Stacked radial and vertical spectra for each of events. 53

Figure 39. P (solid) and S (dashed) radial component spectra of the tamped (upper left) and three water-filled cavity explosions, using the first S arrival. Murphy et al (2001) identified the 9 Hz P spectral peak as associated with a bubble pulse in the water-filled explosions. The peak does not exist for the initial S wave. 54

Figure 40. Same as Figure 39, but for the second S arrival. 55

Figure 41. P (solid) and coda (dashed) spectra of the tamped (left) and 0.01 Kt water-filled cavity (right) explosions using the coda window of Figure 37.	55
Figure 42. Radial seismograms from event AZ25 (left) and CLVD synthetics (right). Seismograms are aligned on initial P. Dashed lines precede the S arrivals.....	56
Figure 43. S-P arrival times from event AZ25 (circles) and CLVD synthetics (triangles). Lines are fits to S-P times vs. distance.	56
Figure 44. Nonlinear yield region of the 27 Kt tamped explosion (left), and tensile cracks (right).	57
Figure 45: Synthetic vertical seismograms at 7.8 km, filtered from 5 to 10 Hz for an explosion plus a CLVD source of the same moment at the same depth (top), and an explosion plus CLVD source of the same moment but at half the depth (second trace), and for the source determined from the nonlinear source calculation (Figure 44). The deeper CLVD source matches the earlier S of the 0.35 Kt event (third trace), while the seismograms for the shallower CLVD and the nonlinear source are consistent with the later S energy in the tamped explosion record (bottom).	58
Figure 46. Initial velocity field (left), nonlinear yield region (middle), and tensile cracks (right) around the cavity for the 0.35 Kt explosion.	61
Figure 47. Radial seismograms at 7.8 km from the nonlinear source calculation (upper trace, solid) overlain with those from a spherical point explosion source (upper trace, dashed), compared with data (middle trace) and CLVD synthetics (bottom trace).....	61
Figure 48. Initial velocities (left), yield volumes (center), and tensile cracks (right) produced by a 0.35 Kt explosion in a 28.9 m radius water-filled cavity at 600 m depth in salt for detonation at the top (upper plots) and base (lower plots) of the cavity.....	62
Figure 49. Configuration of the water filled-cavity used in simulations. Pressure is recorded at three locations (triangles) within the cavity 20 m from the centered explosion source.	63
Figure 50. Pressure within the cavity for the 0.01 Kt (top) and 0.35 Kt (bottom) simulations at 3 locations, each 20 meters from the source. The unfiltered pressure signals are in the left column. The right column shows the same records filtered from 5 to 15 Hz.....	64
Figure 51. The yield region (left), the tensile cracking region (middle), and the dynamic cracking area (right) for fully pressurized fractures. The dynamic fracture region is restricted to about 3 m into the salt.	65
Figure 52: Left: pressure time history on cavity wall closest to (0 degrees) and farthest from (180 degrees) the explosion. Right: Far field P and S spectra at 90 degree takeoff angle.....	66
Figure 53. Vertical component data at 7.8 km for the 0.01 Kt explosion (top), a spherical explosion plus CLVD (middle), and a spherical explosion plus a vertical point force (bottom).....	67
Figure 54. Observed (left) and synthetic (right) tangential (upper trace) and overlain vertical (lower trace, solid) and Hilbert transformed radial (lower trace, dashed) seismograms at 4.64 km from the 0.08 Kt explosion, filtered from 5 to 10 Hz. The tangential synthetic S from a horizontal point force arrives later than the radial and vertical S from a vertical point force.	68
Figure 55. Location of explosions (circles) and accelerometers (triangles).	70

Figure 56. Vertical acceleration spectra at station 25, 506, 585, and 655 m respectively from explosions 1, 2, and 3.....	71
Figure 57: Predicted (Mueller-Murphy) acceleration spectra for the depth and yield, scaled by the decoupling factor, of the explosions (left), and RVP acceleration spectra from numerical calculations (right), for comparison with the observed acceleration spectra of the three explosions at station 25 (Figure 56). The Mueller-Murphy source is based on the parameters for tuff.....	72
Figure 58. Left: Earth structure and source depth of the 3 decoupled explosions. Right: 40 Hz modal excitation by a point explosion source in this structure.	72
Figure 59. Observed acceleration spectra (left) and synthetic acceleration spectra (right) for the three explosions described in the text, and for explosion 2 moved to a shallower depth. High frequency spectral differences are due to source depth and structure; low frequency differences are caused by decoupling.	73
Figure 60. Vertical component records of explosion 2 from stations 21 to 25, filtered from 3 to 7 Hz.	74
Figure 61. Vertical and Hilbert transformed radial record section, from 3 to 7 Hz, from stations 21 to 25.	75
Figure 62. Product trace record section at 3 to 7 Hz, from stations 21 to 25.....	75
Figure 63. Product trace record sections for stations south of the explosions, at 0.5 - 1.5, 1.5 - 3, 3 - 5, 5 - 8, 8 - 11, and 11 - 15 Hz from left to right and from the top down.....	76
Figure 64. Product traces for explosion 3 at station 24, 488 meters from the source, in 6 passbands.	77
Figure 65. Three component records of explosion 3 at station 25 (655 m) in 6 passbands. All components in each passband are plotted on the same scale.....	78
Figure 66. Product traces of the vertical and Hilbert transformed radial records of explosion 2 for stations south of the source, at 0.5 - 1.5, 1.5 - 3, 3 - 5, 5 - 8, 8 - 11, and 11 - 15 Hz from left to right and from the top down.	79
Figure 67. Product traces for explosion 2 at station 24, 418 meters from the source, in 6 passbands.	80
Figure 68. Three component records of explosion 2 at station 25 (585 m) in 6 passbands. All components in each passband are plotted on the same scale.....	80
Figure 69. Product traces of the vertical and Hilbert transformed radial records of explosion 1 for stations south of the source, at 0.5 - 1.5, 1.5 - 3, 3 - 5, 5 - 8, 8 - 11, and 11 - 15 Hz from left to right and from the top down.	81
Figure 70. Product traces for explosion 1 at station 24, 366 meters from the source, in 6 passbands.	82
Figure 71. Three component records of explosion 1 at station 25 (534 m) in 6 passbands. All components in each passband are plotted on the same scale.....	82
Figure 72. Upper left plot shows vertical P (red, lower trace) and tangential S (blue, upper trace) seismograms at the most distant station, 15. Corresponding spectra are shown in the upper right. The P-wave particle motion in the vertical-radial plane is linear and vertically oriented (lower left). The S particle motion in the tangential-radial plane begins tangentially polarized and quickly becomes circular.....	83
Figure 73. SV and SH spectra of explosion 2, recorded at four stations.	84
Figure 74. SV and SH spectra of explosions 1 (left) and 3 (right), recorded at station 15.	85

Figure 75. Plots for each explosion at station 15, similar to Figure 72 except that the bottom right plot of each set shows the S-to-P spectra ratio.....	86
Figure 76. Vertical component records of the tamped (solid) explosion and the shallower partially decoupled explosion, at 145.4 and 163.2 m respectively. Initial P arrivals are aligned at 0.2 seconds.	87
Figure 77. Vertical component records of the tamped (solid) and partially decoupled explosion at station 15, 709.2 and 715.5 m distance respectively. Initial P arrivals at aligned at 0.2 seconds.	88
Figure 78. Tangential (upper traces) and overlain vertical (solid) and Hilbert transformed radial (dashed) records (lower traces) at station 11, 145.4 and 163.2 m distance respectively from the tamped (left column) and partially decoupled (right column) explosions. Initial P arrivals are aligned at 0.2 seconds.	89
Figure 79. Tangential (upper traces) and overlain vertical (solid) and Hilbert transformed radial (dashed) records (lower traces) at station 15, 709.2 and 715.5 m distance respectively from the tamped (left column) and partially decoupled (right column) explosions. Initial P arrivals are at aligned at 0.2 seconds.....	90
Figure 80. S-to-P ratios (tangential S to vertical P) predicted for the explosion 1 Mueller-Murphy source (upper left) and for each explosion, from 10 to 50 Hz.	91
Figure 81. Relative S-to-P spectral ratios of one event to the next. Upper left is the Mueller-Murphy prediction for the explosion 2 to explosion 3 S-to-P ratios.....	91
Figure 82. Vertical component records of the tamped (solid) explosion and the deeper partially decoupled explosion, at 295 and 320.7 m respectively. Initial P arrivals are aligned at 0.2 seconds.	92
Figure 83. Vertical component records of the tamped (solid) explosion and the deeper partially decoupled explosion, at 478.1 and 443.5 m respectively. Initial P arrivals are aligned at 0.2 seconds.	93
Figure 84. Tangential (upper traces) and overlain vertical (solid) and Hilbert transformed radial (dashed) records (lower traces) at 295 and 320.7 m distance respectively from the tamped explosion 1 (left column) and the deeper partially decoupled explosion 2 (right column) explosions. Initial P arrivals are at aligned at 0.0 seconds.	93
Figure 85. Amplitude and phase response of the episensor, to acceleration, from the EpiSensor's user's manual. Y axes are dB and degrees.	94
Figure 86. Synthetic (red) and actual records (blue) of the tamped explosion at 710 meters in 4 passbands.....	96
Figure 87. Synthetic (red) and actual records (blue) of the deeper, more decoupled explosion 1 at 710 meters in 4 passbands.	96
Figure 88. Synthetic (red) and actual records (blue) of the deeper, more decoupled explosion 2 at 710 meters in 4 passbands.	97

Tables

Table 1. Salmon Structure Model Parameters (Murphy 1991).....	34
Table 2: Azgir nuclear explosion dates and times.	48
Table 3: Available data from tamped (A2) and water-filled cavity explosions.....	48
Table 4: Velocity model. The second layer represents an anhydrite cap on a massive salt dome.....	51
Table 5: Source parameters of the three Israeli decoupling explosions.....	70

Acknowledgments

We thank Steve Day for pointing out the conservation of momentum condition for the work in Section 3. Bill Walter provided extensive and useful reviews of the manuscripts of the journal articles that comprises Sections 4 and 6. Dr. Norton Rimer and the late Dr. Evan Bailey provided assistance with the numerical calculations in Section 5. Critical review by Charles Langston of the journal article that comprises section 5 improved the manuscript.

1. SUMMARY

This project spawned four papers submitted to peer-review journals for publication, which comprise Sections 3 through 6 of this report. As such, each can be read as a stand-alone article. The first (Stevens and Baker, 2009) presents analytic and numerical solutions for off-center explosions in a spherical cavity. This work demonstrates that offset of the source leads to a dipole source component which can generate significant shear waves. The second paper (to be submitted) tests the predictions of the first. It analyzes and models data from an off-center explosion and a centered explosion in the same spherical cavity. These explosions were part of a series of decoupling experiments in 1960 in Kirghizia. The third paper (section 5, Xu et al., 2009) isolates the near field shear waves from Sterling and models the observations. It demonstrates that the shear waves are consistent with generation at the source, with the initial S-wave radiation pattern reproduced by modeling that incorporates the flat cavity floor, which is due to melted and then recrystallized salt. The fourth paper (Baker et al, 2009) analyzes local data from a series of nuclear explosions in a water-filled cavity, along with comparable records of the tamped explosion that generated the cavity. The focus is on features that can distinguish between mechanisms for generation of the shear waves. Spectral features, moveout, and S minus P times for the tamped vs. water-filled cavity explosions are all consistent with shear waves being generated at the source by the water-filled cavity explosions.

Two further data sets were analyzed. These contribute less to our understanding of source shear wave generation by decoupled explosions, as the S-waves are dominantly due to conversion from P-waves at the free surface. Even so, documenting the observations, modeling, and conclusions are valuable. The seventh section analyses and models the data of the recent Israeli decoupling experiments (Gitterman et. al, 2007). The S and P waveforms and spectra of these explosions demonstrate some additional difficulties that arise for very shallow sources, where modal excitation is complex and difficult to predict and for which common models, such as the Mueller-Murphy source model, were not developed. In that section we also introduce a new approach to separating overlapping (in time and frequency) P and S-waves local records. Section eight documents the observations of decoupled explosions in an air-filled cavity salt at the Azgir test site. A final section, section nine, summarizes the conclusions common to these investigations, which have advanced our understanding of how shear waves are generated by fully and partially decoupled explosions.

The Salmon/Sterling, Azgir (both air and water-filled cavity explosions), and Kirghizia data are part of a database delivered to AFRL under another recent SAIC contract (Stevens et al, 2004). The Israeli data were also recently delivered to AFRL, by Gitterman et al (2007b).

2. INTRODUCTION

Decoupling is a well-studied and important means of evading detection of a nuclear explosion. The intent is that much of the energy of an explosion will be spent within a sufficiently large cavity, so that the resulting seismic wave amplitudes will be too small to be detected. Work to date on such explosions has largely focused on the extent to which P-wave amplitudes are diminished, and on what factors control the decoupling, such as cavity size relative to yield, cavity shape, and position of the explosive within the cavity. Most such

explosions however are only partially decoupled, and with the extensive global seismic coverage available, they might well be detected. This shifts the focus to identification of an event as an explosion.

A fully decoupled explosion detonated in the center of a spherical cavity is a purely compressional seismic source, and thus its discrimination should be straightforward. In practice however, shear waves from decoupled explosions are ubiquitous, often identical to shear waves from comparable tamped explosions, and much evidence indicates that they are generated at the source. In some circumstances, decoupled explosions generate even more shear waves relative to compressional waves than corresponding tamped explosions. Understanding the generation of shear waves by decoupled and partially coupled explosions is therefore important for nuclear monitoring.

If the explosion is detonated in the center of a spherical cavity large enough to fully decouple the event, any shear waves observed in its records must be the result of conversion from P and/or Rg phases at the free surface or other interfaces. A variety of asymmetries however, such as asphericity of the cavity or offset or asymmetry of the explosion, could lead to the direct generation of shear waves even from a fully decoupled explosion. Also, fracturing or asymmetry of a nonlinear region about the cavity could result in direct generation of shear waves by a partially decoupled explosion.

In this report we detail observations of shear waves from decoupled explosions focusing on features that distinguish their genesis and on numerical modeling of the observations. Most of the data have already been studied extensively, but usually with the goal of quantifying P-wave decoupling. Most of the data are from tamped and decoupled explosion pairs, generally with the decoupled explosion detonated in the cavity created by the tamped explosion, so that path differences are eliminated. These include the U.S. nuclear explosions in salt, Salmon and Sterling, and Soviet explosions in salt at the Azgir test site, both in air-filled and water-filled cavities. We also examine explosions in spherical cavities in limestone in Kirghizia, focusing on the difference between a centered and an off-center source. Simulations include both analytical and numerical models of the reverberations within a spherical cavity of an off-center source, nonlinear source calculations that simulate an aspherical cavity (Sterling), the effect of off-center explosions beyond the cavity walls for partially tamped explosions, and the extent and orientation of fracturing by decoupled explosions and their effect on the resulting waveforms.

3. SEISMIC WAVE GENERATION BY A NON-ISOTROPIC EXPLOSION SOURCE

Abstract: We develop a general solution for seismic wave generation by an explosion source in a spherical cavity, and then a specific solution for a point explosion source offset from the cavity center. We find that the offset causes a dipole component to the source which generates S waves and causes angular variation in P wave amplitude and shape. The S waves vanish at zero frequency but may be a sizeable fraction of the P waves at frequencies of interest. We also perform a nonlinear axisymmetric calculation of an offset explosion in a spherical cavity, which causes a complex source due to cavity reverberations and generates S waves comparable to those found from the analytic solution. The solution has application to shear wave generation by decoupled explosions, and explains at least part of the shear waves observed from such explosions. Data from a pair of explosions centered and offset from the center of a spherical cavity show the expected enhancement of shear waves from the offset source.

3.1 Introduction

Decoupling of a nuclear explosion by detonation in a large cavity has been a longstanding issue for nuclear monitoring. Most previous research has focused on observation and/or prediction of the “decoupling factor”, which is the amplitude ratio of the seismic signal of the tamped explosion to the seismic signal of the decoupled explosion (Latter et al, 1961; Denny and Goodman, 1990; Stevens et al., 1991a,b,c; Glenn and Goldstein, 1994; Murphy et al, 1997; Stevens et al, 2006a). Less attention has been paid to shear wave generation by decoupled explosions, the main exception being two analyses of near field shear wave generation by the Sterling explosion (Langston, 1983; Xu et al, 2009). Since the most reliable discriminants for events in the magnitude range of decoupled explosions are high frequency spectral ratios of the amplitudes of the seismic shear phases S_n and L_g to P_n or P_g (Taylor, 1991), it is important to understand and quantify the sources of shear wave generation by decoupled explosions. In this paper we examine one such mechanism: the generation of shear waves by an explosion offset from the center of a spherical cavity.

Stevens (1980) developed a solution for the seismic waves generated by an explosion in an arbitrarily prestressed elastic medium. In this paper, we generalize the solution to allow for cases where the explosion is non-isotropic. In particular, we consider cases where the explosion is offset from the center of the cavity so that the amplitude and arrival time of the explosion vary as a function of position on the cavity wall. The motivation for this work is that shear waves are observed from almost all explosions, including fully decoupled explosions, and one possible explanation for shear wave generation is non-spherical motion of the cavity wall in response to non-isotropic forcing by the explosion source. In the following, we model a decoupled explosion: a pressure pulse in a spherical cavity with linear elastic material outside. The examples approximately follow the Sterling decoupled explosion, a 0.38 kiloton explosion detonated in the 17 meter cavity created by the earlier Salmon explosion. While the following solution explicitly models a decoupled explosion, it may have more general application to seismic radiation from tamped explosions in heterogeneous conditions.

3.2 General solution for variable pressure applied to spherical cavity

The general solution for the seismic wave field from a set of tractions applied to the inside of a spherical cavity is given by (Stevens, 1980):

$$u = -\int_{\Sigma} u \cdot T(G) \cdot \hat{n} dA + \int_{\Sigma} G \cdot T(u) \cdot \hat{n} dA - \frac{1}{i\omega} \int_{\Sigma} G \cdot T(u^*) \cdot \hat{n} dA \quad (1)$$

where Σ is the cavity surface, u on the left side of the equation is the displacement at any location outside the cavity, and u inside the integral is the displacement on the cavity wall. G is the elastic Green's tensor in spherical coordinates, and T is the stress operator. u^* is the difference in the static displacement field before and after the explosion due to changes in the static stress field, and so will vanish for a decoupled explosion where the prestress does not change, but will be non-zero for a tamped explosion with tectonic strain release. The third integral therefore represents the response of the medium to a change in prestress, the second integral represents the response of the medium to the applied stress from the explosion, and the first integral represents the additional motion due to the response of the cavity wall.

We solve equation 1 for the case where the prestress integral vanishes and the applied stress varies at different locations on the cavity wall. We model the explosion as a pressure pulse, and assume that the applied pressure is normal to the cavity wall. In that case, the applied stress field can be expanded in vector spherical harmonics (Morse and Feshbach, 1953) as:

$$T(u) \cdot \hat{n} = \sum_{l=0}^{\infty} \sum_{m=-l}^l a_{lm}(\omega, R) P_{lm}(\theta, \phi) \quad (2)$$

where using the orthogonality of the vector spherical harmonics:

$$a_{lm}(\omega, R) = \frac{2l+1}{4\pi} \frac{(l-m)!}{(l+m)!} \int_{\Sigma} P_{lm}(\theta, \phi) \cdot T(\omega, R, \theta, \phi) \cdot \hat{n} dA \quad (3)$$

By expanding the Green's tensor in equation 1 in vector spherical harmonics and again using orthogonality, we can evaluate the second integral. Defining

$$u^T = \int_{\Sigma} G \cdot T(u) \cdot \hat{n} dA = -i\omega \sum_{l=0}^{\infty} \sum_{m=-l}^l d_{lm}^1(\omega, R) P_{lm}(\theta, \phi) + d_{lm}^2(\omega, R) B_{lm}(\theta, \phi) \quad (4)$$

where using the notation of Stevens (1980) and Ben-Menahem and Singh (1968):

$$d_{lm}^1 = \frac{a_{lm}}{\mu\beta} \left[\frac{g_l^{2+}(y_0) g_l^{2-}(y)}{l(l+1)} + \left(\frac{\beta}{\alpha}\right)^3 g_l^{4+}(x_0) g_l^{4-}(x) \right] \quad (5)$$

$$d_{lm}^2 = \frac{a_{lm}}{\mu\beta} \left[\frac{g_l^{2+}(y_0) g_l^{3-}(y)}{l(l+1)} + \left(\frac{\beta}{\alpha}\right)^3 g_l^{4+}(x_0) g_l^{5-}(x) \right] \quad (6)$$

with $y = k_{\beta} r$, $x = k_{\alpha} r$, $y_0 = k_{\beta} R$ and $x_0 = k_{\alpha} R$, r the radial coordinate of the receiver point and R the cavity radius. Stevens (1980) solved equation 1 for an instantaneous change in prestress with no applied stress. Except for the factor of $-i\omega$, Equations 4-6 are expressed in the same form as the equations in that paper (equations 3.3 and 3.7) and so the solution is:

$$u(\omega, r, \theta, \phi) = -i\omega \sum_{l=0}^{\infty} \sum_{m=-l}^l b_{lm}^1(\omega, r) P_{lm}(\theta, \phi) + b_{lm}^2(\omega, r) B_{lm}(\theta, \phi) \quad (7)$$

where the coefficients b_{lm}^1 and b_{lm}^2 are derived from d_{lm}^1 and d_{lm}^2 using equation 3.12 of that paper. Note that equation 4 gives the solution for a stress pulse applied at the cavity radius in an infinite medium with no cavity, while equation 7 includes the response of the cavity.

3.3 Solution for an offset explosion source

Equation 7 is the final result, giving the displacement field at any location outside the cavity in terms of the applied stress at the cavity surface, expressed as a sum of vector spherical harmonics. It is only necessary to perform the integral in equation 3 to determine the coefficients a_{lm} and the displacement field can then be calculated using the equations above. We now consider an example in which the explosion is offset from the center of the cavity as shown in Figure 1. This causes an asymmetry in the source due to the angular variation in arrival time, and the angular variation in amplitude.

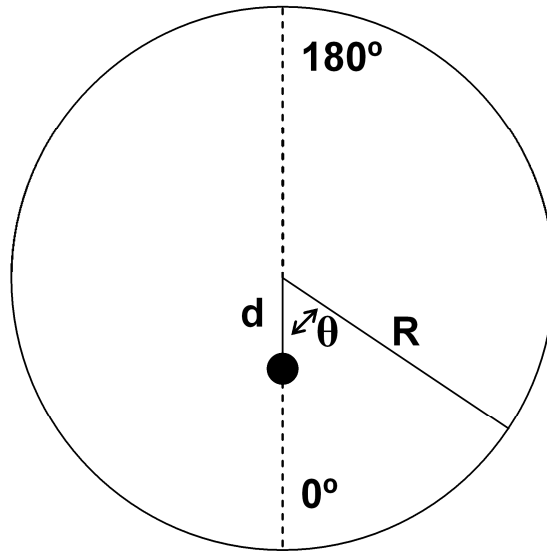


Figure 1. The explosion is offset by a distance d from the center of the cavity.

We assume that the pressure pulse arrival time and amplitude are only a function of θ , with no azimuthal dependence. In that case, only the $m=0$ term is non-zero in the equations above, and equation 3 becomes:

$$a_{l0}(\omega) = \frac{2l+1}{2} \int_0^\pi P_l(\cos\theta) \bar{P}(\theta, \omega) \sin\theta d\theta \quad (8)$$

where P_l is the Legendre function of order l , and $\bar{P}(\theta, \omega)$ is the applied pressure at the cavity wall at angle θ and angular frequency ω . We also assume that the pressure eventually reaches a uniform steady state P_0 , and separate the transient time and angle dependent part P_1 . In the time domain:

$$P(\theta, t) = [P_0 + P_1(\theta, t - \tau(\theta))] H(t - \tau(\theta)) \quad (9)$$

where $\tau(\theta)$ corresponds to the arrival time of the shock wave on the cavity wall and $P_1(\theta, t - \tau)$ describes its amplitude and time history. In the frequency domain, equation 9 becomes:

$$\bar{P}(\theta, \omega) = \left(\frac{P_0}{i\omega} + \bar{P}_1(\theta, \omega) \right) \exp(-i\omega\tau(\theta)) \quad (10)$$

where \bar{P}_1 is the Fourier transform of the pressure P_1 and P_0 is a constant, the steady state pressure.

3.4 Spherically symmetric calculation of the pressure field from an explosion in air

To get a better idea of the form of the pressure field in equations 8-10, we performed a nonlinear spherically symmetric calculation of an explosion of a 0.38 kiloton explosion in air. The air is modeled using a tabular equation of state developed by Marv Alme at the Air Force Weapons Laboratory in 1977. Figure 2 shows the pressure time histories at several locations for this calculation. Note that the time difference between peaks increases with distance as the shock wave decreases in velocity. The shock wave velocity decreases to about 5000 m/s at 17 meters. Also, the shock wave becomes smaller and broader with increasing distance.

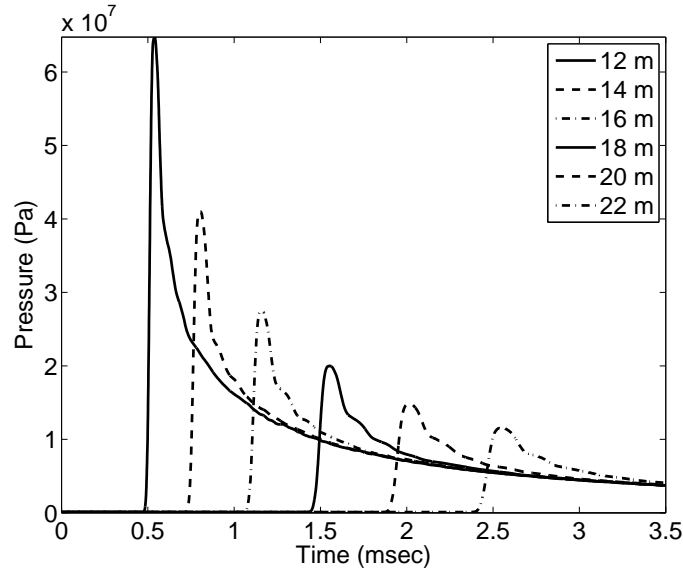


Figure 2. Pressure time history from 0.38 kt explosion in air at distances of 12-22 m.

3.5 Conservation of momentum

An important constraint on the applied pressure P is that conservation of momentum requires that the total impulse on the cavity vanish. That is, forces may vary in arrival time and amplitude around the cavity wall, but cannot lead to a long-term finite impulse when integrated over the cavity wall. This condition can be expressed as follows:

$$I_x = 2\pi \int_0^{\infty} dt \int_0^{\pi} P(\theta, t) \sin\theta \cos\theta d\theta = 0 \quad (11)$$

Since $\cos\theta$ is the Legendre function of order 1, this is a constraint on the dipole component of the source: the a_{10} term in equations 3 and 8. Note, however, that it does not require that the

dipole vanish, only that it integrate to zero over time, or equivalently vanish at zero frequency. In the frequency domain the above condition becomes:

$$\lim_{\omega \rightarrow 0} \int_0^{\pi} \bar{P}(\theta, \omega) \sin \theta \cos \theta d\theta = 0 \quad (12)$$

Expanding the exponential in equation 10 for small frequencies and using the fact that the static term integrates to zero, condition 12 becomes:

$$\lim_{\omega \rightarrow 0} \int_0^{\pi} \left[-P_0 \tau(\theta) + \bar{P}_1(\theta, \omega) \right] \sin \theta \cos \theta d\theta = 0 \quad (13)$$

If we assume that the variation in arrival time can be described by a shock velocity c , so that $\tau = (R' - R) / c \approx -\frac{d}{c} \cos \theta$, the pressure can be written:

$$\bar{P}(\omega, \theta) = \left[\frac{P_0}{i\omega} + \bar{P}_1(\theta, \omega) \right] \exp(i\omega d \cos \theta / c) \quad (14)$$

Expanding \bar{P}_1 in terms of Legendre functions:

$$\bar{P}_1 = \bar{P}_{10} + \bar{P}_{11} \cos \theta + \dots \quad (15)$$

and using the low frequency approximation for the exponential we get:

$$\bar{P}(\omega, \theta) \approx \left[\frac{P_0}{i\omega} + \bar{P}_{10}(\omega) + \bar{P}_{11}(\omega) \cos \theta + P_0 \frac{d \cos \theta}{c} + \bar{P}_{10}(\omega) \frac{i\omega d \cos \theta}{c} + \bar{P}_{11}(\omega) \frac{i\omega d \cos^2 \theta}{c} \right] \quad (16)$$

and condition 12 then gives:

$$\lim_{\omega \rightarrow 0} \bar{P}_{11}(\omega) + P_0 \frac{d}{c} = 0 \quad (17)$$

Neglecting the last term in equation 16 which varies as $(d/c)^2$, the nonvanishing coefficients in equation 3 are:

$$a_{00}(\omega, R) = \left[\frac{P_0}{i\omega} + \bar{P}_{10}(\omega) \right] \quad a_{10}(\omega, R) = \bar{P}_{11}(\omega) + P_0 \frac{d}{c} + \bar{P}_{10}(\omega) \frac{i\omega d}{c} \quad (18)$$

This is a general low frequency ($\omega d / c \ll 1$) solution for the lowest order terms since we have not placed any restriction on the functional form or angular variation of the applied pressure except for its start time.

3.6 Variable arrival time

In the simplest case, the transient pressure P_1 has the same functional form at all points on the cavity wall, differing only by start time. If we assume that P_1 has a characteristic decay time γ , so that $P_1(t) = P_1 \exp(-\gamma t)$, then $\bar{P}_{10} = \frac{P_{10}}{i\omega + \gamma}$, and \bar{P}_{11} represents the momentum conserving response of the pressure field to the cavity wall. For simplicity we consider it to be a damped

exponential with decay constant γ_d , so $\bar{P}_{11} = \frac{P_{11}}{i\omega + \gamma_d}$. Here P_{10} and P_{11} are constants. Condition

1.17 requires that $P_{11} = -P_0 \gamma_d \frac{d}{c}$, so

$$\bar{P}_{11}(\omega) = -P_0 \frac{d}{c} \frac{\gamma_d}{i\omega + \gamma_d} \quad (19)$$

From equation 8, the multipole coefficients are given by:

$$a_{l_0}(\omega) = \frac{2l+1}{2} \int_0^\pi P_l(\cos\theta) \left[\frac{P_0}{i\omega} + \frac{P_{10}}{\gamma + i\omega} - \frac{d}{c} \frac{P_0 \gamma_d \cos\theta}{\gamma_d + i\omega} \right] \exp\left(i\omega \frac{d}{c} \cos\theta\right) \sin\theta d\theta \quad (20)$$

The nonvanishing low frequency coefficients (equation 18) for this case are:

$$a_{00}(\omega, R) = \left[\frac{P_0}{i\omega} + \frac{P_{10}}{i\omega + \gamma} \right] \quad a_{10}(\omega, R) = i\omega \frac{d}{c} \left[\left(\frac{P_0}{i\omega + \gamma_d} \right) + \left(\frac{P_{10}}{i\omega + \gamma} \right) \right] \quad (21)$$

a_{00} is the explosion monopole, which contains a static and a transient term. a_{10} is a dipole term, which in this case comes from a transient pressure of angle independent amplitude applied at the shock arrival time. At high frequencies the solution is more complicated and the coefficients must be evaluated numerically.

The coefficients in equation 20 lead to three nonvanishing terms in equation 7: b_{00} , the P-wave generated by the explosion monopole, b_{10}^1 , the P-wave generated by the dipole term, and b_{10}^2 , the S-wave generated by the dipole term. The P-wave generated by the dipole term causes the shape of the P-wave to vary with azimuth. The S-wave, of course, does not exist for the monopole.

Going back to equations 5-7, we can examine the frequency dependence of the radiated waves. In the far field, the functions g_l^{2-} and g_l^{5-} vanish, and the functions g_l^{3-} and g_l^{4-} become spherical Hankel functions with a frequency and distance dependence of $(\omega r)^{-1}$. In the low frequency limit, the functions g_l^{2+} and g_l^{4+} depend on the frequency and cavity radius as $(\omega R)^{-1}$, except for the $l=0$ term which is proportional to ωR , so in the low frequency limit, the factors d_{10}^1 and d_{10}^2 , as well as b_{10}^1 and b_{10}^2 are proportional to $(\omega R)^{-2}$ and d_{00} and b_{00} are constant. From equation 7, the far field displacement is proportional to these factors times frequency. Collecting all of the factors from equations 4, 7 and 20, we find that the low frequency far field displacement from the monopole and dipole parts of the source are:

$$d_{00}^1 \sim i\omega a_{00}(\omega, R) = P_0 + \frac{i\omega}{\gamma} P_{10} \quad (22)$$

$$d_{10}^1 \sim \frac{\alpha}{R} a_{10}(\omega, R) \approx i\omega \frac{\alpha}{R} \frac{d}{c} \left(\frac{P_0}{\gamma_d} + \frac{P_{10}}{\gamma} \right) \quad (23)$$

$$d_{10}^2 \sim \frac{\beta}{R} \frac{\alpha^3}{\beta^3} a_{10}(\omega, R) \approx i\omega \sqrt{2} \frac{\alpha^3}{\beta^3} \frac{\beta}{R} \frac{d}{c} \left(\frac{P_0}{\gamma_d} + \frac{P_{10}}{\gamma} \right) \quad (24)$$

Including the response of the cavity increases the long period limit of b_{00}^1 by about a factor of 2.5 over d_{00}^1 , while the long period limit of d_{10}^1 and d_{10}^2 are the same as b_{10}^1 and b_{10}^2 .

Figure 3 shows an example. We have used the coefficients in equation 20 with $\gamma=300s^{-1}$ and $\gamma_d=150s^{-1}$ which correspond approximately to the time for a shock wave to travel a cavity radius and a cavity diameter, respectively. Figure 3 shows the far-field spectra and waveforms calculated from equations 20 and 7, with $P_{10}=P_0$ and d/c set to 0.001. The wavefield for a different offset can be calculated approximately by multiplying the dipole waveforms by d/c (in msec) and adding to the monopole term. The monopole static and transient terms are the first and second terms in a_{00} in equation 20, respectively.

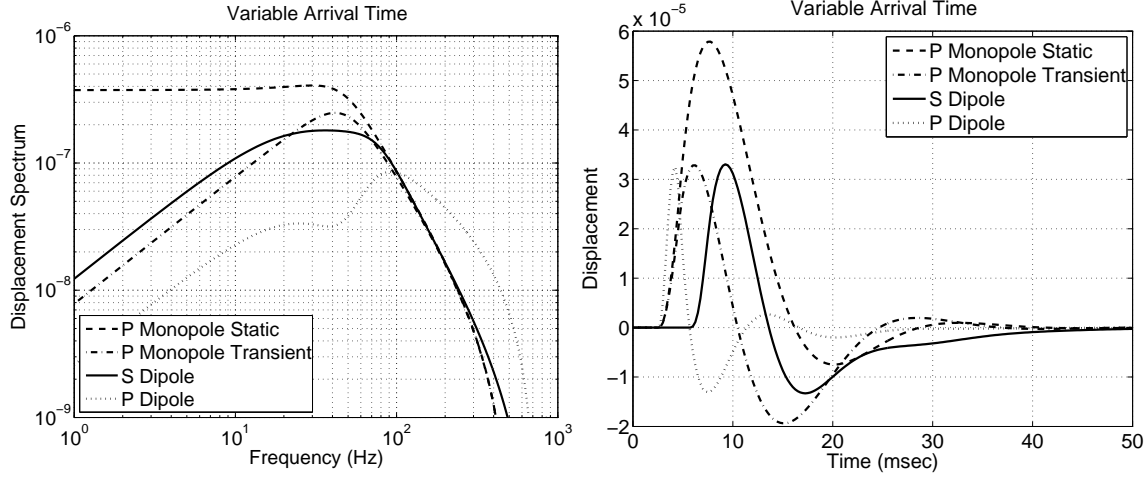


Figure 3. Spectra (left) and waveforms (right) of the monopole and two dipole terms for the angle dependent arrival time with angle independent amplitude described in the text. The dipole terms scale approximately by d/c in msec, where d is the offset from center and c is the shock velocity at the boundary.

With an offset of 5 meters, the source is 12 meters from the closest wall and 22 meters from the distant wall. From Figure 2 there is a time delay of 2 msec between the opposite sides ($d/c \sim 1$ msec), and so would generate approximately the dipole sources illustrated in Figure 3. The amplitude of the dipole terms depend on the difference in arrival time across the cavity, and therefore on the shock velocity in opposite directions. Note that this takes into account only the effect of the time delay between opposite sides, not the difference in amplitude or waveform duration.

3.7 Variable amplitude

Next, we consider the effect of amplitude variations on the cavity wall. From equation 8, the monopole and dipole coefficients for an axisymmetric source can be found by:

$$a_{00} = \frac{1}{2} \int_0^{\pi} P(\omega, \theta) \sin \theta d\theta \quad (25)$$

$$a_{10} = \frac{3}{2} \int_0^{\pi} P(\omega, \theta) \cos \theta \sin \theta d\theta \quad (26)$$

From Figure 2, we can expect that points closer to the source will experience a higher pressure that decays faster than more distant points. So as a simple example, consider a pressure that has a value P_1 with decay time γ_1 on the side of the cavity closest to the explosion ($\theta < \pi/2$)

and a value P_2 with decay time γ_2 on the side of the cavity away from the explosion $\theta > \pi/2$. This gives:

$$a_{00} = \frac{1}{2} \left[\frac{P_1}{\gamma_1 + i\omega} + \frac{P_2}{\gamma_2 + i\omega} \right] \quad (27)$$

$$a_{10} = \frac{3}{4} \left[\frac{P_1}{\gamma_1 + i\omega} - \frac{P_2}{\gamma_2 + i\omega} \right] \quad (28)$$

and conservation of momentum requires that

$$\frac{P_1}{\gamma_1} = \frac{P_2}{\gamma_2} \quad (29)$$

so the pressure difference generates a dipole term, but the higher pressure applied to one side must be offset by a lower, but longer duration pressure on the other side. If there is a static pressure, this just adds $P_0/i\omega$ to a_{00} .

Using the pressure calculations shown in Figure 2, and approximating the pressure applied to the two sides of the cavity with a 5 meter offset by the pressures at 12 and 22 meters, we get approximately for the relative pressures: $P_0=0.5$, $P_1=6.0$, $P_2=0.6$ (all $\times 10^8$ Pa); and for the time constants $\gamma_1=(0.4 \text{ msec})^{-1}$, $\gamma_2=(4 \text{ msec})^{-1}$. The far field spectra and waveforms are shown in Figure 4. The results are quite similar to those found above for the variable time delay.

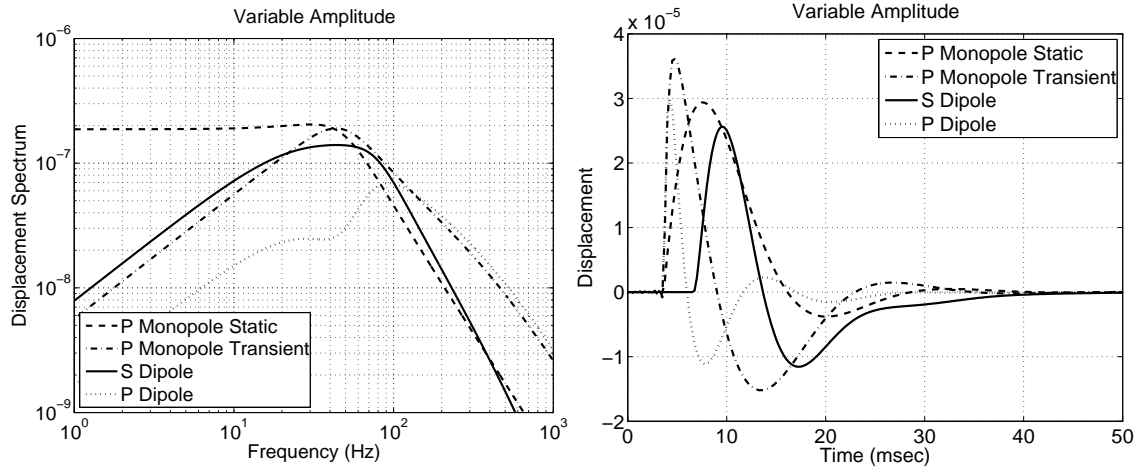


Figure 4. Spectra (left) and waveforms (right) of the monopole and two dipole terms for the angle dependent amplitude variation described in the text.

3.8 Axisymmetric calculation of an offset explosion in a cavity

To get a more realistic estimate of the pressure field and waveforms that would be generated by an offset explosion source, we performed a nonlinear axisymmetric calculation of an explosion in a 17 meter radius air-filled cavity, offset from the center by 5 meters. Calculations were performed using the Eulerian finite difference code STELLAR (Stevens et al, 1991c), which was developed using the methodology in Colella and Woodward (1984). Again, the explosion yield was 0.38 kilotons, so both the yield and cavity size corresponded to the Sterling nuclear explosion. However we used a strong rock model exterior to the cavity to prevent the plastic yielding that occurs with salt. The calculation did not include gravity. Figure 5 shows the

calculated pressure field at three times. The explosion is below the center of the cavity which corresponds to the $\theta=0$ direction. The snapshots show the pressure field starting after the shock wave has passed through the bottom of the cavity and continuing until it reaches the top.

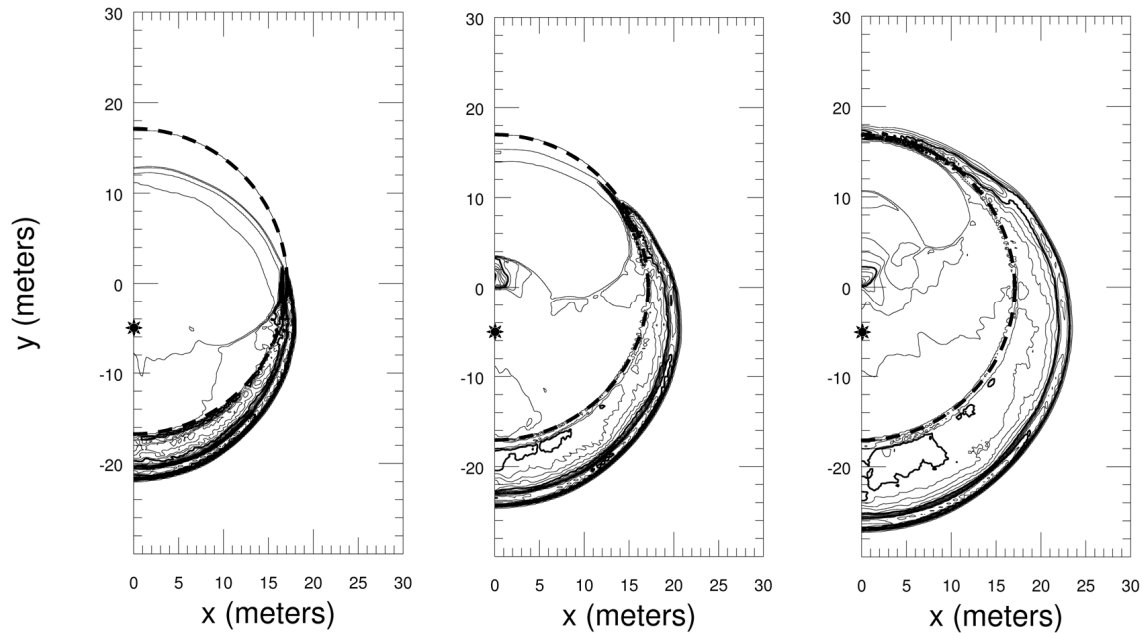


Figure 5. Pressure contours from left to right at 1.5, 2.0 and 2.5 msec. Dashed circle on the contour plot shows the cavity wall; the star shows the explosion location.

Figure 6 shows the pressure time histories at 5 points around the cavity just inside the cavity wall. Two time windows are shown: the first 3.5 msec and 50 msec. The pressure pulses in the first 3.5 msec are similar to the free field pulses in Figure 2, but have a larger initial peak and are more complex because of the interaction between the shock wave and the cavity wall. These are followed by a series of complex cavity reverberations that persist for quite a long time. The first reverberation at the far side of the cavity from the explosion is actually larger than the initial pressure pulse. This is caused by the reflected wave from the bottom of the cavity arriving at the top in time to interfere with the first reflection from the top. Notice in the right hand panel of Figure 5 that the reflected wave has almost reached the top. There is a large pressure spike at the top at about 4 msec.

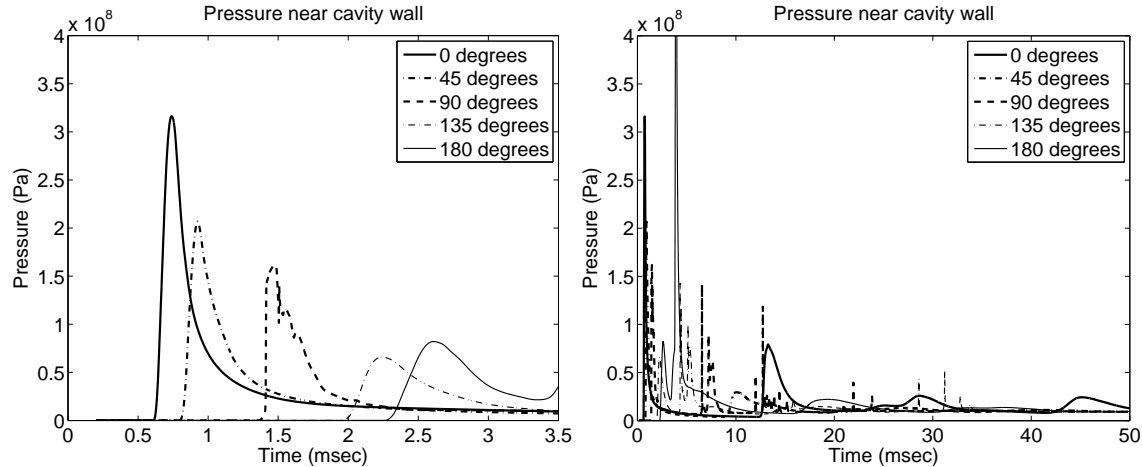


Figure 6. Pressure time histories at 5 points inside the cavity next to the wall. Zero degrees is in the direction of the explosion offset toward the bottom of the grid. Left figure shows the first 3.5 msec of the right figure.

Figure 7 shows velocity waveforms at 45 degree increments from the offset direction to opposite direction at a distance of 40 meters from the cavity center. At this distance the radial and transverse components are mixed P and S waves, but the radial is primarily P and the transverse is primarily S. The amplitude of the S phase relative to P is comparable to the offset source solutions. The waveforms are considerably more complex because of the greater complexity of the pressure field in the cavity, and because 40 meters is still in the near field for the waveforms.

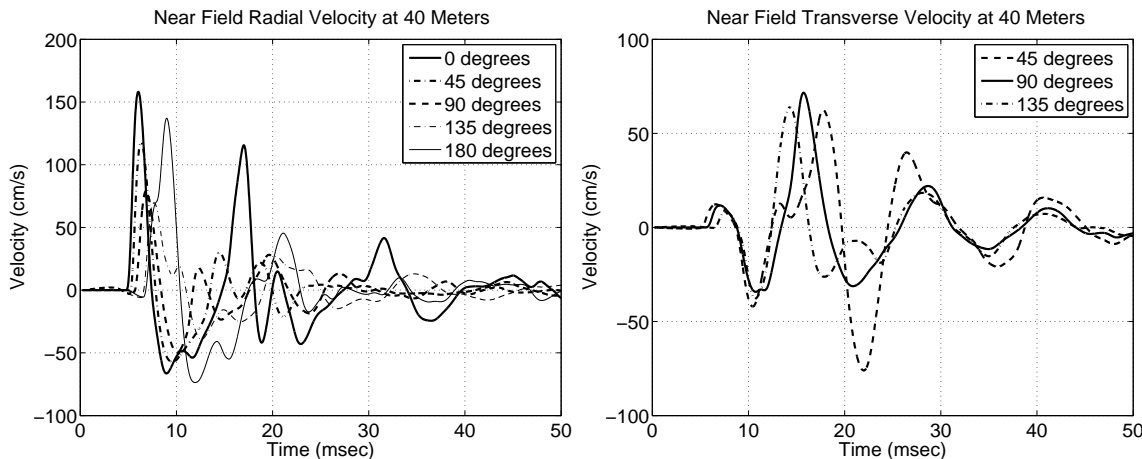


Figure 7. Radial and vertical velocity waveforms low pass filtered at 200 Hz at a distance of 40 meters from the cavity center.

3.9 Multiple reverberations

As a final example we consider the effect of multiple reverberations similar to those seen in the calculation above. The pressure pulses are stronger at the ends of the cavity, and decline in amplitude with each reverberation. We model the pressure field as a series of transient pressure pulses on each half of the cavity with maximum amplitude at zero and π , varying as $\cos\theta$:

$$\bar{P}(\theta, \omega) = \sum_{n=1}^N \frac{P_n \exp(-i\omega t_n)}{\gamma_n + i\omega} \cos \theta \quad 0 < \theta \leq \frac{\pi}{2} \quad (30)$$

$$\bar{P}(\theta, \omega) = -\sum_{m=1}^N \frac{P_m \exp(-i\omega t_m)}{\gamma_m + i\omega} \cos \theta \quad \frac{\pi}{2} < \theta \leq \pi \quad (31)$$

where the times correspond to successive reverberation times on opposite sides of the cavity. We also apply the final static pressure with the first pressure pulse on each side, and a compensating decaying pressure to conserve momentum as discussed in section 3.4. For ease of comparison, we use the same values of P_0 , P_1 and γ_1 as in the variable amplitude case. Multipole coefficients through $l=4$ were calculated. With $N=1$, corresponding to a single pressure pulse on each side, the results are similar to the earlier examples. With multiple reverberations, however, the waveforms are longer in duration and have more low frequency content. For this example, we use 10 reverberations, with P decaying exponentially with time as $\exp(-\gamma_0 t)$ with $\gamma_0=80$, and additionally decreasing 10% with each reflection. Decay coefficients follow equation 29 for each successive pair of pressure pulses on opposite sides of the cavity. Figure 8 shows the pressure at opposite ends of the cavity. The momentum compensating static pressure correction causes the early time offset in the pressure on opposite sides of the cavity.

Figure 9 shows the P and S waves at 45, 90 and 135 degrees. Notice the increase in low frequency amplitude and pulse duration compared to the earlier examples.

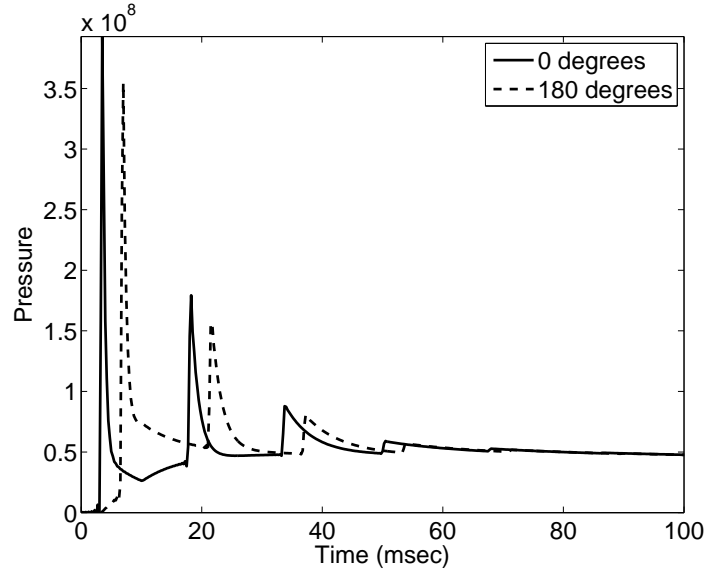


Figure 8. Pressure pulses at zero degrees and 180 degrees for the multiple reverberation example.

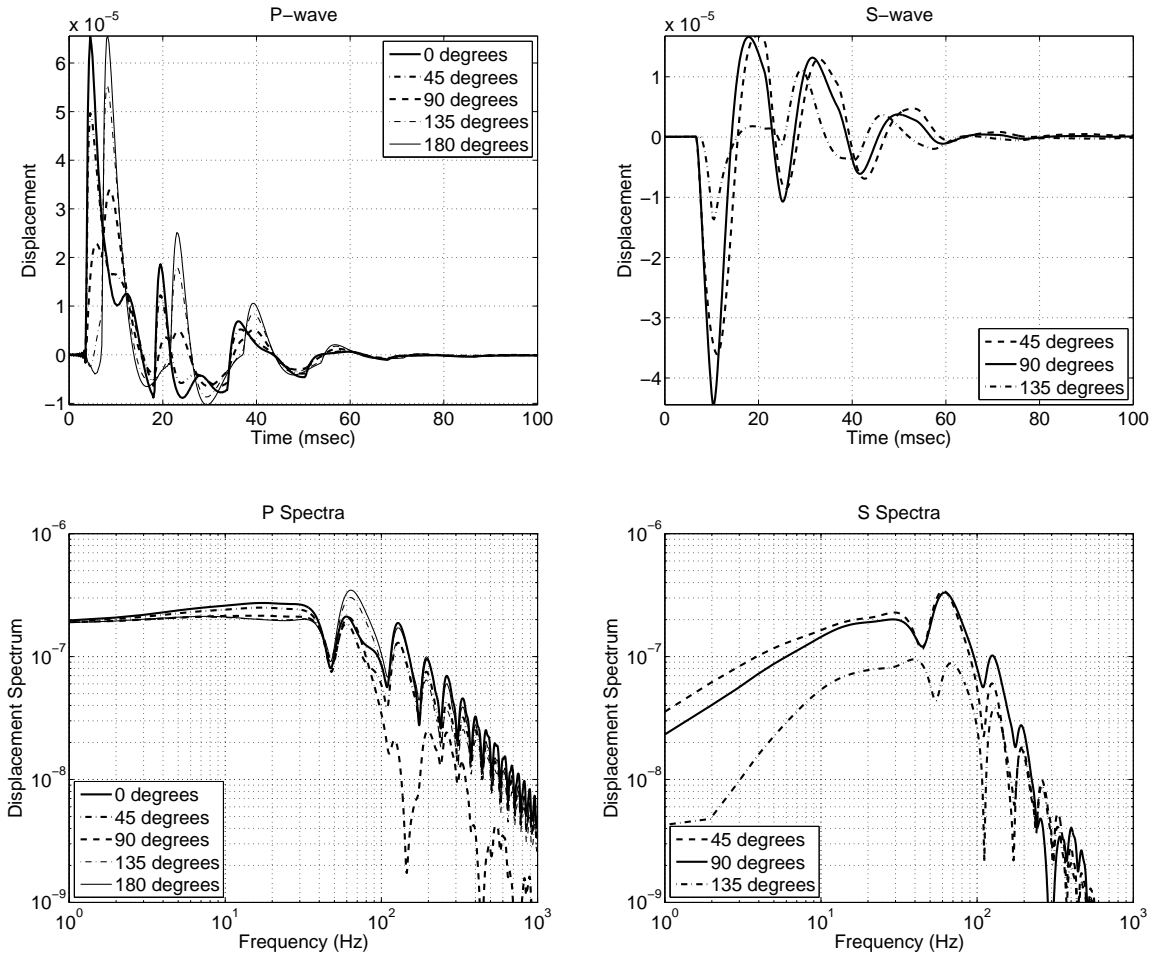


Figure 9. Far field P and S waveforms (top) and spectra (bottom) generated by the pressure pulses in Figure 8.

Figure 10 shows the spectra at 3 angles divided into its multipole components. In the earlier examples the $l=2$ (CLVD) component was negligible, but in this case because we made the pressure at the ends of the cavity larger than the sides, the CLVD component is significant, in fact comparable to the dipole component. Notice that at 45 degrees the dipole and CLVD components add constructively, increasing S, while at 135 degrees they add destructively, substantially reducing S at low frequencies. The CLVD component has a node at 90 degrees, so only the dipole component contributes to S at that angle. As shown in Figure 9, the radiation pattern of the combined waveform appears to be that of a dipole since the first motion is in the same direction at all three angles.

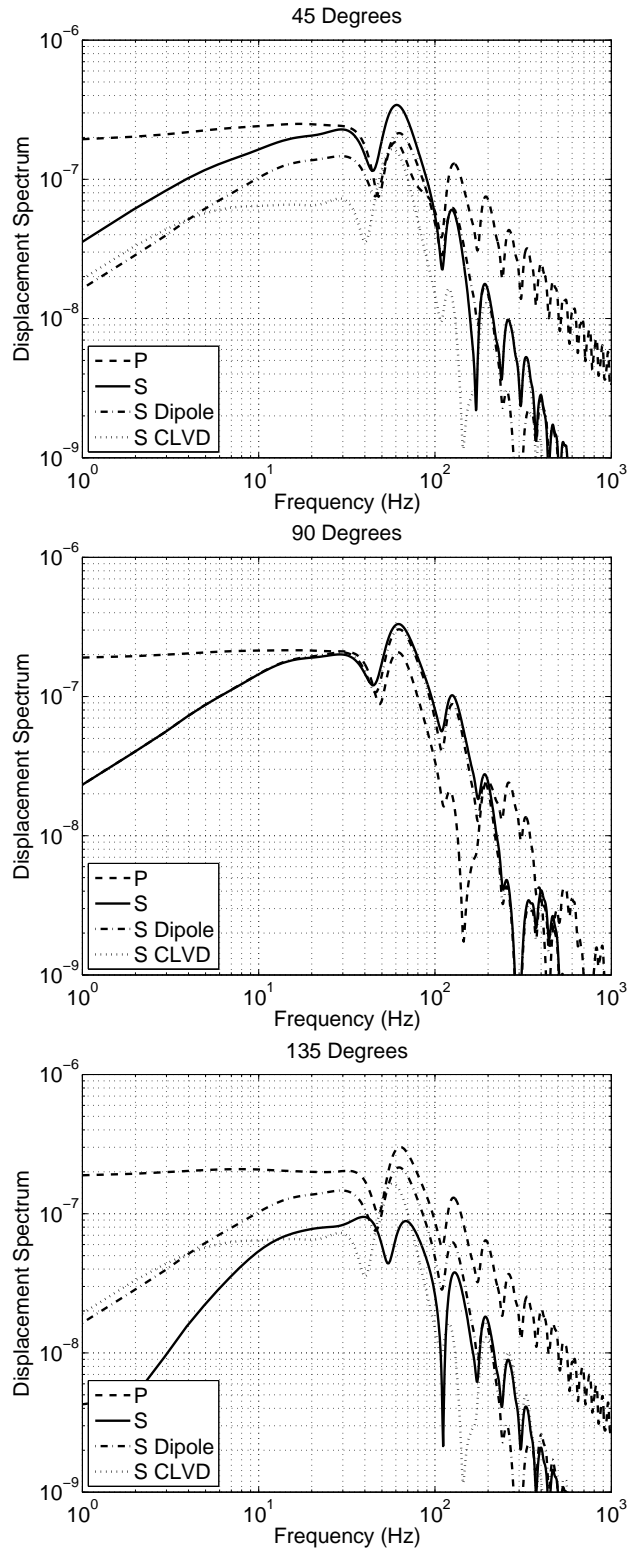


Figure 10. Composition of spectra at 3 angles: 45 degrees (top left), 90 degrees (top right) and 135 degrees (bottom).

3.10 Discussion and Conclusions

We have developed a general solution for seismic wave generation by an explosion source in a spherical cavity, and evaluated the solution for a point explosion offset from the cavity center. This offset causes a dipole component to the source which generates S waves and causes angular variation in P wave amplitude and shape. Zhao and Harkrider (1992) also found a dominant dipole component for an offset explosion embedded in a solid sphere. Depending on the distribution of the pressure field, the CLVD component to the source may also be significant. By conservation of momentum, the S waves must vanish at zero frequency but they may be a sizeable fraction of the P waves at frequencies of interest. We also performed a nonlinear axisymmetric calculation of an offset explosion in a spherical cavity. This leads to a much more complex pressure field on the cavity wall and correspondingly more complex near field waveforms. However the calculated S waves are comparable in amplitude (relative to P) to those found from the analytic solution. The longer duration of the source when cavity reverberations are included increases the low frequency content of the S waves.

Two chemical explosion tests with geometry very similar to that modeled in this paper provide a comparison with our theoretical results (Figure 11). The tests were conducted in Kirghizia in 1960 as part of a series described by Murphy et al (1997). In one test, one ton of explosives was detonated in the center of a spherical cavity. In another, one ton of explosives was detonated near the upper edge of the same cavity. Both were recorded at 5 km on the same instrument. The identical source and receiver locations make this a particularly good example. S waves may be generated by a variety of phase conversion and scattering processes, making isolation of source effects difficult in many cases, but here we can confidently attribute differences to the source offset. Based on the analysis given here, we would expect to see enhanced shear waves at higher frequencies from the off-center explosion. The low frequency spectra depend on the duration of the cavity reverberations, which is not well determined, but using the analysis presented in section 3.5 for the angle dependent amplitude with the same parameters, except for the smaller 4.92 meter cavity and material properties appropriate for limestone (P velocity 6000 m/s, S 3750 m/s, density 2700 kg/m³), leads to the spectra shown in Figure 12 for the offset source at a takeoff angle of 90°. Note that although both the P and S spectra peak at high frequencies, and the S spectrum goes to zero at zero frequency, the P and S spectra are comparable in amplitude at about 10 Hz. Figure 13 shows data for the centered and offset explosions recorded at 5 km, filtered in two bands from 2-8 Hz and 8-14 Hz and normalized by the vertical P-wave amplitude, as the off-center explosion was less decoupled. The data clearly show the expected enhancement of S waves in the 8-14 Hz frequency band for the offset source relative to the centered source.

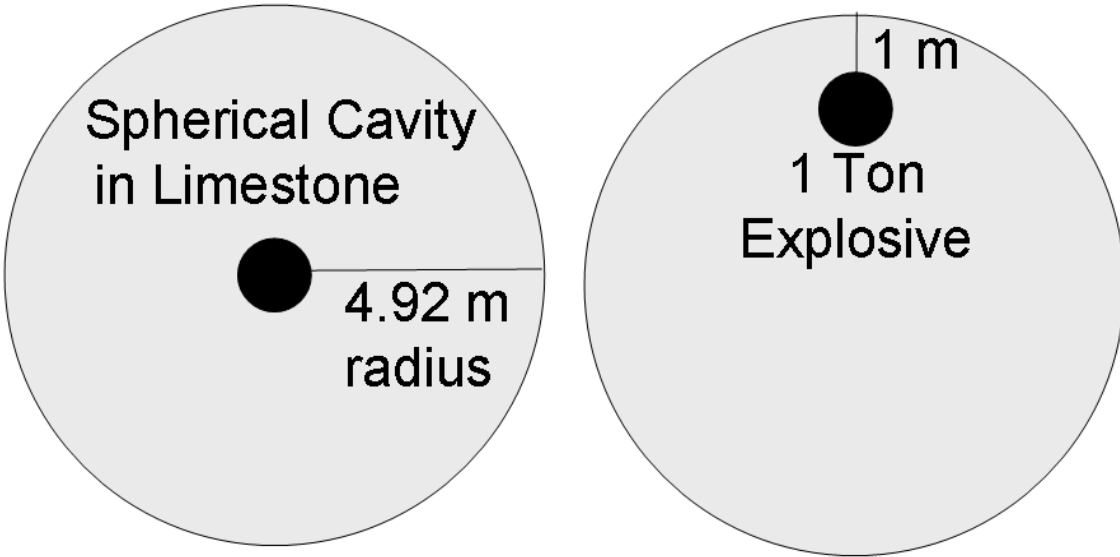


Figure 11. Configuration of Kirghizia explosions at the center and upper edge of a spherical cavity.

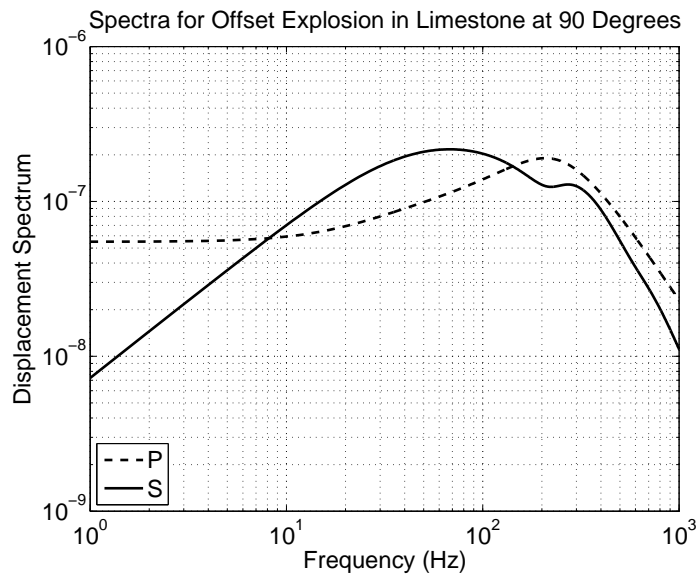


Figure 12. Calculated P and S spectra at 90 degrees (horizontally) from the offset source configuration shown in Figure 11.

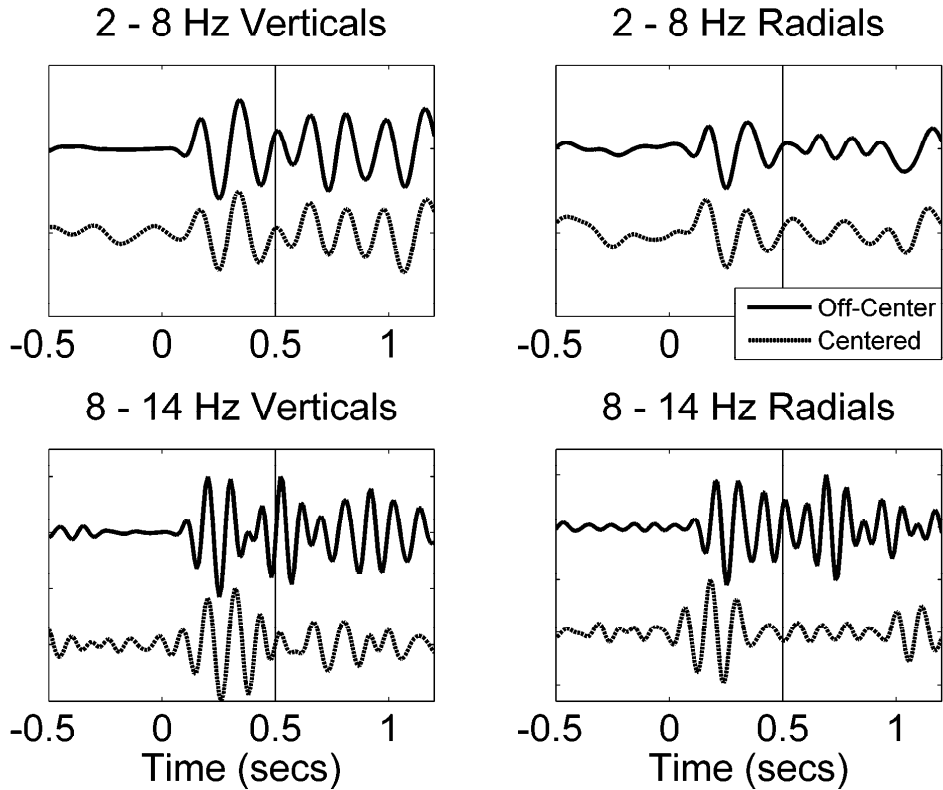


Figure 13. Vertical (left) and radial (right) components of data from the centered and offset Kirghizia explosions filtered from 2-8 Hz (top) and 8-14 Hz (bottom), scaled by the maximum vertical component amplitude. Increased shear waves are apparent in the higher frequency seismograms from the offset source.

The calculations performed earlier in this paper used parameters modeled after the Sterling explosion: 0.38 kiloton yield in a 17 meter cavity. The Sterling explosion was conducted in the cavity generated by the earlier 5.3 kiloton explosion Salmon in a salt dome. The cavity had a flat bottom due to melt that filled in approximately 7 meters at the base of the cavity (Healy et al, 1971). Consequently the bottom of the cavity was closer to the explosion source than the top, and so the calculations here are relevant to that explosion, although we are addressing the more general problem of shear wave generation and P-wave variations caused by an offset explosion source. A more complete treatment of the shear waves generated the Sterling explosion including calculations with the flat bottom using a realistic salt model is given by Xu et al (2009).

Although the solution given above strictly applies only to decoupled explosions, it may have relevance to tamped explosions as well. A tamped explosion is characterized by a pressure pulse that propagates through the surrounding medium causing nonlinear deformation of rock out to the elastic radius, which is an order of magnitude larger than the cavity radius. The tamped explosion source can also be expanded in spherical harmonics as with the decoupled source. Empirical explosion source models such as the Mueller-Murphy model (Mueller and Murphy, 1971) parameterize the explosion source as a spherically symmetric pressure pulse applied at the elastic radius. Propagation through heterogeneous media, as well as the effects of the free surface and gravity, cause angular variations in the explosion source function, so the tamped explosion source may be more accurately characterized as a multipole source. The conservation of

momentum constraints apply to a tamped source as well, and so the dipole component of the source must always vanish in the long period limit, however it may cause shear wave generation at higher frequencies of interest. In the examples given above, the CLVD source also vanished in the long period limit. This is because the final state of the pressurized cavity is uniform, however this is not necessarily the case for a tamped source and the CLVD (or other configurations of the $l=2$ multipole source including $m \neq 0$) may have a non-vanishing static limit for a tamped explosion caused by non-spherical permanent deformation.

4. SV GENERATION BY A VERTICALLY OFFSET EXPLOSION IN A SPHERICAL CAVITY

Abstract: A fully decoupled explosion detonated in the center of a spherical cavity is a purely compressional seismic source. Any shear waves observed in records of such explosions are the result of conversion from P and/or Rg phases at the free surface or other interfaces. A variety of asymmetries however, such as asphericity of the cavity or offset or asymmetry of the explosion, can lead to direct generation of shear waves. A pair of explosions in the same spherical cavity, one centered and one near the roof of the cavity, recorded at the same station 5 km away, provide a unique opportunity to investigate the effect of an offset source on shear wave generation through analysis of the seismograms and modeling of the observations.

4.1 Introduction

Understanding the generation of shear waves by decoupled explosions is important for nuclear monitoring, as their discrimination from earthquakes depends on their high frequency S to P ratios. It should also improve understanding of shear wave generation by explosions in general, as the extent and type of source asymmetry possible in decoupled explosions is quite constrained compared with tamped explosions.

Although we might expect a decoupled explosion in a spherical cavity to be a pure P-wave source, recent work has demonstrated not only that shear waves are observed from decoupled explosions, even in the near field, but that they can be generated at the source. The near-field S-wave radiation pattern of Sterling, a 5 kt nuclear explosion in a 29 m radius cavity in salt was first modeled by displacement and opening of a crack (Langston, 1983). More recently, Xu et al (2008) showed that the known asymmetry of the cavity, a flat floor due to melted and then recrystallized salt, leads to the observed shear waves. Further, the similarity of Sterling's coda with azimuth indicates that shear waves are generated at the source for some time. In a separate study of historical Soviet records from the Azgir test site, Baker et al (2009) showed that local shear waves from decoupled explosions in water-filled cavities in salt were generated at the source. Stevens and Baker (2009) showed via analytic and numerical simulations that an offset source in a spherical cavity will generate significant direct S-waves due to the variation in timing and amplitude of the shock wave on the cavity walls.

We compare records at 5 km from a centered and a vertically offset explosion in the same spherical cavity to predictions. Specifically, we identify an SV arrival in the off-center explosion records, investigate the frequency dependence of the arrival, and compare the observations with predictions for the known source parameters.

4.2 Data

The explosion pair of this study was part of a series of 22 decoupling tests performed in Kirghizia in 1960, in 5 separate chambers excavated within a homogeneous limestone formation. The cavities were inspected visually between explosions and showed no signs of damage, allowing multiple explosions to be detonated within a single cavity. Consistent scaling with yield confirmed the consistency of the cavities' responses through multiple explosions (Murphy, et. al, 1997). Two explosions of one ton of ammonium nitrate were detonated in the same 4.92 m

radius cavity at 292 m depth, one in the cavity's center and one one meter from the top of the cavity.

There is some small uncertainty regarding the density and yield of the explosive source, which was reported to be ammonium nitrate, but was also reported to have a density of $1,600 \text{ kg/m}^3$, which is nearly the density of crystalline ammonium nitrate. Ammonium nitrate prills, the common pelletized form used in fertilizer, have a bulk density of just 780 kg/m^3 , and are the explosive equivalent of 0.44 times as much TNT. Forms used for explosives are commonly less dense. Mixture of the ammonium nitrate with TNT on the other hand increases the density and the yield, but was unlikely to have been used for these events, as such a mixture was reported to have been used just for the two largest explosions in the series of tests. Fertilizer prills of ammonium nitrate therefore provide a lower bound on the explosive power of these events and are likely slightly more dense than the explosive used. Regardless of the exact yield, because both explosions were of the same yield, were detonated in the same chamber, which was undamaged by the explosions, and were recorded at the same 3-component station five kilometers from the source, we can be certain that differences between the waveforms are due to the relative positions of the sources within the chamber. The greatest possible variation in yield, or in placement of the explosive relative to the wall due to uncertainty of its density is not sufficient to vary the simulation results significantly. A one ton sphere of ammonium nitrate fertilizer prills would have a 0.67 m radius, so the explosion would have been centered 1.67 m from the cavity roof (Figure 15).

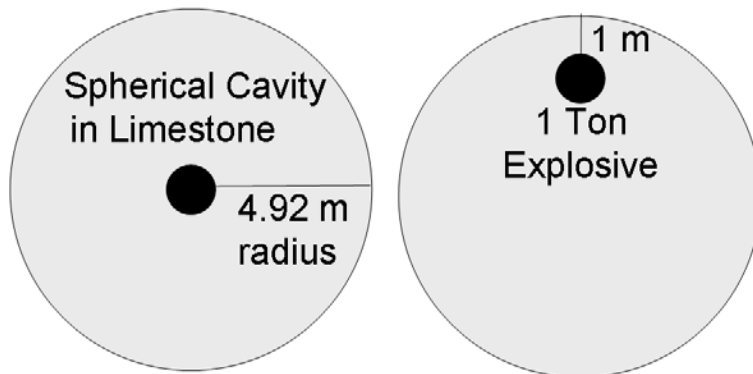


Figure 15. Configuration of the centered (left) and off-center (right) 1 ton explosion sources in the spherical cavity. The explosive source is on scale relative to the cavity size.

Two factors suggest that both explosions might act as spherical seismic sources. First, Murphy et al (1997), using near field peak amplitudes, found the centered explosion to be fully decoupled, and the off-center explosion nearly so, with amplitudes approximately twice as large as those of the centered explosion. Second, the explosions were overburied, which normally produces a spherical source even from a tampered explosion. Specifically, a tampered explosion of one ton of TNT at 292 meters depth would be 24 times overburied, and this ignores the decoupling factor, which Murphy et al (1997) found to be approximately 10 at 10 Hz for the off-center explosion, and it ignores the reduced yield of ammonium nitrate relative to TNT.

4.3 Analysis

Figure 15 shows the vertical component acceleration spectra at 5 km of each event. Amplitudes are similar at low frequencies, but the decoupling effectiveness for the off-center explosion drops dramatically at higher frequencies. This is consistent with the near field observations at lower frequency of Murphy et al. (1997), who found a factor of two difference in near field peak amplitudes, and different, complex spectral curves for the off-centered explosion compared with other centered, decoupled explosions at high frequencies. Their spectral comparison was with centered explosions in other cavities because no near field records were available from the centered explosion in the same cavity. The spectral curves in Figure 15 separate at approximately 7 Hz. The records are hand digitized, so the upper limit of their resolution is not well-defined. Similarity of the waveforms on different components indicates that the off-center records are reliable up to at least 15 Hz. For the centered explosion, the same measures plus similarity of the same components of different events' recordings indicates that the records are reliable to at least 12 Hz.

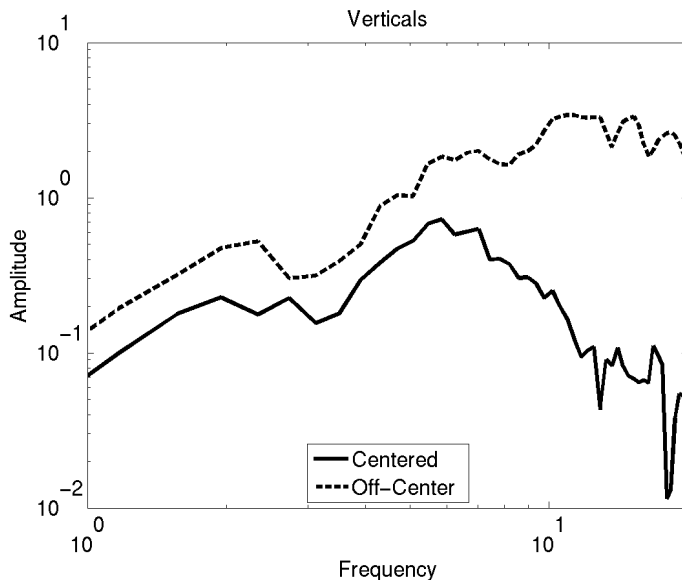


Figure 15. Vertical component acceleration spectra of the centered (black) and off-center (dashed) explosions at 5 km.

Figure 16 shows the centered explosion displacement seismograms (black dashed) overlaying the off-center explosion (red) records. All three components of the seismograms are scaled by the maximum vertical component amplitude in each passband. At 2 to 8 Hz, the waveforms of the two explosions are nearly identical on all three components (Figure 16, top row). With a bandpass filter high frequency corner greater than 8 Hz, the waveforms become dissimilar. At 8 to 14 Hz (Figure 16, bottom row), there is very significant additional energy on the vertical and radial components at approximately 0.5 seconds after the P, which is the predicted S minus P time. Seismograms are aligned with the initial P at zero seconds.

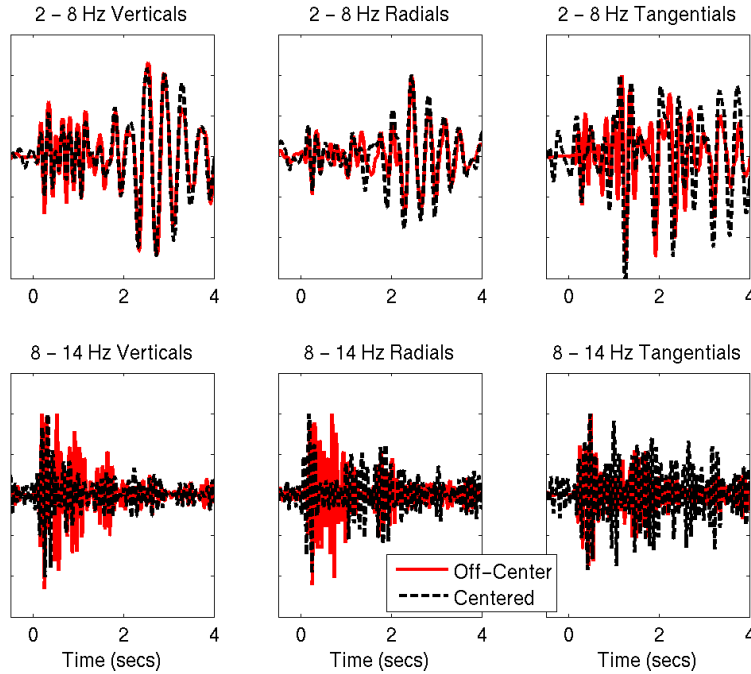


Figure 16. Three component seismograms of the centered (black) and off-center (red) explosion at 2-8 Hz (top row) and 8-14 Hz (lower row), scaled by the maximum vertical component amplitude to account for decoupling. P waves are aligned at zero.

Besides the arrival time, the particle motion can identify the phase. Figure 17 shows the overlain Hilbert transformed radial (dashed) and vertical (solid) seismograms of the off-center (lower) explosion records at 8 to 14 Hz. The additional phase in the off-center explosion records has retrograde motion, indicated by the alignment of the Hilbert transformed radial with the vertical, consistent with its identification as a higher mode Rayleigh wave, or equivalently, as an S-wave.

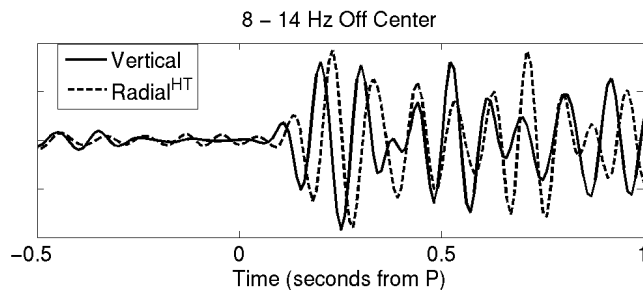


Figure 17. Vertical (solid) and Hilbert transformed radial (dashed) records of the off-center explosion at 8-14 Hz. The additional phase in the off-center records has retrograde motion.

The seismograms in Figure 16 were scaled by the maximum vertical component amplitude so that amplitude differences due to reduced decoupling of the off-center explosion would not obscure the similarities and differences of the records. That highlighted the S-to-P differences between events. We also want to separate the effect of changes in the S amplitude relative to P from the effect of decoupling and the instrument response. To do so we plot spectral amplitude ratios. First, we plot the ratios of the off-center explosion's P and S spectra to those of the

centered explosion (Figure 18). Strong P coda appears to overlap the S arrival, so the S spectrum represents an upper bound, particularly for the centered explosion. This removes the instrument response and indicates that the difference in decoupling between events is similar for both phases, with the decoupling factor decreasing dramatically above 10 Hz. This observation will provide a secondary basis for distinguishing between mechanisms for the S-wave generation (the main factors being the existence of the SV in the off-center records and the frequency at which it emerges relative to P).

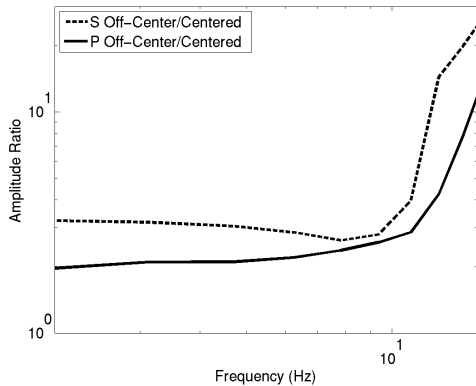


Figure 18. Ratios of P (solid) and S waves (dashed) of the off-center to the centered amplitude spectra (right). Spectra are averages of the radial and vertical components.

We also plot the ratio of the S spectra from the off-center vs. the centered explosion, normalized by the ratio of the off-center to centered P spectra (Figure 19). The latter ratio provides normalization as a function of frequency for decoupling of each event. This will be valid if decoupling of the S-wave is the same as that of P, so would be valid for S-waves generated within the cavity, but not necessarily for S-waves generated by deformation outside the cavity walls. Because no distinct S-wave stands out in the centered explosion record, its S spectra largely represents the P-coda and so provides an upper bound, so the S off-centered to centered ratio represents a lower bound on the true value. Nonetheless it is interesting to see that the off-centered explosion S-wave begins to increase relative to that of the centered explosion at 9 Hz, similar to the 8 Hz frequency at which the S-wave seems to emerge in bandpass filtered seismograms.

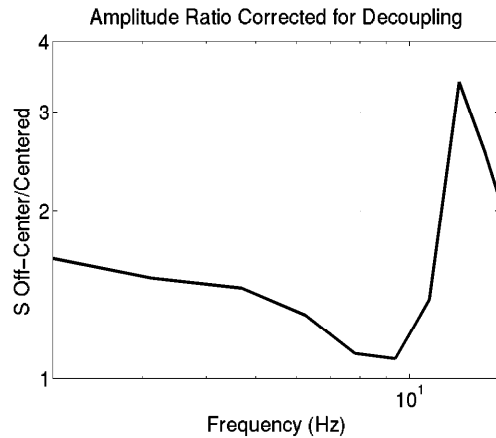


Figure 19. Ratio of off-centered to centered explosion S spectra. The ratio is normalized by the off-centered to centered explosion P spectra to account for decoupling. Spectra are averages of the radial and vertical components.

We conclude that the additional arrival in the off-center explosion records is a shear wave generated at the source. It cannot have been scattered from P or Rg, as the cavity and stations are the same for both explosions. From Figure 16 (bottom right), we see that the phase is entirely SV. That is, there is no additional arrival on the tangential component of the off-center explosion record compared with that of the centered explosion, consistent with predictions for a vertically offset source (Stevens and Baker, 2009).

4.4 Modeling

The observation of an additional SV arrival in the off-center explosion records is consistent with Stevens and Baker (2009) demonstration that a vertically offset source will produce SV, but not SH waves, due to variations in timing and amplitude of the initial shock wave and its reverberations within the cavity. Another possible source of shear waves is asymmetric nonlinear deformation outside of the cavity. We perform simulations to test both mechanisms. We use one ton of TNT on the source, as that is an upper bound on the likely yield, and so places an upper bound on the nonlinear deformation outside of the cavity. The difference in yield between TNT and ammonium nitrate makes no significant difference to the shear wave amplitudes relative to the P-waves generated by reverberations within the cavity.

4.4.1 Shear wave generation by nonlinear deformation

To assess the possible effect of nonlinear deformation outside the cavity we perform a series of calculations. We begin with the Eulerian finite difference code used to perform the calculations in Stevens (2009). This makes a nonlinear axisymmetric calculation of an explosion in a 4.9 meter radius air-filled cavity, offset from the wall by 1.67 meters. We then overlay that result into a 2D, axisymmetric, Lagrangian, finite difference calculation to propagate the nonlinear shock through the solid material after the cavity pressure history has been determined. The stresses and displacements are saved on a monitoring surface outside of the nonlinear region, and are used as the starting conditions for wavenumber integration synthetics, which propagate the solution to 5 km.

Figure 20 shows the areas of nonlinear deformation around the cavity for each explosion. The nonlinear yield region of the centered explosion only extends one or two grid cells into the limestone from the cavity wall (left), consistent with earlier observations of full decoupling (Murphy, et al., 1997). There is, however, a small area of nonlinear deformation extending 5 meters from the top of the cavity for the off-center simulation (right).

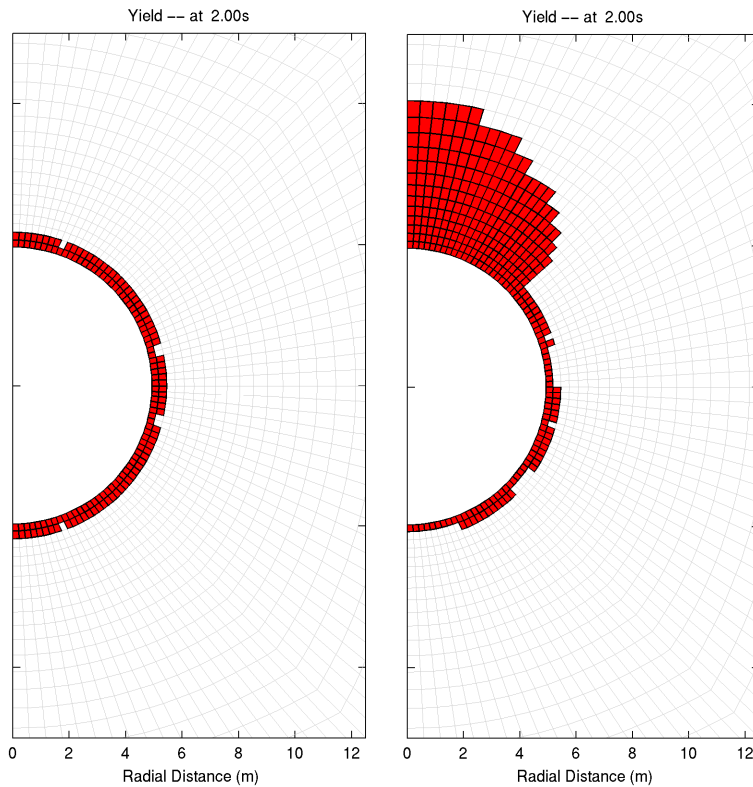


Figure 20. Nonlinear yield regions (right column) for the centered (upper row) and off-center (lower row) explosions.

Figure 21 shows the synthetic seismograms and spectra. These results match the general characteristics of some observations, but fail badly in the details. The waveforms are similar at lower frequencies, the off-center explosion produces an additional SV but not SH arrival at higher frequencies, and the ratios of the off-center explosion's S and P-waves to the centered explosion's S and P waves both increase at higher frequency. The frequencies, however, at which those ratios increase are significantly higher than those observed. Even at 10-20 Hz, the seismograms are identical (Figure 21, left). The ratios of off-center to centered explosion spectra show that the off-center P-waves become larger than those of the centered explosion at approximately 30 Hz (Figure 21, 2nd from left). The off-center explosion's S-wave only starts to become larger than the centered explosion's S-wave at approximately 60 Hz. This compares poorly with the observed P and S waves of the actual off-center explosion, both of which increase in amplitude relative to those of the centered explosion at 10 Hz (Figure 18) due to reduced decoupling, with the S-wave amplitude increasing more than that of the P-wave due to additional S-wave being generated (Figure 19). There is only a narrow passband, approximately

95 to 115 Hz, where the synthetic S waves from the off-center explosion increase in amplitude relative to the centered explosion more than the P waves do. The right hand plot shows seismograms in that passband.

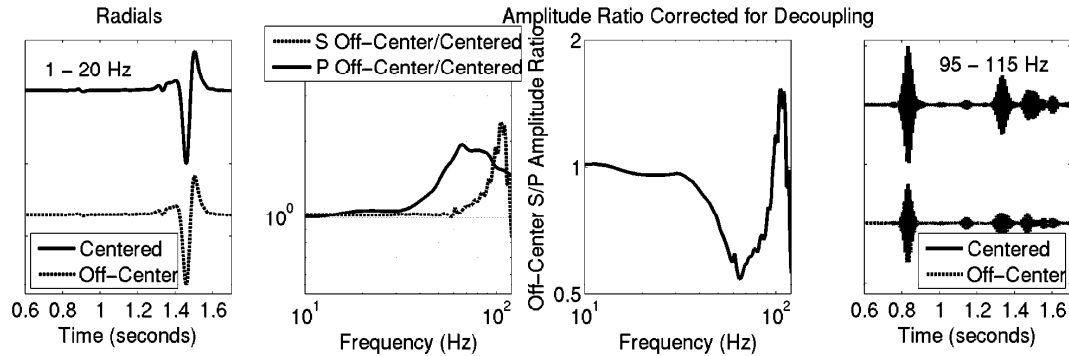


Figure 21. Radial synthetic seismograms at 5 km, at 1-20 Hz (left) and 95-115 Hz (2nd from right) for the off-center (solid) and centered (dashed) explosions, ratios of off-center to centered explosion S (dashed) and P (solid) amplitude spectra (2nd from left), and the ratio of the off-centered to centered explosion S spectra normalized by the off-centered to centered explosion P spectra to account for decoupling. Off-center and centered synthetic seismograms are on the same scale within each plot.

4.4.2 Shear wave generation by reverberations within the cavity

For the solution of the Eulerian calculation of the explosion in the cavity to provide the starting conditions for the Lagrangian calculation, it is cut off at an early time, before the energy can propagate beyond the model edges. This is also before multiple reverberations can occur, so the previous calculation only models the effect of nonlinear deformation. There is however strong empirical evidence for long-lasting resonance within a cavity in nearfield Sterling records, where coda dominated by a 55 Hz oscillation was identified as a result of cavity reverberations. The resonance continues very strongly for 10 cycles, with reverberations of slowly diminishing amplitude continuing much longer. To simulate the effect of multiple reverberations we perform analytic simulations similar to those of Stevens and Baker (2009). There is more than a factor of three difference in amplitude of the P-wave above and below the cavity due to proximity of the source to the top (Figure 22, left). That sets up a strong dipole moment, which must go to zero at zero frequency, but which can generate large S-waves at higher frequencies (Figure 22, right). The presence of low frequency S-waves depends on the time over which the reverberations remain significant. We use a conservative exponential decay rate proportional to the travel time across the cavity. Even so, the P and S far field source spectra for such reverberations are consistent with the observations at 5 km. The synthetic S-wave generated at the source is much smaller than P at low frequencies, so the centered and off-center explosion synthetics are dominated by the P-waves, which are similar. The amplitude of the S-wave generated by the dipole increases with frequency, surpassing the P-wave amplitude at approximately 8 Hz, consistent with the observations (Figure 23).

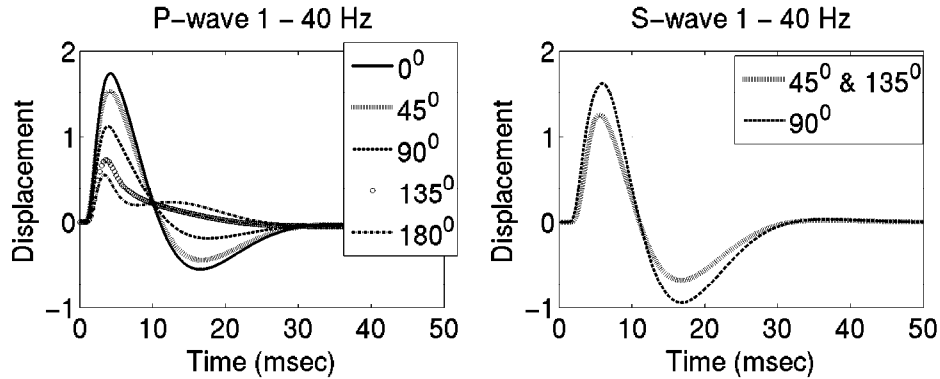


Figure 22. Synthetic far field P (left) and S (right) waves at different incidences from the vertical, due to amplitude variations resulting from the proximity of the offset source shown in Figure 14 to different locations on the cavity wall. Records are filtered from 1 to 40 Hz.

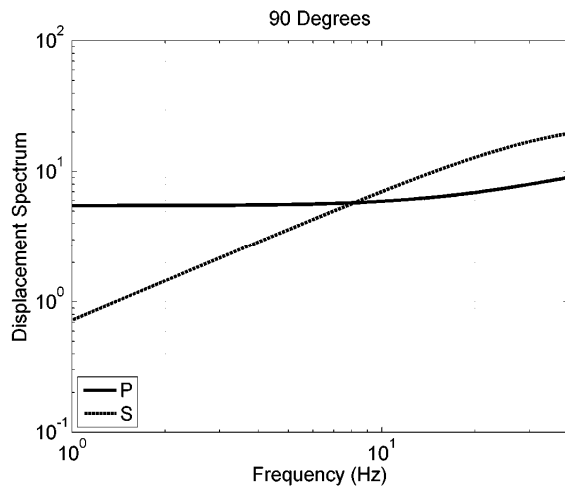


Figure 23. Synthetic far field P (solid) and S (dashed) spectra due to amplitude variations around the cavity resulting from the offset source shown in Figure 14.

4.5 Discussion and Conclusions

Comparison of seismograms at 5 km from two separate explosions in a spherical cavity, one detonated in the center, and one near the roof, show that the off-center explosion generated S waves not generated by the centered explosion. Because the cavity in which the explosions were detonated and the station are unchanged the SV must be due to the offset of the source within the cavity.

Variations in amplitude of the reverberating shock wave around the cavity produce a dipole component to the source, which reproduces the vertically polarized S wave of the off-center explosion records that emerges at approximately 8 Hz. The nonlinear deformation outside the cavity causes differences at very high frequency between the seismograms of the centered and off-center sources, but does not reproduce the observations.

This result is important to monitoring of decoupled explosions, as it demonstrates that large S-waves are generated at frequencies observed at local and regional distances by a nearly fully

decoupled explosion offset from the center of a spherical cavity. Such an explosion may in fact prove more difficult to identify, as the high frequency S-to-P ratio will be more earthquake-like than that of a similar tamped explosion. Purposely offsetting the explosive source in a decoupled test could prove to be a more effective evasion scenario than centering the explosion, even if the decoupling factor is reduced. The increase in S relative to P spectra with frequency, however, is opposite of that observed for both tamped explosions and earthquakes, which typically have lower S-wave than P-wave corner frequencies (e.g. Brune, 1970 for earthquakes; Fisk, 2006 for explosions), and so may be used to identify decoupled explosions such as this.

The observations and modeling also bear on explosion shear wave generation in general, as they demonstrate that a modest amount of a simple type of asymmetry can generate S-waves at frequencies important for monitoring. This suggests that many other types of asymmetry, perhaps less pronounced than had been assumed necessary, could be responsible for the shear waves generated from tamped explosions.

5. AN ANALYSIS OF SHEAR WAVES GENERATED BY THE STERLING EXPLOSION

Abstract: We show that the near field shear waves from the decoupled explosion Sterling were likely caused by the cavity shape, which was approximately spherical except for a flat floor due to melted and recrystallized salt. We model the impact of the explosion shock wave on the cavity walls using a 2D Eulerian finite difference code that simulates the evolution of the air shock in the cavity coupled with 2D Lagrangian finite difference code that simulates the nonlinear region outside the cavity. Calculated shear waves generated by the asymmetric impact of the shock wave on the cavity walls match the observed initial shear wave amplitudes and radiation pattern. The observations also have substantial P and S coda, which are not reproduced by the calculations. Similarity of coda waveforms with distance indicates their source is at or very near the cavity. Longer time modeling of the air shock evolution appears to produce a more realistic source function and provide a better match to the coda, and indicates that the coda are caused by air reverberations between the top and bottom of the cavity. We assess the likelihood that fractures created by the tamped explosion that formed the cavity, Salmon, were re-opened by Sterling. Modeling of hydrofracture propagation driven by the Sterling explosion, by coupling stress wave dynamics in rock with fluid mechanics in the fractures, shows that the cavity pressure is insufficient to overcome the overburden to propagate fractures into rock, except for the area immediately below the explosion on the cavity floor.

5.1. Introduction

Research on discrimination of tamped explosions from earthquakes has been extensively conducted for decades. Various models of both earthquakes and explosion sources have been proposed, and many methods have been developed to discriminate underground explosions from earthquakes. Those depend mainly upon the characteristics of the seismic signal observed at teleseismic and regional distances (e.g., Brune & Pomeroy, 1963; Masse, 1981; Denny and Johnson, 1991; Murphy 1977). However, detonation of a nuclear explosion in a large cavity to decouple the source from the surrounding medium and so evade detection has been a longstanding challenging issue for nuclear monitoring (e.g., Latter et al., 1961; Murphy et al. 1997). The commonly used and most reliable discriminants for events in the magnitude range of decoupled explosions are high frequency spectral ratios of the amplitudes of the seismic shear phases S_n and L_g to P_n or P_g , with explosions in general having lower S/P ratios than earthquakes because of differences in the source characteristics (e.g. Taylor, 1991). Although there have been many investigations related to decoupled explosions (eg., Denny and Goodman, 1990; Glenn and Goldstein, 1994; Murphy et al, 1997), they have focused on the effect of decoupling on P-wave amplitudes. How shear waves originate, especially from decoupled explosions in spherical cavities, is not clear. Understanding shear wave generation by decoupled and partially coupled explosions is necessary to ensure correct identification by discriminants that depend on shear wave amplitudes.

For a perfect spherical cavity large enough to decouple the explosion, a nuclear explosion detonated exactly at the center would generate no shear waves in a homogeneous medium. Shear waves, however, have been observed from all decoupled explosions, even quite close to explosion sources such as the Sterling event (Perret, 1968). A decoupled explosion detonated in

air away from the cavity wall generates an air shock wave, an isotropic dilatational wave, propagating toward the cavity wall that would not excite other wave types in the absence of the cavity wall. Candidates for the observed shear wave generation in the near field should include: 1) asymmetry in the explosive-cavity system (such as an off-center explosion in a spherical cavity, or a centered explosion in a nonspherical cavity) so that the shock waves impact the wall at different times and strength; 2) partially coupled explosions generate cracks or open existing cracks more readily than tamped explosions; 3) heterogeneities surrounding the cavity convert the compressional waves into shear waves.

The Salmon and Sterling explosions are particularly useful for investigating shear wave generation in a decoupled explosion because they were set off in simple salt at the same location, the near field was well instrumented, and the source characteristics have been widely investigated (e.g., Gupta and Kisslinger, 1964; Patterson, 1966; Murphy, 1969, Perret, 1968, Healy et al. 1971, Langston 1983, Glenn and Denny, 1987, Denny and Goodman 1989; Stevens et al., 1991c). The Salmon event was 5.3 kt and excavated a cavity in which the Sterling event of 0.38kt was detonated. This pair of nuclear explosions was designed to provide a test of the concept of seismic decoupling under realistic conditions. Both devices were emplaced at 827.8m (the overburden is about 180bars) in a salt dome and the explosions were recorded on a common set of instruments. The structure between the source and receivers is so simple, consisting of nearly homogeneous salt, that the limited reflections and conversions are easily recognized. The post-Salmon cavity was found to be approximately spherical with a 17m radius, except where a pool of molten salt recrystallized in the bottom of the cavity forming a flat floor approximately 10m from the center. The Salmon cavity wall was damaged and cracked (Perret 1968). 0.21 kt is the maximum yield for which an explosion in the Sterling cavity would be fully decoupled (Denny and Goodman 1990) and so the cavity wall was slightly overdriven by the 0.38 kt Sterling explosion.

Shear waves are not apparent in the Salmon nearfield records but are observed in the Sterling nearfield records (Perret, 1968). The Salmon device vaporized and melted the surrounding salt, creating a spherical cavity and generating stress waves radially propagating outward by the explosive gases, and its nearfield records are dominated by compressional waves. In the Sterling configuration, on the other hand, the nuclear explosive pressure waves reached the flat floor and spherical wall at different times and strengths, resulting in nonspherically-symmetric effects such as the SV wave generation evident in the near cavity observations. To explain the observed SV waves, Perret (1968a) suggested that they were generated from a fundamental asymmetry in shock pressure on the cavity walls, and Langston (1983) constructed kinematic source models to fit the P and SV observations. His results suggest that the SV waves were radiated primarily by induced normal faulting occurring beneath the cavity rather than by an asymmetric pressure distribution due to the preshot cavity geometry.

The main purpose of this paper is to investigate the possible mechanisms for the observed shear wave generation by Sterling. Instead of using the approximately analytical methods for elastic models (e.g., Perret, Langston, Healy), we use numerical methods to analyze the interaction between the shock wave and the surrounding media for the Salmon/Sterling events in two dimensions and to provide insight into the shock wave propagation and its nearfield effects. Denny and Goodman (1990) simulated the elastic-plastic behavior of salt in nuclear explosions with a simple one-dimensional finite difference code using the Grüneisen equation of state to describe the high pressure behavior of salt, but did not directly compare the observations with the

numerical simulations. Because the Salmon records in the nearfield are composed of mainly compressional waves, Rimer and Cherry (1982) adopted a constitutive relation combining a limiting yield strength with quadratic work hardening and softening and modeled spherical wave propagation using a nonlinear elastic-plastic finite difference method and noted a reasonable fit to the Salmon data including attenuation and a precursor. The actual environment in which the explosions take place is not uniform, and the cavity is not always perfectly spherical, so a one-dimensional simulation is insufficient to reveal all the explosion source characteristics such as spall and material boundary effects (Murphy, 1991; Stevens et al, 1991d). In this study we extend the numerical simulations to two dimensions to include all the material layers above the shot level and the spallation and wave propagation through material boundaries. The numerical method uses the two-dimensional axisymmetric Lagrangian finite difference code (CRAM) with gravitation to model wave propagation in salt. The algorithms are described in detail by Wilkins (1964). For the Sterling event an Eulerian finite difference code STELLAR is coupled with CRAM to model the air-salt interaction. Both codes have been successfully used for modeling explosions in different media in previous studies (e.g., Stevens et al, 1991c). The numerical results are compared with the observations in the near field and at local distances in our study.

In the following sections we first briefly review the salt material properties because they are critical in modeling the salt behavior at intermediate strain and modeling the nearfield recordings. Then we simulate the tamped Salmon event and compare the near-field synthetics with borehole observations in two dimensions. The material parameters derived from the Salmon simulation are used for the small yield decoupled Sterling event. Next we model the Sterling decoupled event in the actual nonspherical geometry and demonstrate that the shear waves can be generated by the cavity asymmetry. The Sterling nearfield recordings are also analyzed in detail to reveal the likely shear wave generation sources.

In the following the velocity seismograms are either obtained by integration of the records from the acceleration gauges or directly from the velocity gauges, and the records have been reviewed to ensure that they are consistent with those published (Perret, 1968; Langston, 1983; Murphy 1977). In the numerical calculations, the shot point is taken as the origin of the coordinates, the radial component is calculated with respect to it, and the tangential component is in the vertical (SV) plane, perpendicular to the radial, with positive pointing upward consistent with Langston (1983). The original observations in the horizontal-radial and vertical directions have been translated into the radial and tangential directions as we defined above.

5.2 Review of salt material properties

The properties of salt in the moderate strain regime are important in understanding wave propagation due to explosions. A variety of salt models have been used. A simple linear incompressible model was used by Perret (1968) to estimate the Salmon cavity radius from the measured permanent displacement. However, nonlinear behavior was found to persist to very low strains (10^{-8}) (McCartor and Wortman, 1990). Inelasticity of salt at high strains was investigated on the laboratory scale (Heard et al, 1975; Larson, 1982). At higher strains, salt is found to behave nonlinearly and its attenuation increases with the strain amplitude. The Salmon near-field recordings showed the strain-dependent attenuation as well (e.g., Gupta and McLaughlin, 1989; McCartor and Wortman 1985). The precursors in the nearfield Salmon records have a constant value of about 0.3m/s but the latter peak amplitudes drop rapidly with range, indicating a plastic wave following the elastic wave precursor (Rimer and Cherry, 1982).

In modeling nonlinear wave propagation in spherical symmetric salt, Patterson (1966) used a salt-crushing strength model, Denny and Goodman (1990) adopted the Grüneisen equation of state to describe the high pressure behavior of salt for the finite difference calculation while the plastic flow is assumed to be governed by the von Mises criterion with a limit on shear strength of 400 bars, Wortman and McCartor (1989) proposed a nonlinear model for partial shear failure which is designed to account for the Salmon attenuation and precursor. In their model, the shear modulus is permanently and instantly reduced by 80% in any material element once the compressional strain level exceeds 10^{-4} . Glenn and Goldstein (1994) derived an empirical strain hardening model for Tatum salt from plastic wave speed data recorded during the Salmon event. An empirical laboratory salt model was also used by Stevens et al. (1991c) to carry out a series of coupled radiation/hydrodynamic simulations of the Sterling event.

Rimer and Cherry (1982) successfully modeled the Salmon explosion event in the one-dimensional spherical case, including the precursors in the nearfield records, and found that ground motion data was best modeled by using the salt work-softening-hardening model, which is required in order to explain the small amplitude “elastic” precursor. In their model, the salt strength is represented as a function of the plastic work done on the salt, $Y = Y_0(1 + e_1 E - e_2 E^2) \leq Y_{Lim}$, where Y_0 is the initial strength, Y_{Lim} is the limiting yield strength and e_1 and e_2 are respectively work hardening and work softening parameters. The yield strength initially increases as inelastic energy E is absorbed by shear failure in a manner quadratic in this inelastic energy. For Salmon, the parameters are as follows:

$$Y_0 = 2.5MPa, Y_{Lim} = 68MPa, e_1 = 6 \times 10^{-4} m^3 / J, e_2 = 10^{-10} m^6 / J^2$$

This model strongly suggests that shear failure plays a strong role in the nonlinear behavior of salt at moderate strains. The same constitutive functional is applied well to other Grand Saline events e.g., GNOME and COWBOY. In this study we choose this empirical constitutive model because it provides a reasonable fit to the near-field Salmon data (Rimer and Cherry 1982), including attenuation and precursors, and is also consistent with cube root scaling.

5.3 Numerical simulations of the Salmon explosion

As the first step, we simulate the tamped 5.3kt Salmon explosion and compare the synthetics with data in order to confirm the applicability of the model parameters obtained in the one-dimensional spherical scenario by Rimer and Cherry (1982). A two-dimensional axisymmetric finite difference grid is set up to model the tamped event in a realistic scenario. The grid spacing is sufficient to resolve up to 100Hz. The nuclear explosion is modeled by depositing this energy in about 68 tonnes/kt of vaporized rock as an initial condition at the shot point. The geometry of the source and receivers used in this study is shown in Figure 24. The details of borehole instrumentation for the tests are discussed by Perret (1968). The instruments are located over an azimuth range of about 55° , but for our purposes we treat them as being in a single vertical plane, with the vertical and horizontal-radial recordings rotated into the radial and tangential components as defined above.

The Salmon structure model consists of four layers, sediment, limestone, anhydrite and salt and their properties are listed in Table 1 (Murphy, 1991, Perret, 1968). The top sedimentary layer consists of mainly sands, clays and shales and is thus weak material. The cavernous limestone

and anhydrite cap rock above the salt dome, are hard rock layers, and the salt is slightly weaker than the hard rock layers. The salt is modeled using the Rimer and Cherry (1982) constitutive values and the limestone and anhydrite layers are modeled as elastic, but the sediment layer is modeled as a nonlinear inelastic material with spall caused by the explosion.

Table 1. Salmon Structure Model Parameters (Murphy 1991)

Material	Thickness (m)	Vp(m/s)	Vs (m/s)	Density(kg/m ³)
Sediment	270	1900	762	2000
Limestone	50	3500	1880	2470
Anhydrite	140	5650	3150	2770
Salt	1000	4670	2550	2200

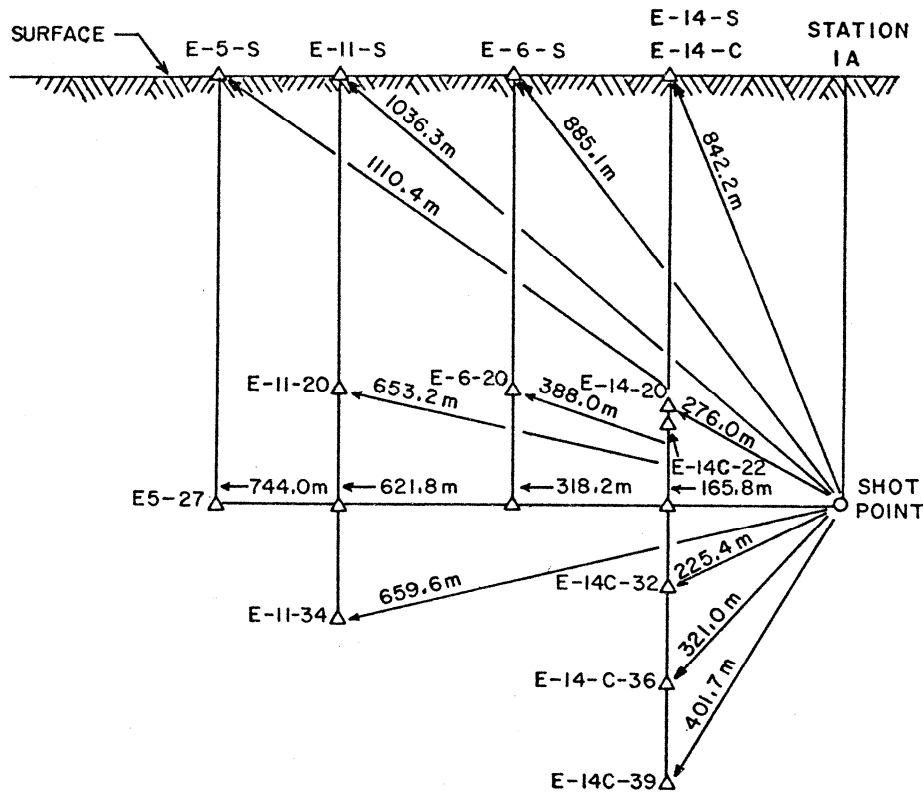


Figure 24. Locations of near field strong motion instruments. This figure is reproduced from the paper by Healy et al (1971). The shot depth is 828m.

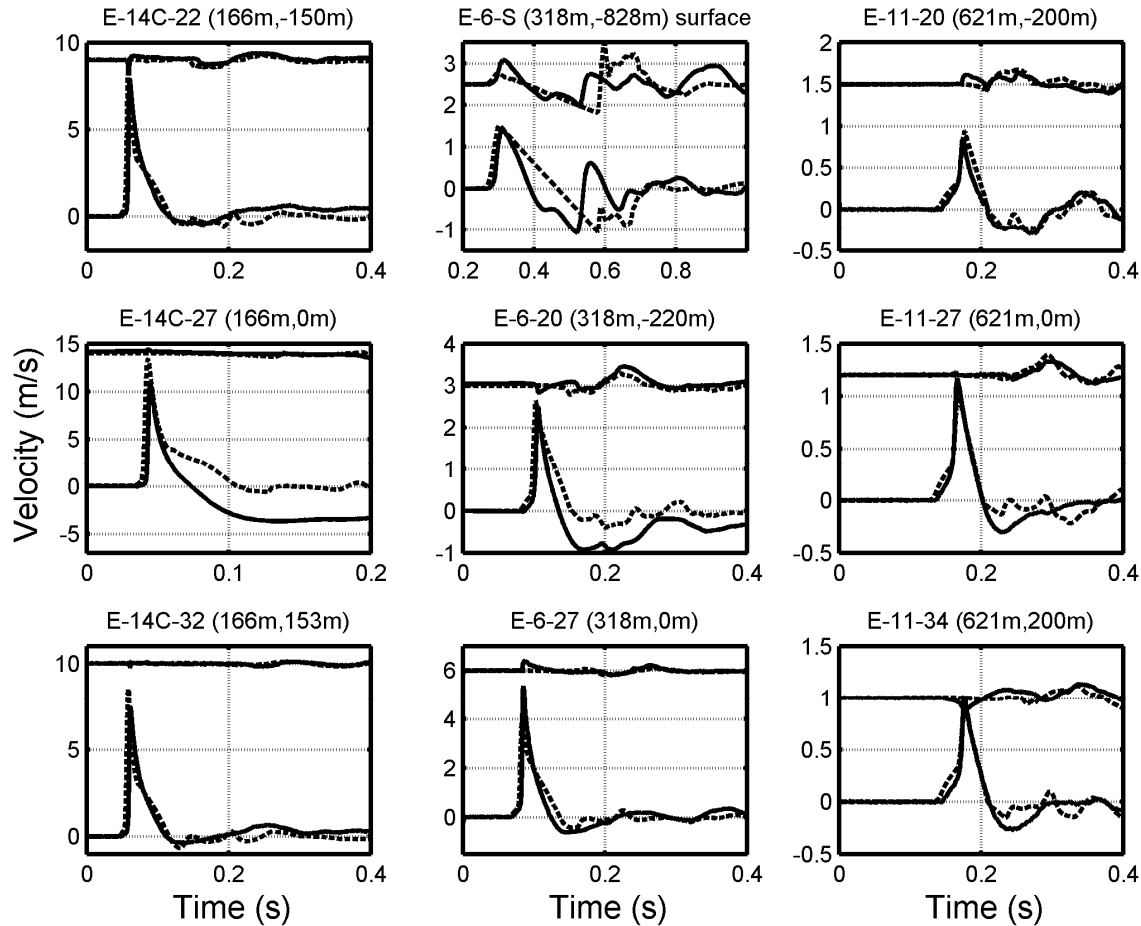


Figure 25. Comparison between the observations (solid lines) and numerical synthetics (dashed lines) at 9 stations. The top traces are tangential velocity and the bottom traces are radial velocity in each location. Note the good agreement between the observations and synthetics at the surface location and near the shot point. Spall at E-6-S is seen in both observations and simulations.

Comparison at receivers between the observations and simulations is shown in Figure 25. In each figure, the solid lines represent data and the dashed lines the synthetics, with upper traces indicating the tangential component (positive downward) and the bottom lines the radial component (positive away from the explosion source). The two-dimensional numerical results are in good agreement with the observations. All the inside locations have dominant radial components, although there are relatively small tangential waves at distance, demonstrating that the tamped Salmon explosion closely resembles a point spherical explosion source and any heterogeneities and layer boundaries convert little compressional wave energy into shear waves. The source level stations, E-14C-27 and E-6-27 show quite small amplitude shear waves relative to the compressional pulses, but E-11-27 has a larger shear wave amplitude. Its timing is consistent with P to S conversion at the salt-anhydrite interface and so it does not directly come from the explosion source.

The final cavity radius in two dimensions is about 22.5m (compared with 22.3m derived from residual displacements by Perret, 1968b, 22.15m in the spherical symmetric calculation reported by Rimer and Cherry, 1982), greater than the measured cavity radius just before the Sterling event (17m, presumably due to shrinkage).

The salt surrounding the explosion suffers high deformation and yielding due to the high pressure and energy transfer. The calculated nonlinear region is shown in Figure 26. It shows that the nonlinear yield region extends to nearly 1000m horizontally and downward (which is consistent with the spherical calculation by Rimer and Cherry 1982), but is capped by the anhydrite rock 400 m above the cavity. Denny and Goodman (1990) analyzed the elastic Salmon precursor velocities and believed that the Salmon event was nonlinear out to about 800m in salt, possibly due to work hardening. Our result is consistent with their estimate from free-field observations. The Salmon explosion simulation also predicts tensile cracking near the cavity and spalling near the free surface. The tensile cracks extend nearly spherically up to 200m into the salt. At the surface (E-6-S), spallation is seen in both observations and synthetics (Figure 25, top row, center). The observations show greater slopes in the two components but the general characteristics are consistent. The aspherical distributions of the yield and cracks shown in Figure 26 are likely to be responsible for the small tangential components in Figure 25. The tensile cracks due to spall near the surface extend to a depth of about 60m above the shot. By analyzing the surface records, Perret (1968b) obtained the maximum depth of spall to be about 77m. The good agreement between the observations and synthetics indicates that the salt material model derived in the one-dimensional spherical case is suitable for the two-dimensional calculations.

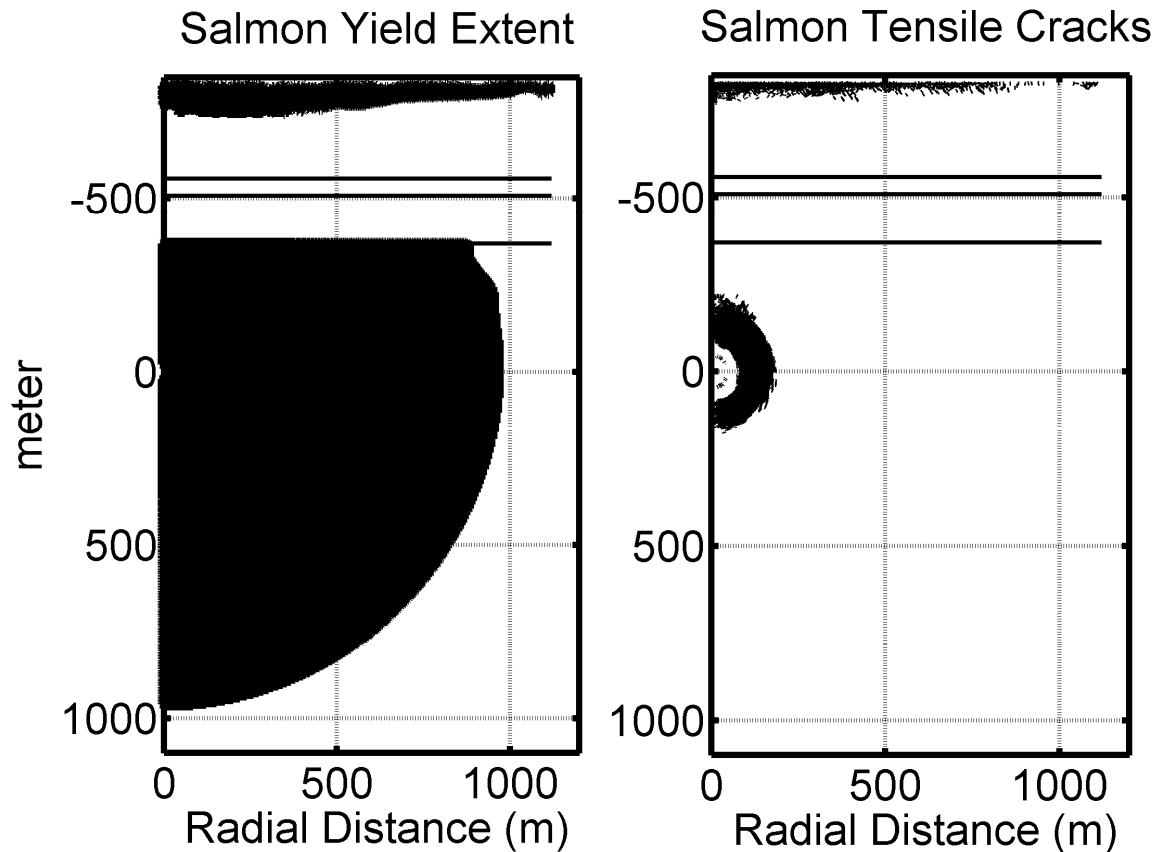


Figure 26. Nonlinear regions generated by the Salmon explosion. Left: yield region extending to 1000m; right: Regions of tensile cracking around the cavity and the free surface (spall).

5.4 Numerical simulation of the Sterling event

We model the Sterling event using the same finite difference code CRAM mentioned above, but coupled with the Eulerian code STELLAR to simulate the air-rock interaction. The grid setup is similar to that for the above Salmon event calculation. To successfully simulate waves due to the cavity explosion, the initial grid must be in equilibrium so that the motions due to the vacant cavity under overburden pressure are close to zero. The equilibrium solution is obtained by running CRAM in an overdamped mode with an initial approximate solution until motions become negligible throughout the CRAM computational grid. The early time interactions between the air shock due to an explosion and the surrounding salt interaction are simulated with STELLAR and then the stress states at 2.627 ms are overlaid onto the CRAM grid for calculating wave propagation at later times.

Figure 27 shows the STELLAR results at 2.6msec when the shock wave penetrates into salt. The particle velocity, pressure and plastic work distribution are all consistent with the non-spherical cavity geometry. Particles move in the radial direction above the cavity floor but in a complicated pattern below the floor. The pressure is higher below the cavity floor due to higher shock wave impact. The maximum pressure is 2.8kbar at 7m below the salt floor. The highest plastic work is found below the salt floor and indicates salt hardening. Figure 28 show the radial and tangential velocity data along with the numerical calculations. The velocity seismograms were compared at the same 7 receivers as were used in Langston (1983) plus at E6-20. Note that the station E14C-32 is misnamed as E14C-34 in Langston's article. Both observations and synthetics are lowpass filtered below 100Hz. The results show that the observed P wave amplitudes and pulse widths are predicted quite well by the finite difference method using the Rimer/Cherry salt model (Rimer and Cherry, 1982) at all 8 near cavity stations although our calculations show less complex P wave coda prior to SV arrivals than observed. Also, SV waves are well predicted at the shot level stations (middle 3 figures) and below (bottom 2 figures). Most striking is the comparison at the two deeper stations (bottom 2 plots) where the predicted polarity and amplitudes of the SV waves are in excellent agreement with the observations. The calculated SV coda is also less complex than observed. The calculated SV waves at the stations above shot level are smaller than observed, which could be due to some additional asymmetry in the shock arrival time on the upper cavity wall not modeled in the calculations. The good agreement between data and simulations implies that the shape of the cavity itself explains the observations. Also, the empirical salt model used in the calculation appears to be adequate to describe the salt's properties even at lower stress.

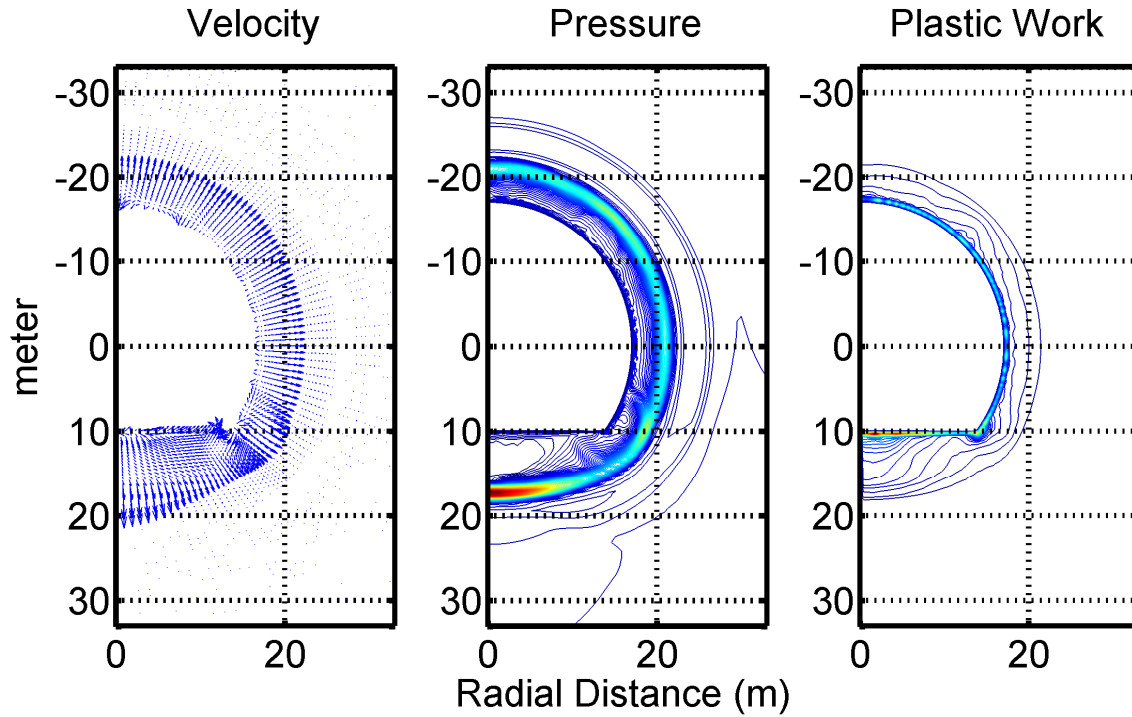


Figure 27. Interaction between the air shock and the salt calculated from STELLAR at 2.627msec. Left: particle velocity vectors. Middle: pressure contours. The maximum pressure is 2.8kbar at 7m below the salt floor. Right: plastic work distribution. The maximum plastic work incurred is about 5×10^6 ergs/cm³ at the pool floor, corresponding to the yield surface of 680bars. The higher plastic work indicates the higher yield surface (material hardening).

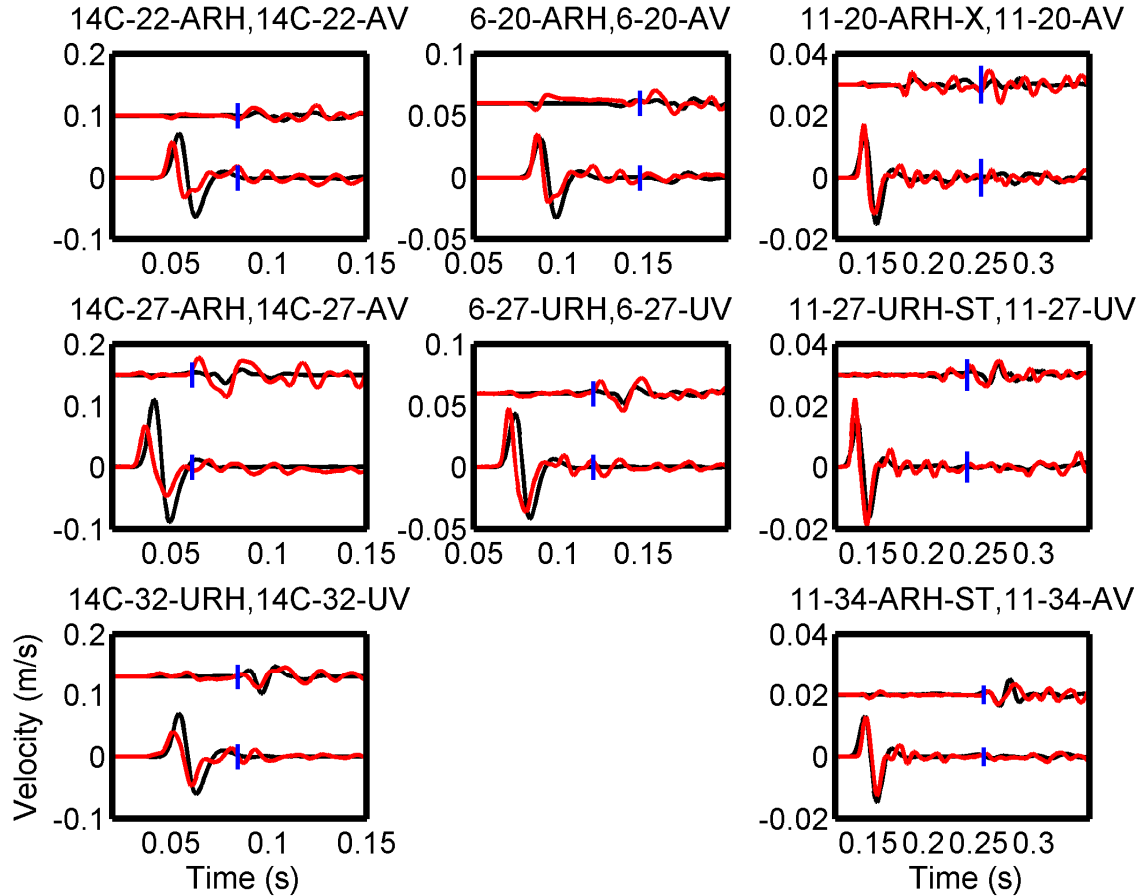


Figure 28. Observed (red) and synthetic (black) waveforms at near-cavity locations in salt. The top curve in each plot represents the tangential component and the bottom curve represents the radial component. The blue vertical bars denote the theoretical SV arrival time ($v_s=2550\text{m/s}$). The waveforms have been lowpass filtered below 100Hz. The agreement on P wave arrivals and amplitudes is striking, and the agreement on S wave arrivals and amplitudes is better for the shot-level locations and below than for above shot-level stations. The synthetics show less complexity than the observations.

The Sterling device is not fully decoupled in a 17m cavity according to the Latter (1961) criterion. The eventual nonlinear deformation extends into the surrounding salt (Denny and Goodman 1990). Figure 29 shows the nonlinear deformation (left) and tensile cracks (middle) from the Sterling calculation. Since Sterling is an overburied cavity explosion, the high overburden pressure limits the yield region to about 65m above and to the right of the cavity, and to less than 60m below. The Rimer/Cherry salt model hardens after accumulating plastic work, and so the region below the cavity, which experienced the highest shock pressure, also hardened the most, limiting the extent of the nonlinear zone below the cavity. This is likely to cause additional asymmetry in the outgoing waves, adding to SV generation.

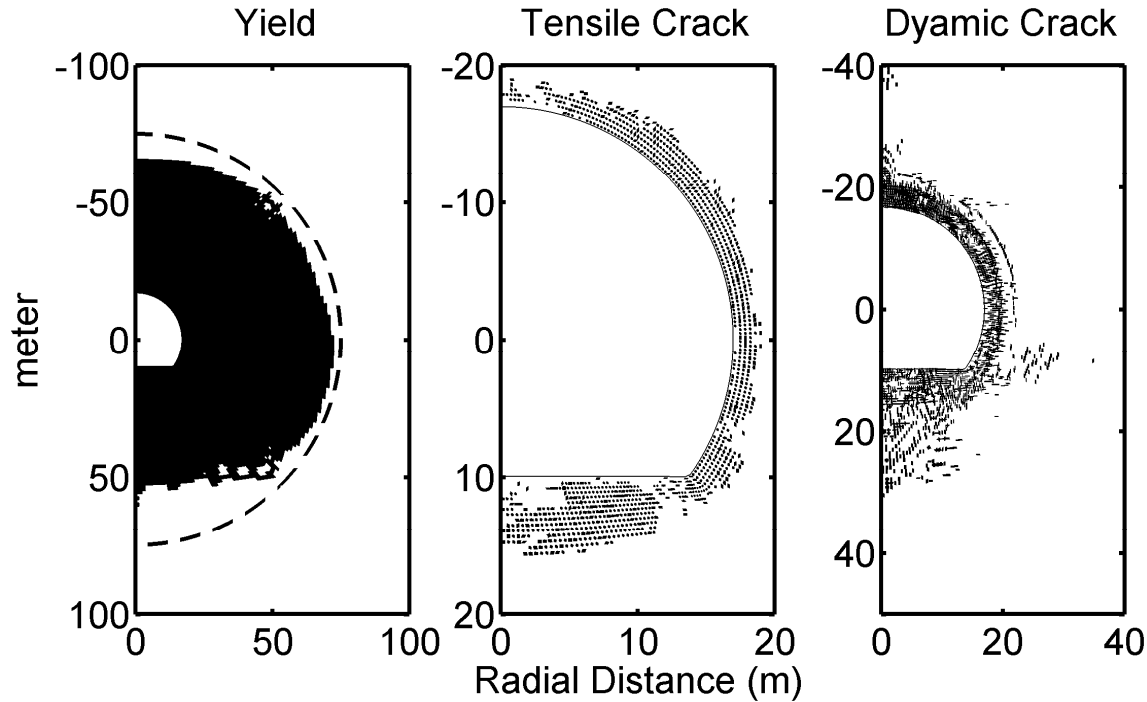


Figure 29. Left: nonlinear deformation distribution due to the Sterling explosion. The dashed line circle is drawn to highlight, by contrast, the asphericity of the yield region. Middle: tensile crack distribution due to the Sterling explosion. Tensile cracks open only near the cavity wall. No spall is observed in the calculation. Right: locations where dynamic fractures could occur.

We also performed two sets of tests to examine where hydrofractures could occur (see Nilson et al., 1991; Stevens et al., 2006a). The right panel of Figure 29 shows the fracture locations if the entire surrounding salt is pressurized by the cavity. This calculation depicts the preferred pathways for the possible fractures driven open by the cavity pressure. This plot shows that a vertical fracture near the axis of symmetry below the cavity floor is more likely to propagate due to higher shock impact than at other locations but its extension is limited to 20 meters into the salt. To test Langston's conjecture on the kinematic fault geometry, we also modeled a single preexisting conical crack connecting to the outer bottom edge of the cavity. The results indicate cavity pressure does not exceed the overburden pressure, and so a crack at that location would not be driven open. This calculation implies that the dynamic crack opening is not a contributor to the observed SV generation.

5.5 P and S spectra and waveforms from the Sterling event

The nonlinear source synthetics above reproduce the near-field initial P and S pulses quite well, in both polarity and amplitude. The observed P coda and S coda however, are not modeled well as they extend to a considerably longer time. The long-lasting complex coda could be caused by reverberation inside the cavity and in the nonlinear damage region. To further look into the explosion source characteristics, we align nearfield recordings at the initial P and initial S arrivals respectively, and examine the records for 0.05s after P, and 0.2s after S. The comparison between the seismograms from stations above, at and below the shot level should reveal the dependence of waves on the incidence angle. In the following all the records and

synthetics are scaled to a reference distance of 679m for comparison using constant $Q_p=200$ (Gupta and McLaughlin, 1989) and $Q_s=50$ for attenuation in salt and correcting for geometrical spreading. To estimate corner frequencies, an attenuation correction is made at the reference distance. Q_s is estimated by matching the seismograms at the same distance after correction. The receivers at E11-20, E6-20, E14-20 and E14C-22 (above the shot level), at E-11-27, E-6-27 and E-14-27 (at the shot level) and at E-11-34, E14C-32, E-14C-36 and E14C-39 (below the shot level) (Figure 24) are used (no data are available at station E5-27). An additional 10 stations above and below the shot level are used for numerical calculations.

Comparisons of P spectra and coda, specifically acceleration waveforms (top row) and their displacement spectra (bottom) are shown in Figure 30, for both the observations (left) and synthetics (right). In each waveform plot, the top, middle and bottom traces correspond to the receivers above, at and below the shot level, respectively. There is good general agreement between observations and synthetics in the time domain. That the amplitudes and shapes are consistent in general at the three levels indicates that the P waves originate from the cavity and no significant interference from upper layers is included, as these waveforms are all scaled to the same distance from the cavity center. Displacement spectra demonstrate that both observations and synthetics for P waves have a clear corner frequency around 30Hz and have a similar dropoff rate at higher frequencies (Figure 30, lower row). The corner frequency is consistent with that obtained by Sharpe's model (Denny and Goodman, 1990). The thick line represents the spectrum calculated using the reduced velocity potential from the decoupled 0.38kt explosion in a spherical cavity of 17m in radius. The two spectra are in good agreement, further confirming that the P waveforms are mainly from the cavity.

Similar comparisons for SV waves are depicted in Figure 31. Each waveform plot (at top) shows the scaled S waves and coda above, at and below the shot level for observations and synthetics. The synthetics are less complex than the observations, but the initial amplitudes are in good agreement. Note also that since the overlay from STELLAR to CRAM was performed after the primary shock wave had entered the surrounding media, but before any cavity reverberations had reached the boundary, motion from any later time reverberations is excluded from the calculations. The direct SV waves (prior to the thick vertical line) appear to have negative polarity above shot level and positive polarity at and below shot level, as described by Langston (1983) although they are more complex than that simple description. The SV coda in the observations (after the thick vertical line) are surprisingly coherent in amplitude and phase at all 11 stations after correcting for attenuation and geometrical spreading. The coda similarity between all the recordings at a variety of angles from the cavity source strongly suggests that much of the S coda comes from the localized source regime, not from scattering off lateral heterogeneities or layer boundaries (which would show time delays).

The displacement spectra of SV waves in the 0.2s window (including direct and coda SV) are shown in the bottom row of Figure 31. Again it shows consistency of the spectral characteristics at all the stations for the observations and synthetics. All the spectra have been corrected for attenuation. The synthetics have lower spectral amplitudes, as expected from the waveform plots (top). Both the observations and synthetics show SV waves with richer high frequency content than the P waves, i.e., the corner frequency is at 50-60Hz, higher than the 30Hz corner frequency of the P waves.

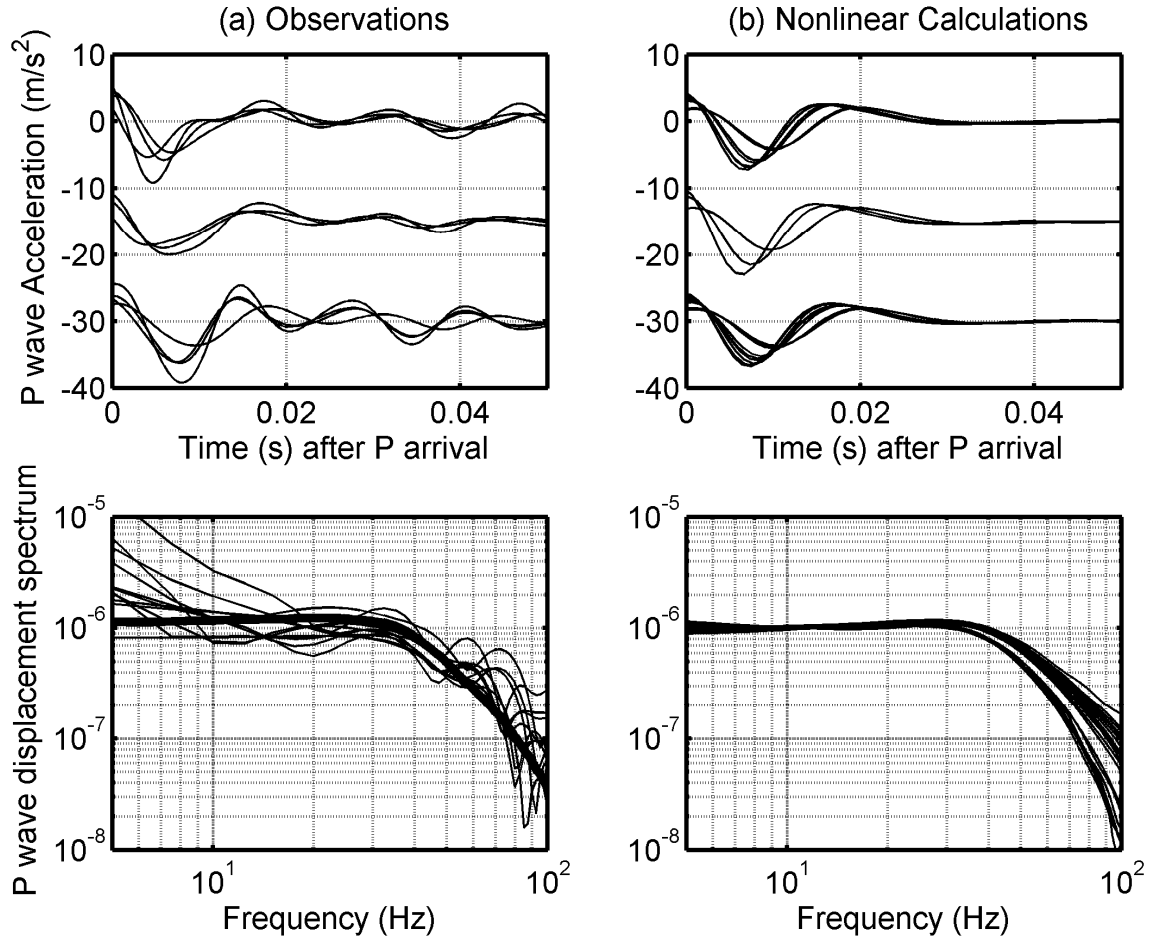


Figure 30. P waveforms (top) and spectra (bottom) from the observations (left column) and nonlinear calculations (right column). The radial P waveforms are aligned at their predicted arrival times given a velocity of 4.6 km/s, and filtered from 3 – 100 Hz. In each waveform plot the top, the top, middle and bottom sets of seismograms correspond to receivers above, at and below the shot level. In the observed P spectra (bottom left), the thick line indicates the prediction for a spherically symmetrical case. All the records are scaled to the most distant location by using $Q_p=200$ and corrected for geometrical spreading.

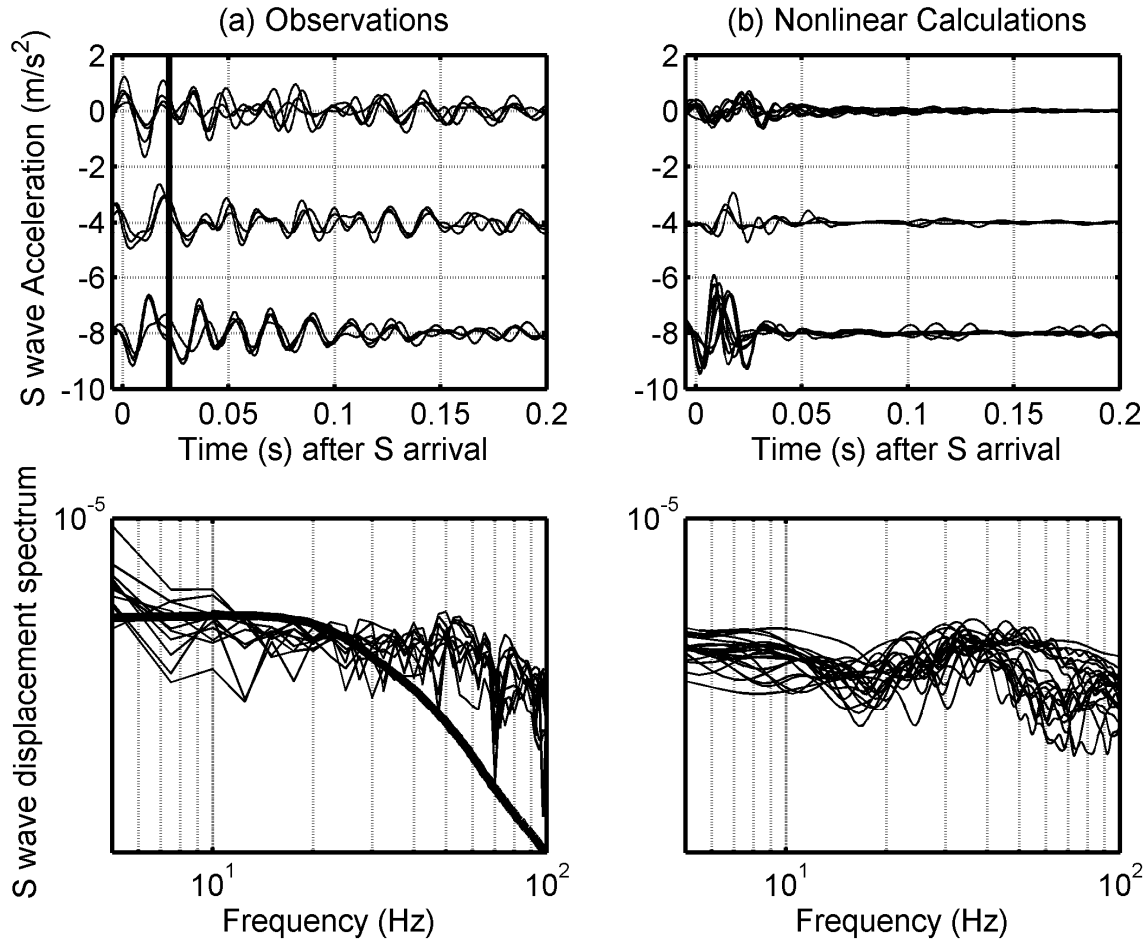


Figure 31. S waveforms (top) and SV spectra (bottom) obtained from the observations (left column) and nonlinear calculations (right column). SV acceleration waveforms (tangential components) are aligned at the predicted arrival times given a velocity of 2.55km/s, filtered from 3 – 100 Hz. In each waveform plot, the top, middle and bottom seismograms correspond to receivers above, at and below the shot level. In the observed S spectra (bottom left) superimposed is the predicted spectrum using the scaling relationship between P and S waves as discussed in the text. All the records are scaled to the most distant location by using $Q_s=50$ for S after geometrical spreading correction. Records at the same level or similar incidence have similar waveforms from the initial S throughout the coda, indicating that the bulk of the energy is coming directly from the source. Note that the corner frequency of the observed S waves is higher than that of the P waves in both the observations and the synthetics.

Fisk (2007) showed that for many explosions the S wave spectra are related to the P wave spectra by the velocity ratio: $U_s(\omega) \sim U_p(\omega\beta/\alpha)$, so the S wave corner frequency is less than the P corner by a factor of β/α . The thick curve on the left side of Figure 31 is the SV displacement spectrum scaled from the P spectrum by using the velocity ratio, and it is clearly inconsistent with the near field Sterling data. However, the velocity ratio scaling would be expected if the S waves were caused by a permanent asymmetric deformation, and in this case they appear to be caused by transient cavity reverberations. Stevens and Baker (2009) shows that reverberations from an offset source in a spherical cavity cause a dipole source that generate S

waves similar to those observed here. Figure 32 shows the P and S spectra calculated in that paper from a point explosion source offset from the cavity center with multiple reverberations, with the scale changed to have the same frequency range as Figure 31. The calculation was for an explosion modeled as a point pressure source offset from the center of a 17 meter radius cavity. The S-waves are caused by pressure reverberations which are strongest at the bottom and top of the cavity and decay over time. The results are similar to those in Figure 31. Although the S spectra goes to zero in the long period limit, the amplitude is comparable to P above 5 Hz, and the S spectrum has more high frequency energy than the P spectrum. The near field P and S waves from Sterling therefore appear to be explained quite well by the shape of the cavity which causes a variation in pressure amplitude and arrival time across the cavity, and cavity reverberations oriented vertically causing a secondary vertical dipole source.

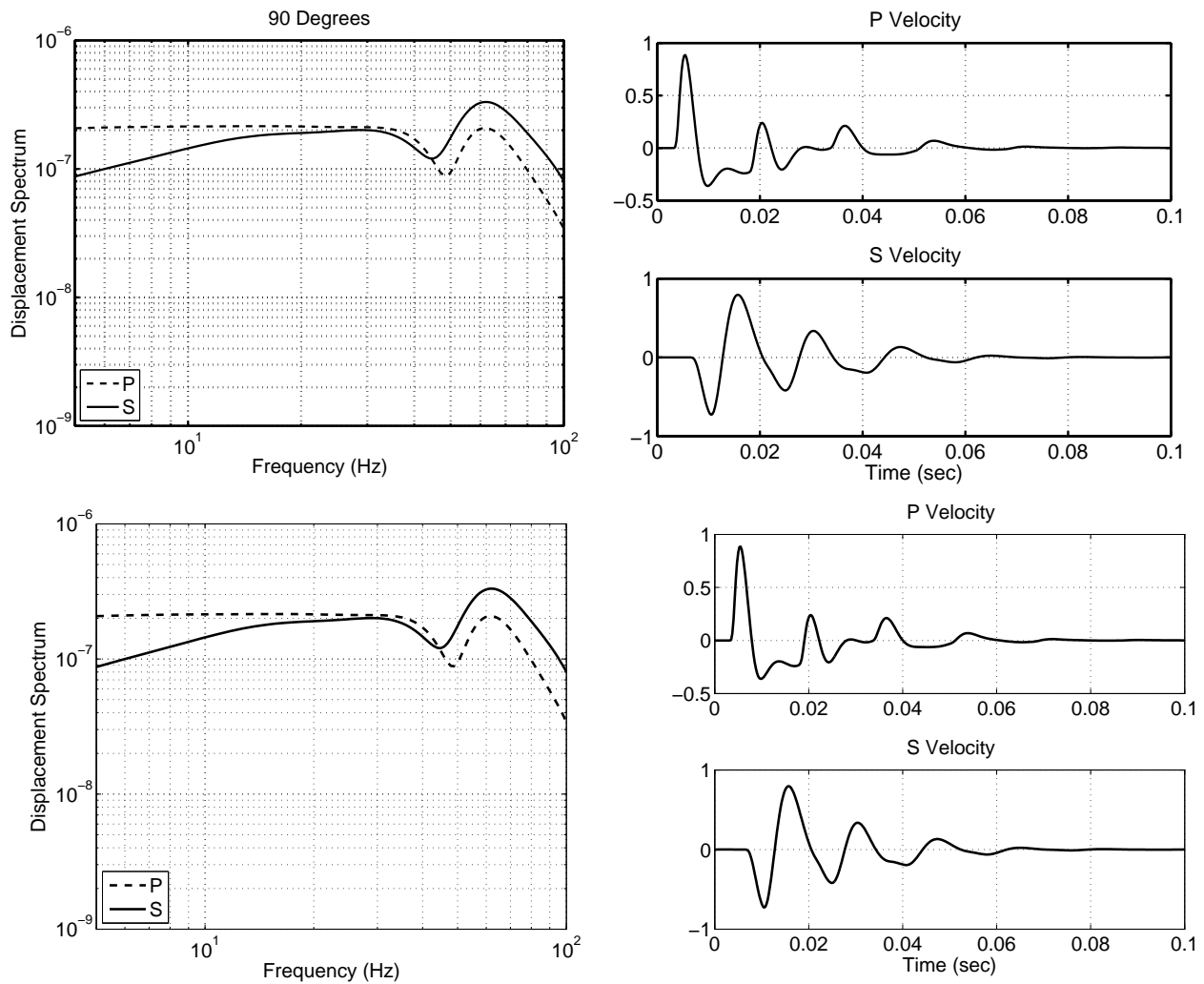


Figure 32. P and S spectra (left) and velocity waveforms (right) from a point explosion source offset from the center of a 17 meter cavity at 90 degrees from the offset direction.

5.6 Discussion and Conclusions

We have used the two-dimensional axisymmetric finite difference method to model the nonlinear wave propagation for the tamped Salmon and decoupled Sterling events. The numerical results provide insight into the shock wave interaction with salt and the nonlinear deformation due to the explosions. The numerical results are in good agreement with the observations in the near field for both events. As expected, Salmon records are dominated by the compressional wave pulse. The final cavity of the simulation is about 22.5m in radius, while Perret (1968) estimated the Salmon cavity radius from the measurement to be around 22.3m by using the simple incompressible salt model. The nonlinear deformation range extends to nearly 1000m which is consistent with that obtained by Denny and Goodman (1990) using other methods. The agreement indicates that the simple work-hardening salt constitutive model is adequate to describe the salt behavior at higher stresses. Using the same salt properties, the calculated seismograms in the near field are in good agreement with the Sterling observations. The nonlinear region is accordingly much smaller, i.e., about 60m, also consistent with that estimated by Denny and Goodman (1990) using the spectral ratios at distance. It is reported that Salmon did some damage to the surrounding salt up to 60m (Denny and Goodman, 1990), and for the Sterling event, the initial cavity radius is about 5m shorter than that estimated from the Salmon cavity because the cavity shrank after the Salmon event (Rawson et al., 1967), but the general agreement between synthetics and observations in the Sterling event implies that the effect on the salt material properties is insignificant.

Sterling records clearly show the shear wave generation due to the cavity asymmetry. For a non-isotropic explosion source, Zhao and Harkrider (1992) found that a point explosion offset from the center in a solid-filled spherical region embedded in a whole space acts primarily as a dipole source, which can generate S waves comparable in amplitude to the initial P wave. Stevens and Baker (2009) found a similar result for an offset explosion in an air-filled cavity and as discussed above, the offset explosion including cavity reverberations gives similar results to Sterling observations.

In the Sterling event, the calculations above show the aspherical cavity geometry is sufficient to generate the observed P and the major SV characteristics in phase and amplitude in the calculation, although the strong SV coda is not modeled due to the early time pressure overlay implementation. Our results demonstrate that the S waves originate directly from the source by shock wave conversion and reinforce Perret's (1968a) suggestion that the SV waves were generated from a fundamental asymmetry in shock pressure on the cavity walls caused by the pool of recrystallized salt at the floor. To fit the SV wave polarity, Langston (1983) explained the SV waves by a hybrid cone normal faulting model including both shear and tensile motion. Shear slip of only 70 microns is sufficient to reproduce the polarity of SV waves and amplitude. The dynamic fracturing calculation in this study using the pressurized salt model in Figure 29 (right plot) indicates the preferred fracturing orientation is downward, not in the normal faulting direction of 30 degrees from the horizontal beneath the cavity. Further, dynamic fracturing along the lower cavity corner is found to be blocked by the high overburden pressure and thus could not have generated the observed SV waves. Therefore, cavity asymmetry is our preferred explanation for the observed primary SV waves. Late arriving SV waves appear to be caused by vertically oriented cavity reverberations.

6. GENERATION OF SHEAR WAVES FROM EXPLOSIONS IN WATER-FILLED CAVITIES

Abstract: We analyze shear waves from a 27 kiloton nuclear explosion at 597 m depth in salt at Azgir, Kazakhstan, and four subsequent small nuclear explosions in the water-filled cavity of the original explosion. We use local recordings on a common set of radial and vertical component instruments to identify the source of these shear waves. These small explosions caused minimal damage to the cavity walls and so are similar in some important ways to cavity decoupled explosions, however the signal size is comparable to a tamped explosion. The shear wave amplitudes relative to P generated by the water-filled cavity explosions are comparable to each other and to the tamped explosion. Comparison of the water-filled cavity explosions' P-spectra, with a distinct bubble pulse peak, and two distinct S-phases, which lack that spectral peak, indicates that the S-phases are not scattered from P. The initial S-waves' travel time curve, impulsiveness, and compactness are consistent with generation at or very near the source and are inconsistent with significant scattering much outside the source volume. We estimate that the S waves are consistent with an S-wave source at the same depth and with the same moment as the spherical component of the explosion source. Nonlinear axisymmetric numerical modeling of the nonlinear deformation of the salt medium indicates that neither fracturing nor asphericity of the nonlinear region outside of the cavity, for variety of source asymmetries, would produce the observed shear waves for any of the water-filled cavity explosions. Oscillations of the cavity itself due to variations in the amplitude and timing of the pressure around the cavity wall can, however, produce shear waves at the frequencies observed. Both offset of the source and asphericity of the cavity lead to such variations in pressure.

6.1. Introduction

Understanding the generation of shear waves by explosions has practical value for nuclear monitoring and theoretical value to modeling of explosion sources. The ratio of S to P-wave energy is central to discrimination of explosions from earthquakes, so understanding the basis of the S-wave generation is necessary to appropriate application of the S-to-P discriminants. Decoupled explosions may be expected to produce fewer shear waves than would an otherwise similar tamped explosion, since decoupling should reduce the effectiveness of many of the usual mechanisms expected to dominate explosion shear wave generation, including asphericity of the source volume, spall, block motion, and tectonic release. In practice however, decoupled explosions often produce shear waves similar to those produced by tamped explosions in the same source location (e.g. Stevens et al, 2006a). Local recordings on a common set of radial and vertical component instruments of a tamped 27 Kt nuclear explosion at 597 m depth in salt at Azgir, Kazakhstan, and of four subsequent small nuclear explosions in the water-filled cavity of the original explosion provide an opportunity to investigate the generation of shear waves by explosions with many similarities to typical decoupled explosions.

That the cavity is water-filled makes this experiment unique. The water-filled cavity explosions are similar to decoupled explosions in air-filled cavities in that, in both types of explosions, much of the explosions' energy is expended in pressurizing the cavity, so nonlinear deformation outside the cavity is minimal. Our simulations of the explosions predict that the water would be vaporized to 0.8 meters for the 0.01 Kt explosion, the smallest one, with

nonlinear deformation outside of the cavity extending to three cavity radii. That is similar to the decoupling of the U.S. nuclear explosion Sterling (Xu et al, 2009). For the largest, 0.35 Kt, explosion, water would be vaporized to 2.6 m, with nonlinear deformation out to ten cavity radii. The cavity was examined between explosions and found to be largely intact, confirming a lack of significant nonlinear deformation. In each explosion, outside of the volume where the water is vaporized, the water is pressurized and a bubble pulse reverberation is modulated by the reflected shock wave (Murphy, et al, 2001). Unlike air-filled cavity explosions however, the water-filled cavity explosions generate large signals. Murphy et al. (2001) found that the explosions were not decoupled in terms of signal amplitude. Instead, the coupling was enhanced due to the greater pressure of water in the cavity than is the case for air filled cavities, which is largely due to the compressibility of air vs. the incompressibility of water. Thus, although the explosions are not decoupled in the usual sense, we can use their records to investigate shear wave generation by small explosions in approximately spherical cavities that cause little to no elastic deformation outside the cavity walls. In that sense, the findings will be relevant to decoupled explosions.

All of the explosions generated shear waves. The goal of the work reported here is to constrain to the extent possible the source of those S-waves. To this end we first analyze travel times and particle motions of local records and compare them with synthetics to unambiguously identify phases. We then compare spectra and travel times with predictions for different S-wave generation mechanisms. The distinct bubble pulse peak in the water-filled cavity explosions' P-spectra (Murphy et al, 2001) permits a test of whether the S-phases are scattered from P. Record sections using the closely spaced stations permit comparison of travel times and phase velocities with synthetics. The different S-P times for the tamped and water-filled cavity explosions are used to infer the depth of the S-wave source. Because these analyses indicate that direct generation at the source is the most likely cause of the observed shear waves, we use nonlinear source calculations to evaluate the effectiveness of possible mechanisms. Specifically we evaluate whether the water-filled cavity explosions could generate a sufficient aspherical component of nonlinear region to account for the observed shear waves. The calculations include offset sources and a nonspherical cavity that simulates the actual cavity geometry. We also perform nonlinear calculations to assess the potential of hydrofracturing or of opening of a pre-existing crack to generate the observed S-waves. We also perform simulations to assess the potential for oscillations of the cavity itself, due to amplitude and time variations of the pressure field around the cavity due to a source asymmetry, to generate the observed S-waves.

6.2 Data

These data provide the opportunity to compare seismograms of tamped and cavity (water-filled in this case) explosions from the identical source location and recorded at the same stations, which eliminates path effects. Murphy et al. (2001) report event dates and times (Table 2) and describe the following conditions. The source was located at 597 m depth, 47.9086 N. latitude, and 47.9119 E. longitude. The initial explosion left a cavity with a maximum horizontal radius of 32.5 m, and a volume equivalent to a 28.9 m radius sphere. The cavity changed only slightly with each explosion in the water-filled cavity, which was sealed before each explosion. After the 0.35 Kt explosion, its volume had increased 3%. After the 0.08 Kt explosion, both the floor and ceiling were approximately 3 m shallower, due to material falling to the floor from the roof.

Table 2: Azgir nuclear explosion dates and times.

Yield (kt)	Date	hh:mm:ss:ms
27	07/01/1968	04:02:00.5
0.35	04/25/1975	05:00:00
0.10	10/14/1977	06:59:59:10
0.01	10/30/1977	06:59:59:07
0.08	09/12/1978	04:59:58:49

Table 3 lists the distances of each station from the source. Recordings, nearly all just radial and vertical components, are available at each event-station pair marked with an x. Azimuths to the stations are unknown. Data were recorded at greater distances as well, but the closest recordings to the source provide more distinct arrivals and better resolution of high frequency spectra than do more distant local and near regional records.

Table 3: Available data from tamped (A2) and water-filled cavity explosions.

R (km)	A2 (27 kt)	A22 (.35 kt)	A23 (.10 kt)	A24 (.01 kt)	A25 (.08 kt)
0.59	-	-	-	-	x
0.82	-	-	-	-	x
1.1	-	-	-	-	x
1.17	x	x	x	x	-
1.6	-	-	-	-	x
1.71	x	x	x	x	-
1.96	-	-	x	-	x
2.8	-	x	-	-	-
2.88	-	-	-	x	-
3	-	-	-	-	x
3.06	x	-	-	-	-
4.64	-	-	-	-	x
7.8	x	x	x	x	-
8.8	-	-	x	x	x

Figure 33 shows velocity records at 7.8 km for the 0.01, 0.10 , and 0.35 Kt (from the top down) water-filled cavity explosions and the tamped explosion (bottom) filtered from 5 to 10 Hz. The vertical and the Hilbert transformed radial records are overlain to facilitate identification of the retrograde motion that often characterizes near source explosion shear waves. Although variations exist among all the records, each has a distinct secondary arrival at approximately 2 seconds after the initial arrival (which is set at 0.0 second, absolute times aren't known), the latter part of which shows retrograde motion and so indicates a likely shear wave of comparable amplitude to P for all four events.

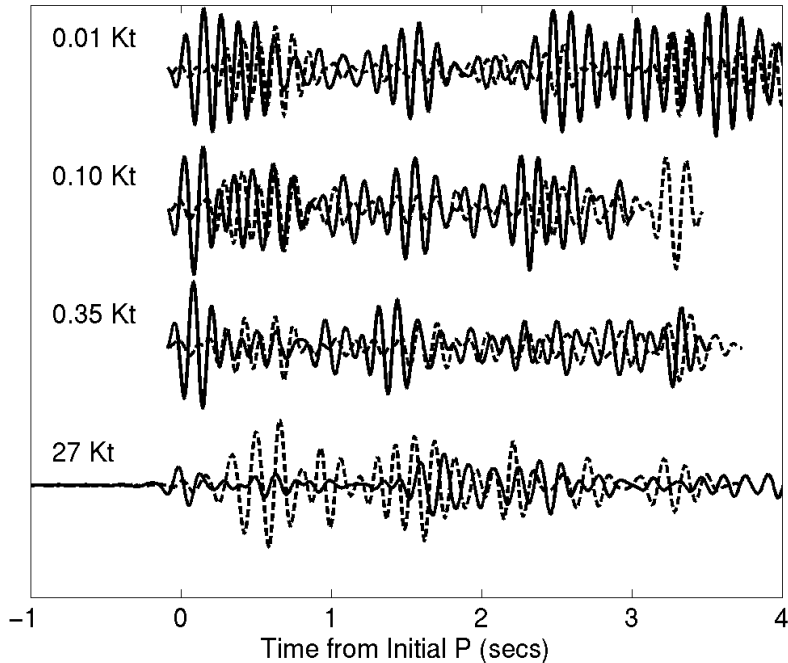


Figure 33. Vertical (solid) and Hilbert transformed radial (dashed) velocity records at 7.8 km, filtered from 5 -10 Hz, for three water-filled cavity explosions (upper three) plus the 27 Kt tamped explosion (bottom). Absolute times are not known, so traces are aligned with the first arrival set at 0.0 seconds. Alignment of the Hilbert transformed radial with the vertical identifies the local Sg phase as a higher mode Rg phase.

6.3 Identification of shear waves in the records

To compare P and S waves from the tamped vs. the water-filled cavity explosions, we first identify the phases. The S-waves are more prominent relative to P in the radial records, so we show radial record sections in Figure 34. These are records from all the water-filled cavity explosions, from 1 to 9 km distance. Recordings of different events are similar, so we use just one, or where possible a stack of several, at each distance. The upper record section shows the closest records with a dashed line indicating the start of a consistent later phase. We don't have absolute times, but if we assume a P-wave velocity of 4.25 km/s from the model of Murphy et al (2001), the relative moveout of the second phase near the source corresponds to a velocity of 2.05 km/sec, a reasonable corresponding S-wave velocity. At the more distant stations (lower record section), the secondary phase is more spread out. At those distances, the separation between the P and S phases is greater, allowing better isolation of the phases into reasonable length windows for spectral estimation.

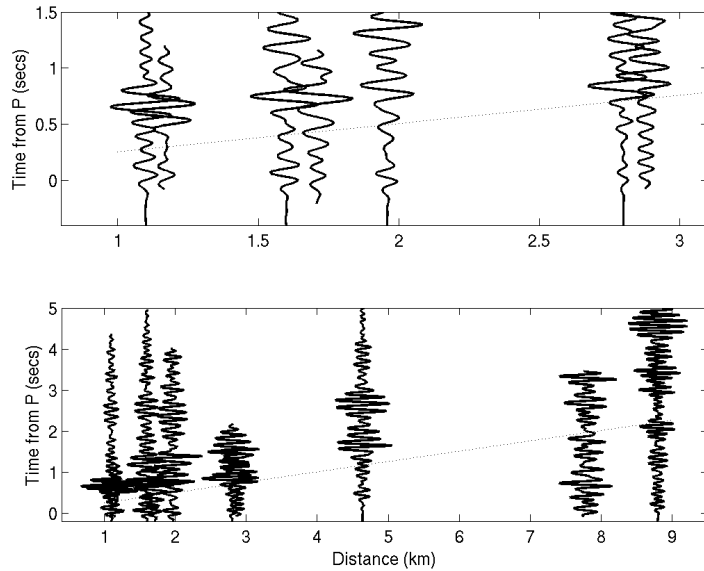


Figure 34. Record sections for the water-filled cavity explosions from 1 to 3 km (top), and from 1 to 9 km (bottom). Dashed lines show the 2.05 km/s group velocity (assuming a P-velocity of 4.25 km/sec) corresponding to the S arrivals.

We commonly observe retrograde elliptical particle motion in Sg near explosions (e.g. Stevens et al., 2007), which identifies the phase as higher mode Rg. The motion is more complicated for the very close-in records (Figure 35), but the particle motion still is useful in identifying the phases. The observed moveout of the second phase in the record sections above, identified as S, predict an S-P time at 1.7 km of 0.43 seconds. We plot the particle motion for the traces up to that time, and after that time, for the 0.01 Kt explosion (vertical records of the 0.35 Kt explosion are cut off too early, and the tamped explosion is dominated by lower frequency). The motion is linearly polarized motion throughout P, and becomes more circular at the S-P time, supporting identification of the second phase as S.

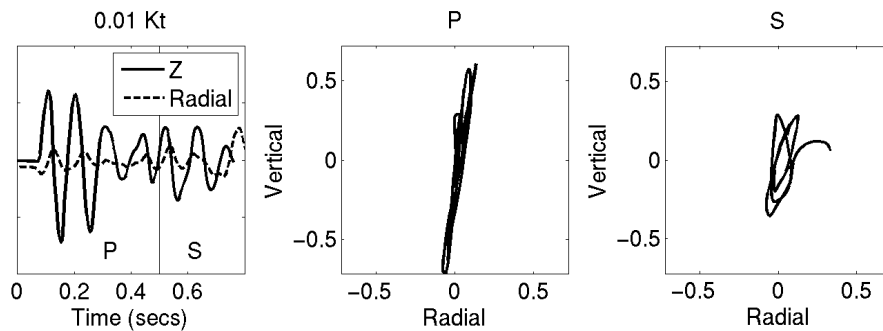


Figure 35. Overlain Hilbert transformed radial (dashed) and vertical (solid) velocity records at 1.71 km of the 0.01 Kt explosion (left) and particle motion up to the S-P time (middle) and after the S-P time (right).

Figure 36 shows the radial and vertical records from AZ22, the 0.35 Kt explosion, at 7.8 km, filtered from 5 to 10 Hz, where the signal to noise ratio is highest, compared with a point CLVD and explosion full waveform synthetic seismograms for the structure listed in Table 4. The shallow structure is described in Murphy et al (2001), and is overlain on a more general regional

structure model. Data are positioned so the initial arrivals align with synthetics, as absolute times are not known. The S wave in the CLVD synthetics at approximately 3.3 seconds matches the arrival in the data.

There is a late arriving P-wave at about 3 seconds in both the data and synthetics. It is much clearer in the data on the vertical component. To minimize the contribution of P-wave energy such as the phase at 3 seconds, and its coda, to the S spectra estimate, we use the radial components for spectral estimates.

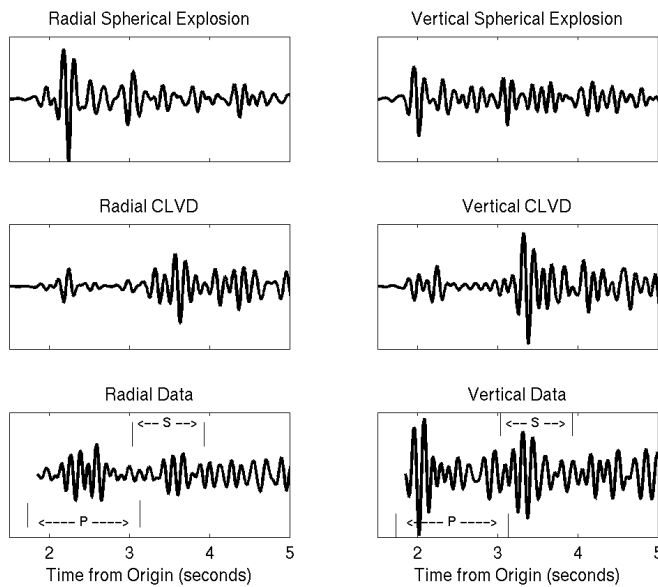


Figure 37: Radial (left) and vertical (right) spherical explosion (top) and CLVD (center) synthetics and data from the 0.35 Kt explosion (bottom) at 7.8 km. Vertical bars in the real data plots indicate the limits of the P (near the base of the plot) and S (near the top, approximately 3 to 4 seconds) windows used to estimate spectra. The explosion synthetic represents the response of the structure to a spherically symmetric source, and the CLVD is the first approximation to the non-spherical components of the source.

Table 4: Velocity model. The second layer represents an anhydrite cap on a massive salt dome.

Thickness (km)	Vp (km/s)	Vs (km/s)	Density (g/cm ³)	Q
0.240 1.	50	0.60	2.00	25
0.06 5.	65	3.15	2.77	200
5.000 4.	24	2.40	2.2	150
2.0 5.	2	2.95	2.30	500
2.0 5	.889	3.306	2.549	176
19.97 5	.935	3.332	2.566	195
10.00 6	.284	3.527	2.693	207
12.00 8	.357	4.691	3.449	231
115.00 7	.980	4.479	3.312	237

We also identify a second S arrival. It is much slower moving, arriving at approximately 4.2 seconds. Figure 37 shows overlain vertical and Hilbert transformed radial velocity records for the 0.01 Kt explosion at 7.8 km. The initial S arrival, identified earlier, is labeled S1. The second arrival, labeled S2, has retrograde motion consistent with higher mode

Rg. The records shown are filtered from 5 to 10 Hz, but the retrograde motion is clear even for records filtered from 8 to 12 Hz, indicating that the arrival is not likely fundamental mode Rg from the 597 m deep source, since for a velocity of 1.8 km/sec (based on the arrival time relative to P) at 10 Hz the source depth is three times the wavelength, which is too deep to generate strong fundamental mode Rg. The arrival is also too early for fundamental mode Rg in this velocity structure. The CLVD synthetics (Figure 36) also show more energy than the explosion synthetics after the initial S window, although the relative amplitudes don't match well.

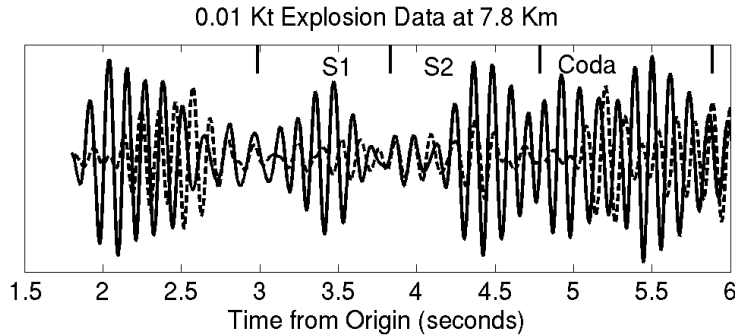


Figure 37: Overlain vertical (solid) and Hilbert transformed radial velocity records of the 0.01 Kt explosion at 7.8 km, filtered from 5 to 10 Hz. The first and second S arrivals (labeled S1 and S2) and the coda are delimited by vertical bars along the upper plot boundary.

Comparison of pre-event noise levels with signal is the usual method of ensuring that we are analyzing signal, not noise. The rms signal-to-noise ratios of all components and events recorded at the 7.8 km station range from ~80 to 1,800, but the pre-event windows are so short, most are smaller than 0.1 seconds, that there is not a measure of the signal-to-noise at longer periods. Only a few records have longer pre-event noise windows. One record of the 0.35 Kt explosion at 2.8 km has 0.5 seconds of pre-event noise. For that, the signal-to-noise ratio was more than 100 from the minimum frequency of ~2 Hz upwards. For records without sufficient pre-event noise windows, we use particle motion to assess whether a particular phase is well recorded relative to the background noise. That is, linear polarization in the expected P wave window indicates that the P-wave signal dominates that time window. Similarly, we have had success identifying shear waves near explosions by their retrograde particle motion, which is typical for higher mode Rayleigh waves. Thus, retrograde motion in the predicted S-wave window supports the assumption that the signal-to-noise level is sufficient. The lower and upper limits vary somewhat with the event and station, but the P-wave particle motion is generally linear from 1 to 15 Hz. The initial S-wave particle motion is typically retrograde down to at least 2 or 3 Hz, and sometimes to 1 Hz. Even then, the cessation of retrograde particle motion doesn't necessarily mean that the signal is down at the noise level, as lack of retrograde motion may be due to overlap with P at lower frequencies. The later S-wave is retrograde to 1 Hz, although at that frequency we may be observing the fundamental mode arriving within the same time window. Retrograde motion is not necessarily predicted for S, especially at higher frequencies, but even so it is commonly observed to 10 Hz. Thus we are confident that the records analyzed provide P and S signals at amplitudes well above the noise levels from approximately 1 to 15 Hz, with the most consistently strong signals from 5 to 10 Hz.

There is one local tangential component record, at 4.64 km. While the lack of additional tangential records limit nearly all our observations to the SV plane (and the lack of knowledge of station azimuths prevents detection of any radiation pattern), and so limits our modeling to

axisymmetry, this one tangential record provides a glimpse at whether the assumption of axisymmetry is valid or violated. We discuss this record in the modeling section, as it has some bearing on the source of the observed shear waves.

6.4 Origin and Characteristics of the spectral peak

Murphy et al (2001) showed that peaks in the water-filled cavity explosions' spectra could be explained by bubble pulse resonances near 8 to 10 Hz. These bubble pulses are higher frequency than those associated with underwater explosions, due to the constraints of the cavity. Specifically, the expansion of the bubble pulse is checked by the reflected shock wave. Murphy et al (1998) performed nonlinear calculations that included the material models, the water equation of state, and dynamic interaction of the shock wave, bubble pulse, and cavity walls. Calculations predict that, for the 0.01 Kt explosion for example, water was vaporized to a radius of 0.8 m, and its initial bubble extended to 6.2 m before the reflected shock wave stopped its expansion.

The observed bubble pulse is consistently near 9 Hz, although calculations predicted somewhat higher frequency overall, and an increase in frequency with yield (Murphy et al, 2001). The consistency of the peak suggests some controlling effect of the cavity itself. We also note that the prominence of the peak is greatest for the smallest explosion. For the largest, the peak only stands out clearly in some of the records. Figure 38 shows the stacked spectra of the best local records for each explosion (6 to 8 records per stack). The spectral peak is barely visible in the stack of the 0.35 Kt explosion, although it does stand out distinctly in some individual records. This is consistent with observations of Murphy et al (2001), for example their Figure 3, which show the spectra from the station at 1.71 km.

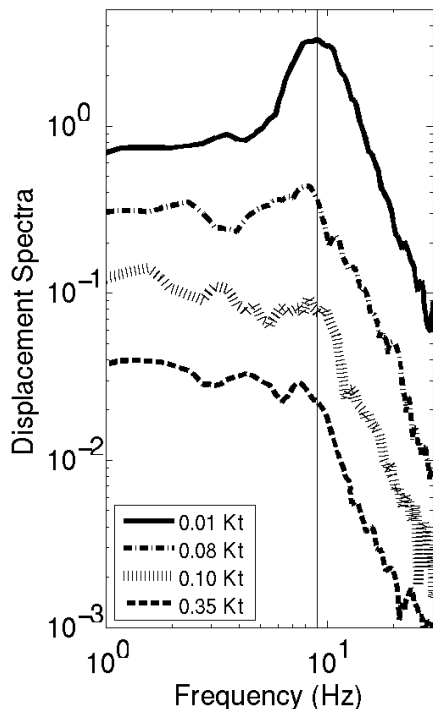


Figure 38: Stacked radial and vertical spectra for each of events.

6.5 The spectral peak distinguishes whether S is scattered from P

If the shear waves were dominated by scattered P-waves, their spectra should be similar to the P-wave spectra and should have the same resonance peak. The converse is not necessarily true. That is, a bubble pulse peak in the S spectra could result from periodic forcing of the cavity by the bubble pulse in an asymmetric fashion. Figure 40 shows spectra estimated from the radial components for the P (solid) and the initial S1 wave (dashed) arrivals. We use the records from 7.8 km because they recorded the tamped as well as three of the water-filled cavity explosions, and because the separation of S and P is insufficient on closer-in records. We use the radial records, where P amplitudes are lower. This is important because of the apparent overlap of secondary P-arrivals and of P-coda with the S-arrivals. Windows are as shown in Figure 37. The P window is from 0.2 seconds before the initial arrival to 1.2 seconds after. S runs from 1.1 seconds after initial P, to 2.5 seconds after. The amplitude is small over the 0.1 second overlapping section between the two phases, and is further diminished by Hanning tapers applied before spectral estimation.

Each of the water-filled cavity explosions has a peak in the P spectra at approximately 9 Hz (vertical line) associated with the bubble pulse modeled by Murphy et al. (2001). A corresponding peak is absent from each water-filled cavity event's S spectra, indicating that the S waves were not generated by scattering from P. The tamped explosion (upper left) lacks the bubble pulse, confirming that the peak is not simply a propagation effect. Figure 41 shows the P and S2 spectra. Again, the water-filled cavity explosions' P, but not S, spectra show the bubble pulse.

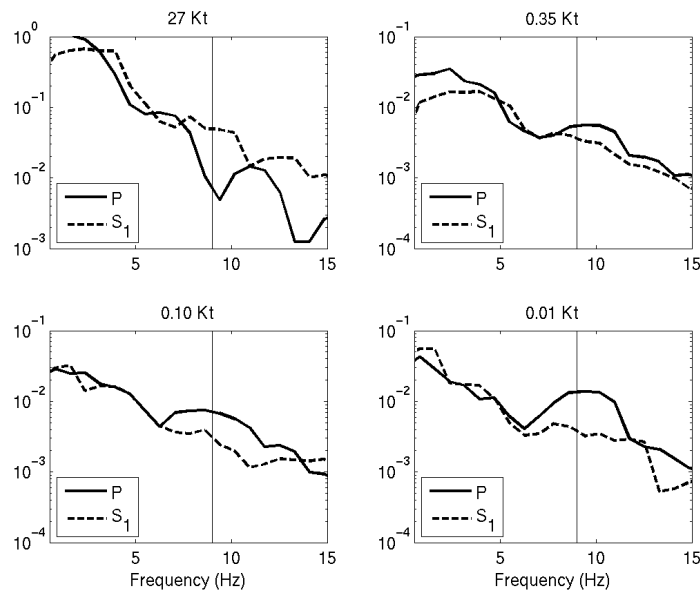


Figure 40. P (solid) and S (dashed) radial component spectra of the tamped (upper left) and three water-filled cavity explosions, using the first S arrival. Murphy et al (2001) identified the 9 Hz P spectral peak as associated with a bubble pulse in the water-filled explosions. The peak does not exist for the initial S wave.

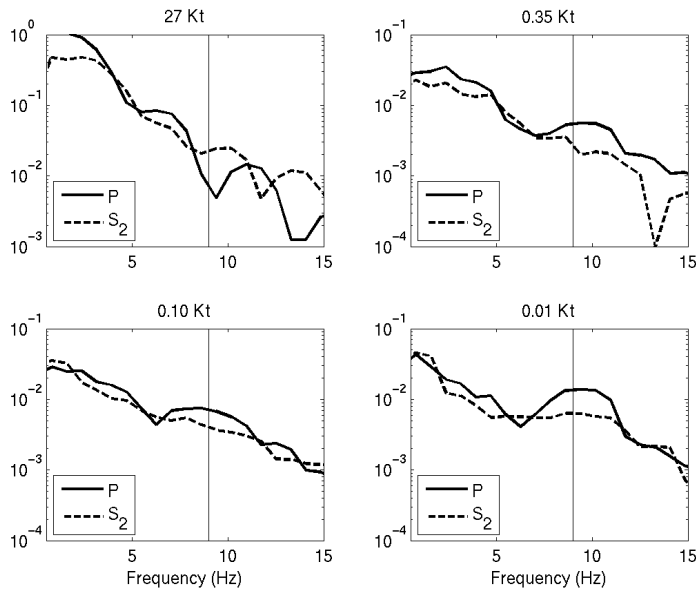


Figure 40. Same as Figure 39, but for the second S arrival.

It is possible that the spectral peak has been attenuated from the S-wave, or obscured by the scattering process. We check that possibility by examining the coda spectra. The 0.01 Kt explosion is the only one with a sufficiently long radial record at 7.8 km to include the coda. The other events' records are cut off too early. Figure 41 shows the P and coda spectra for those two events. The water-filled cavity explosions' spectra are again estimated from the radial component. The tamped explosion spectra are estimated from the vertical component, because the radial component is cut off too early. Unlike the case for the S arrivals, the spectrum of the water-filled cavity explosions' coda shares the P-wave bubble pulse peak, indicating that the coda was scattered from P. This shows that for scattered energy arriving even later than the S phases the bubble pulse peak was not obscured by attenuation or by the scattering process. Thus, the peak should have been apparent in the S-spectra if the S were scattered from P. Again, both the P and coda spectra of the tamped explosion lack the bubble pulse peak.

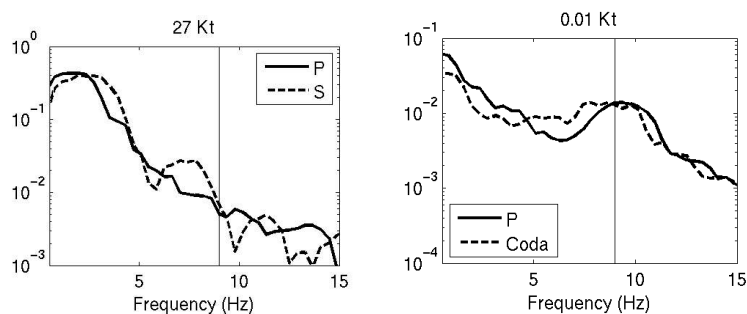


Figure 41. P (solid) and coda (dashed) spectra of the tamped (left) and 0.01 Kt water-filled cavity (right) explosions using the coda window of Figure 37.

6.6 Initial S travel time curve is consistent with source generation

We examine the S-P times to see if they are consistent with a source of S at the same location and time as P. Event AZ25, the 0.08 Kt explosion, was recorded at 6 stations, at 0.82 to 4.6 km from the source. Figure 42 shows the data (left) and CLVD synthetic (right) record sections for

displacement. Figure 43 shows the picked S minus P times versus distance for both. The data S-P times are very similar, just slightly delayed, to those of the CLVD synthetics (spherical explosion synthetics do not reproduce the S-phase). Consistent S-P times for data and synthetics provide evidence, independent from the spectral observations, that the shear waves are either generated at the source or scattered from very near the source.

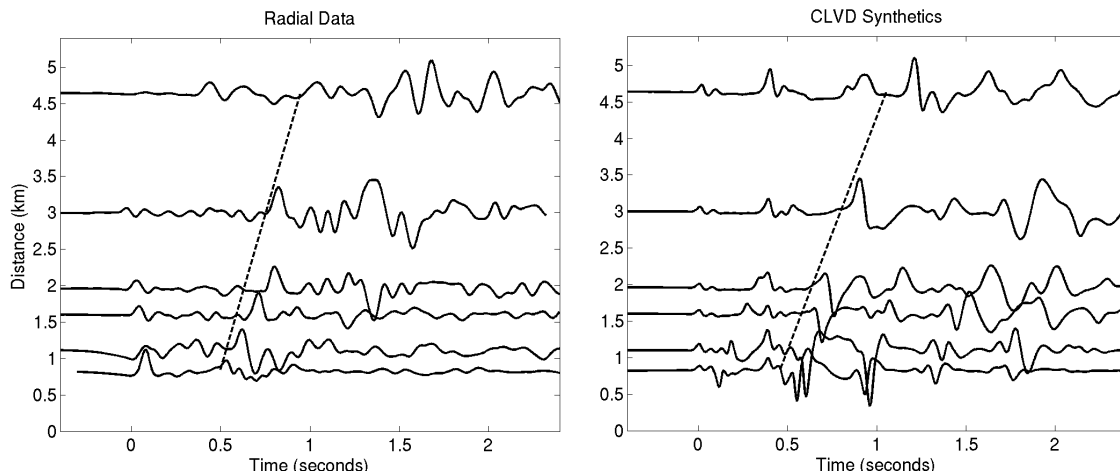


Figure 42. Radial seismograms from event AZ25 (left) and CLVD synthetics (right). Seismograms are aligned on initial P. Dashed lines precede the S arrivals.

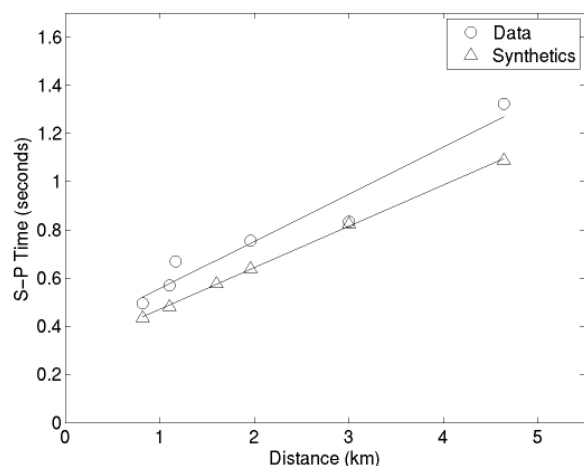


Figure 43. S-P arrival times from event AZ25 (circles) and CLVD synthetics (triangles). Lines are fits to S-P times vs. distance.

6.7 Size and depth of the explosion S-wave source

Our goal in this section is to estimate the size and depth of the S-wave source relative to the P-wave source. We use a CLVD and a monopole for this effort. The CLVD, the next higher moment spherical harmonic after the monopole, is a practical and common choice for modeling of explosion shear waves. In later sections, we will address whether we can refine our understanding of the actual S-wave source. We use the records at 7.8 km, because that station recorded the tamped and three of the water-filled cavity explosions, and the P and S phases are better separated than in the very close in records. We match the average of the vertical and radial component amplitudes, and for S, match the sum of the first and second S phase

amplitudes. To first order, a CLVD with the same moment as the explosion provides a good match to the observed S-to-P ratio of each of the explosions. There is some variability between even the water-filled cavity explosion S-to-P ratios, so it is difficult to draw conclusions regarding second order differences between the water-filled cavity and tamped explosions. Nonetheless, some of the details are interesting. When filtered from 5 to 10 Hz, the CLVD component required to match the observed water-filled cavity explosion S-to-P ratios is significantly smaller than that of the tamped explosion, 41% of the total moment vs. 65%. When filtered from 4 to 8 Hz however, so the bubble pulse peak is excluded, the tamped explosion's CLVD moment relative to the spherical explosion moment is only slightly larger than the water-filled cavity explosions'. Specifically, the CLVD then is, on average, 53% of the total moment of the water-filled cavity explosions, vs. 61% for the tamped.

Another important observation is that the initial S-wave of the tamped explosion is later than that of the water-filled cavity explosions, which suggests a shallower shear wave source for the tamped explosion relative to the water-filled cavity explosions. We will compare synthetics for CLVD sources at different depths, but the CLVD is an idealized point source. To investigate the distribution of the tamped explosion source volume and its effect on the waveforms we also perform a nonlinear source calculation. Figure 44 shows the nonlinear yield region and location of tensile cracks predicted for the 27 Kt explosion by a 2D, axisymmetric, nonlinear, Lagrangian, finite difference code named CRAM (Stevens et al, 1991c). The nonlinear deformation area extends from approximately 2 km depth to the surface, and the cracks extend horizontally to 2 km at the surface.

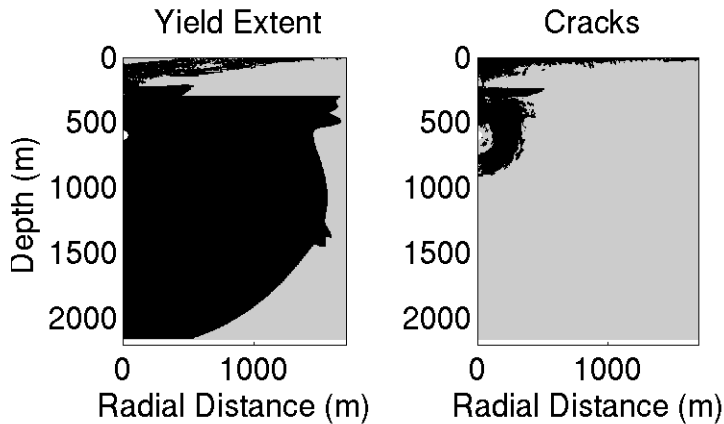


Figure 44. Nonlinear yield region of the 27 Kt tamped explosion (left), and tensile cracks (right).

Figure 45 compares three different synthetics with the tamped and a water-filled cavity explosion seismogram. The two uppermost traces show the sum of synthetics for a 597 m depth spherical explosion plus a CLVD of the same amplitude. The upper trace shows the case where the CLVD is at the same depth. The second trace shows the case where the CLVD is at half the depth. The S-wave energy is more strongly concentrated later in the seismogram in the second case due to greater excitation of shallower, slower modes. The middle trace shows seismograms from the nonlinear calculation of Figure 44, which also has S-wave energy arriving later than it does for the deep CLVD source. To produce those records, the time dependent displacements and stresses computed by CRAM are saved on a cylindrical monitoring surface located outside of the region of nonlinear response. These provide the input to wavenumber integration calculations that propagate them to local and regional distances. The large early S arrival from

the deeper CLVD source (top trace) matches the earlier S of the 0.35 Kt event (fourth trace). All the water-filled cavity explosions have similar, earlier S. The concentration of energy later in the S-wave window of the tamped explosion (bottom trace) is more similar to the seismograms from the shallower CLVD source (second trace) and the nonlinear calculation (middle trace). (This is less clear in the radial component (Figure 33) which has some additional motion apparently caused by the source extending into the shallow layer).

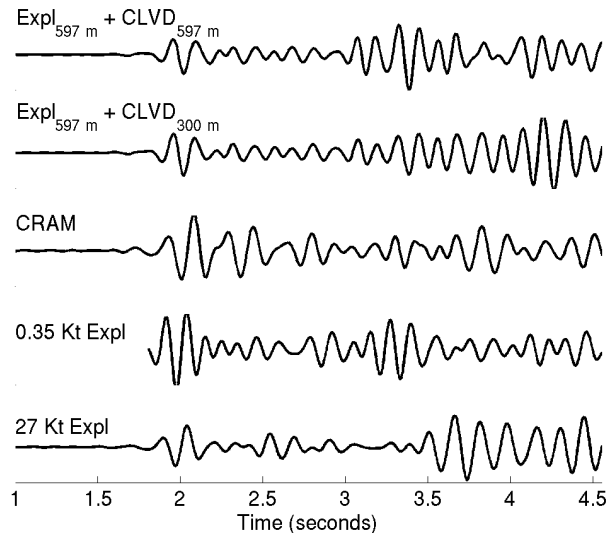


Figure 45. Synthetic vertical seismograms at 7.8 km, filtered from 5 to 10 Hz for an explosion plus a CLVD source of the same moment at the same depth (top), and an explosion plus CLVD source of the same moment but at half the depth (second trace), and for the source determined from the nonlinear source calculation (Figure 44). The deeper CLVD source matches the earlier S of the 0.35 Kt event (third trace), while the seismograms for the shallower CLVD and the nonlinear source are consistent with the later S energy in the tamped explosion record (bottom).

Besides the effect on timing, a shallower source of the same moment yields larger amplitudes than a deeper source due to greater excitation of the shallow modes. This means that the moment of a shallow CLVD source necessary to match the observed S-to-P ratio of the tamped explosion is reduced. Resolution of the predicted amplitudes is limited by uncertainty in the details of the source structure and in the exact depth distribution of the tamped source. To first order however, we conclude that both the water-filled cavity and tamped explosion records require an S-wave source of comparable moment to the P-wave source to produce the observed S waves. The significant difference is that for the water-filled cavity explosions the source is at the spherical explosion depth, and for the tamped explosion, a much more distributed S-wave source that can be modeled by a CLVD at half the spherical explosion depth provides a better match to the data. Notably, the S-to-P ratio produced by the nonlinear calculations is smaller than that observed. Greater source asphericity may be required than is produced by the 2D calculation. Alternately, more complex structure than homogeneous salt in the vicinity of the source could produce larger S-wave amplitudes.

6.8 Shear Wave Source Modeling

6.8.1 Introduction

Models of the S-wave generation mechanism must be constrained to generating S at or very near the cavity for consistency with the uniform move-out of S minus P times for single events and with the differences between the tamped vs. water-filled explosion S minus P times, the latter already modeled by the depth of a CLVD. In the previous section we used a CLVD as the S-wave source. The CLVD is a common approximation to the aspherical component of the nonlinear deformation about the explosion source. We begin our modeling by using nonlinear axisymmetric source calculations to assess whether the water-filled cavity explosions could produce a sufficiently large aspherical component of nonlinear deformation to generate the S-wave amplitudes observed. To consider the maximum extent of asphericity likely in the nonlinearly deformed volume, we do these calculations for offset as well as centered sources. We do the calculations for the largest and the smallest of the water-filled cavity explosions. The actual cavity of the explosion is elliptical, and likely has a flat floor, so we also perform nonlinear source calculations for such a cavity. Besides increasing the asphericity of the nonlinear volume, which the offset source and asymmetrical cavity numerical calculations are intended to model, source asymmetries cause variations in amplitude and timing of the shock wave about the cavity wall which can generate shear waves. To predict the S-wave spectra relative to P due to amplitude and timing pressure variations, we use an analytic calculation of an offset source in a spherical cavity. Such a source is equivalent to movement of the cavity up and down (for a vertical offset). To compare the fit of such a source to the data relative to the fit of a CLVD source, we also calculate vertical point force synthetics. For comparison with the one tangential record, we use synthetics for a horizontal point force. We also numerically model both hydrofracturing and opening of a pre-existing crack for the largest water-filled cavity explosion to evaluate whether such cracking could generate the S-waves observed.

6.8.2 Nonlinear Modeling of Source Asymmetries

The first step of all of the nonlinear source models is a calculation similar to Murphy et al.'s (2001), which models the explosion in water, the expansion and contraction of the bubble pulse, its modulation by the reflection of the shock wave from the cavity wall, and nonlinear deformation outside of the cavity walls. We perform these initial calculations for a number of conditions, including yields of 0.01 and 0.35 Kt, offset of the explosion to the top and bottom of the cavity, and spherical and elliptical cavity shapes, the latter also having a flat floor.

The evolution of the shock is simulated in 2 dimensions (axisymmetric) with an Eulerian hydrodynamic code, STELLAR, that can accommodate the large differential motions which occur at early times within the water and between the rapidly moving water and the walls of the cavity. STELLAR calculations provide the first step of all the simulations.

To examine the effect of nonlinear deformation outside the cavity, we use a snapshot in time of pressure, stress and displacement throughout the grid to provide initial conditions for a nonlinear, 2D, Lagrangian, finite difference code that propagates the nonlinear shock through the solid material. The Eulerian and Lagrangian codes both use the same material property models, including the shear failure model for salt (Stevens et al, 1991a). The transition from the initial Eulerian calculation to the Lagrangian occurs at 25 milliseconds, after the initial shock has

defined the shape and extent of the deformation at and beyond the cavity walls, but before the bubble pulse within the cavity has re-expanded. To separately examine the effect of reverberations within the cavity, we perform the initial STELLAR calculation a second time, running it for 300 milliseconds. The spatial extent of the deformation makes it impractical to use such late time output of STELLAR as input to the Lagrangian code.

To compare synthetic seismograms to observations at local distances, the stresses and displacements of the Lagrangian calculation are saved on a monitoring surface outside of the nonlinear region, and provide input to a wavenumber calculation that simulates linear propagation into the salt beyond the nonlinear region.

6.8.3 Explosions within a spherical cavity

To understand the effects of asymmetry and fracturing we need a baseline model, so we first quantify the size and shape of the nonlinear volume about the cavity and the shear waves generated for the simplest case, explosions centered in a spherical cavity. Although the cavity remained intact between explosions, the high pressure within the cavity likely generated a larger nonlinearly deformed volume about the cavity than would a comparable air-filled cavity explosion. If the yield volume is asymmetric due to gravity or structure near the surface, that would generate shear waves.

Even if tamped, a 0.35 Kt explosion at 597 meters depth would be 6.7 times overburied, and a 0.01 Kt explosion would be 22 times overburied, so it is reasonable to expect the source volume to be approximately spherical. Near source structure, such as the hard anhydrite cap, could however affect the shape of the nonlinear region, and so the shear waves generated. Our first source calculations estimate the size and shape of the nonlinear region and the S-waves generated. We also investigate the extent of decoupling by estimating the source volume from the largest and smallest of the explosions.

Calculations for the largest water-filled cavity explosion show a nonlinear region out to approximately 10 times the cavity radius (Figure 46, middle). The hard anhydrite cap limits the upper region of nonlinear deformation, flattening out the source volume. Tensile cracking is symmetric in a small volume about the source and near the free surface (middle). The effect on shear wave production however is small, as synthetics for this source are nearly identical to those for a spherical explosion source, as shown in Figure 47 where the two sets of synthetics are overlain (top). The data (middle trace) and CLVD synthetics have an S arrival, beginning at 3.7 seconds, not produced by the CRAM or point explosion sources. The initial velocity field from the first stage of the calculations is, as expected, quite symmetric, as the explosion was detonated in the center of the cavity (Figure 46, left).

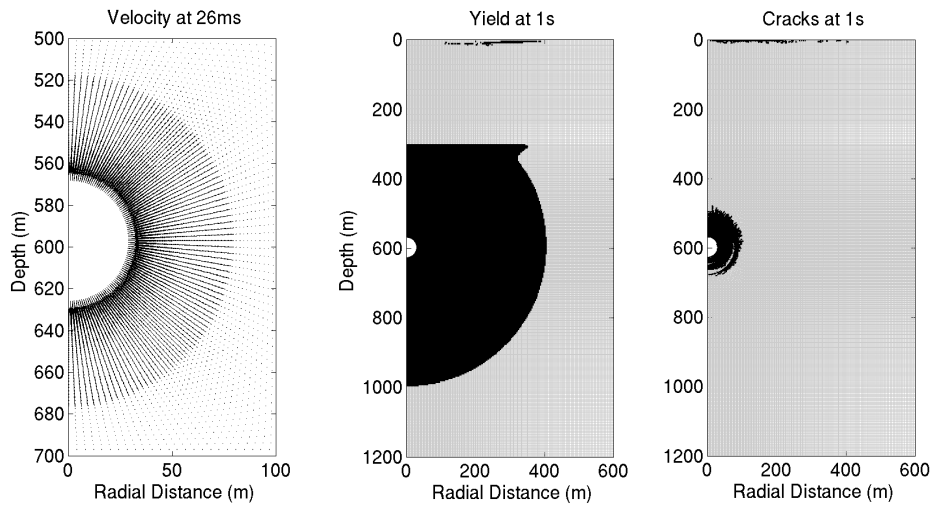


Figure 46. Initial velocity field (left), nonlinear yield region (middle), and tensile cracks (right) around the cavity for the 0.35 Kt explosion.

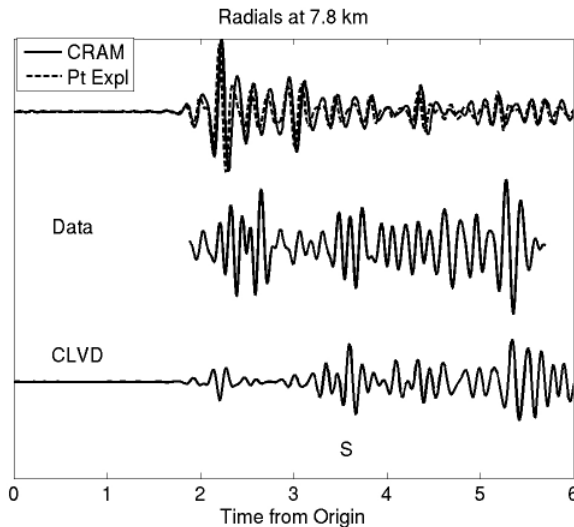


Figure 47. Radial seismograms at 7.8 km from the nonlinear source calculation (upper trace, solid) overlain with those from a spherical point explosion source (upper trace, dashed), compared with data (middle trace) and CLVD synthetics (bottom trace).

The size of the source volume indicates that this explosion is more properly considered partially coupled. Simulations for the 0.01 Kt explosion show a volume of nonlinear yielding extending to approximately 3 to 4 cavity radii, comparable to that estimated for the decoupled U.S. nuclear explosion Sterling, also in salt (Xu et al, 2009). That the observed waveforms and relative S-to-P amplitudes of the largest and smallest explosions are similar, although the predicted radii of their yield volumes differ by a factor of 3, suggests that whatever process is generating the shear waves scales similarly to the process generating the compressional waves.

Calculations similar to those described above were performed with the explosion source detonated at the top (Figure 48, upper row), and also at the base of the cavity (Figure 48, lower row). The initial velocities (left column), nonlinear volumes, and patterns of tensile cracking are all quite asymmetric. This leads to some distinct differences in high frequency near field shear

waves, but at several km the shear waves are, like those of the symmetric calculation, nearly identical to those produced by a spherical explosion source.

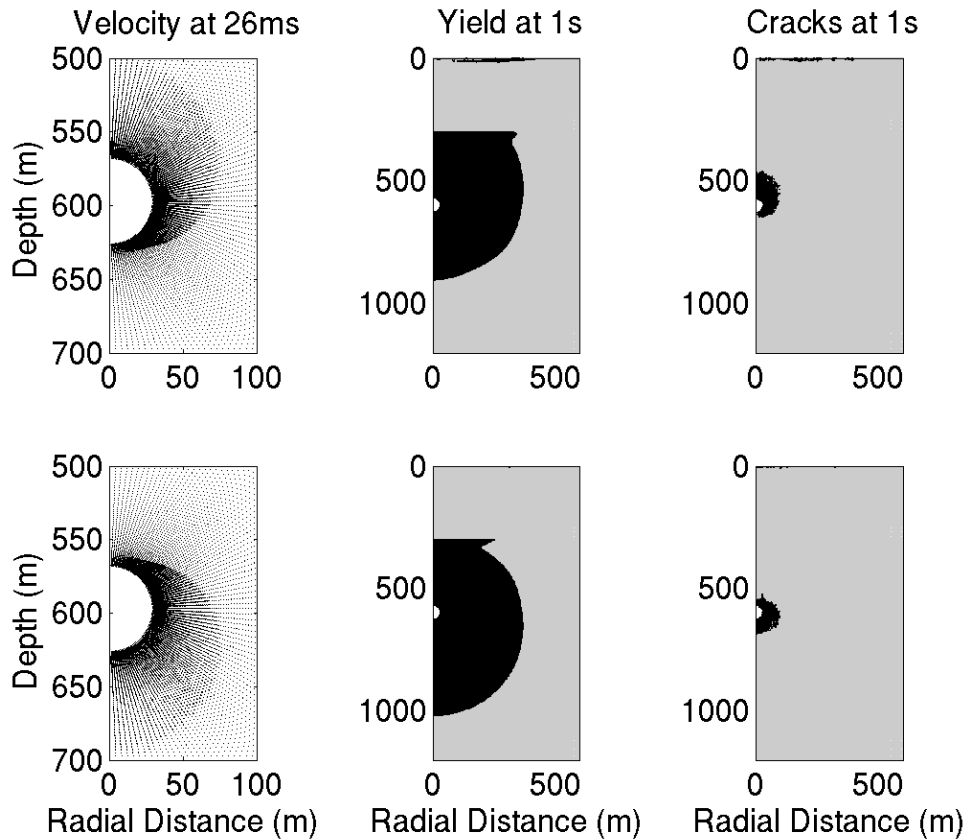


Figure 48. Initial velocities (left), yield volumes (center), and tensile cracks (right) produced by a 0.35 Kt explosion in a 28.9 m radius water-filled cavity at 600 m depth in salt for detonation at the top (upper plots) and base (lower plots) of the cavity.

6.8.4 Asymmetrical cavity calculations

Murphy et al (2001) report that the cavity has a maximum horizontal radius of 32.5 meters, the distance from the roof to the floor is only 40 meters, and the volume is 101,000 m³. Although not reported for this event, we know that the Salmon explosion, under similar circumstances (a deep nuclear explosion in salt) left a flat floored cavity due to recrystallized salt. That geometry affected the generation of shear waves by the decoupled explosion, Sterling, that was detonated in the cavity (Xu et al, 2009). We consider it most likely that recrystallization of melted salt into a flat floor is the usual situation for nuclear explosions in salt. Figure 49 shows the cavity geometry we use for further calculations.

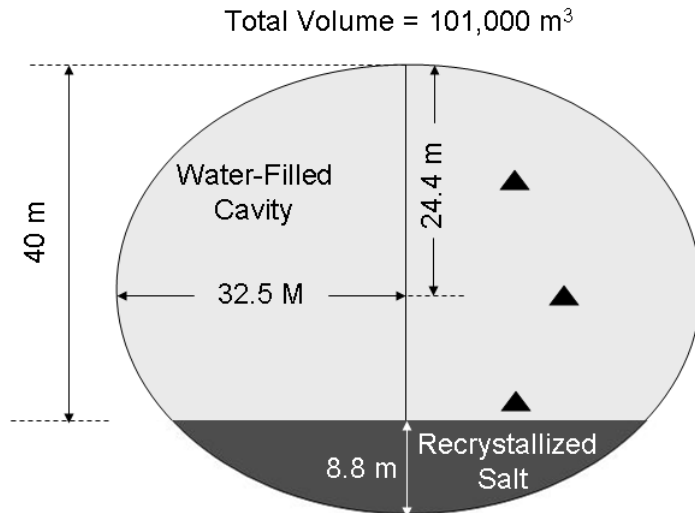


Figure 49. Configuration of the water filled-cavity used in simulations. Pressure is recorded at three locations (triangles) within the cavity 20 m from the centered explosion source.

The nonlinear yield region and the cracking due to the 0.35 Kt explosion in the elliptical cavity are indistinguishable from those of the explosion in the spherical cavity, shown in Figure 47. The nonlinear yield region and the amplitudes at local distances are approximately twice as large for the 0.01 Kt explosion in the elliptical vs. the spherical cavity. The normalized waveforms at local distances however, for both explosions in the elliptical cavity, are very similar to those for a point explosion source and for the spherical cavity explosions. The asymmetry of the cavity is on too fine of a spatial scale to strongly affect waveforms in the frequencies observed.

The Eulerian calculations provide the starting conditions of the Lagrangian calculations at 25 milliseconds. They allow us to predict the effect of the nonlinear yield region as discussed above, but the effect of cavity reverberations is neglected. By running the Eulerian calculations for 300 milliseconds, we are able to make some observations regarding the nature of the cavity reverberations. The unfiltered pressure signals at three locations inside the cavity (Figure 50, left column) are dominated by the high frequency shock wave and its reflections. Similar to offset sources, the pressure time series vary with location within the cavity. When filtered from 5 to 15 Hz however (Figure 50, right column), all the pressure time series are similar, with a second peak approximately 0.1 seconds after the initial peak due to the second expansion of the bubble pulse.

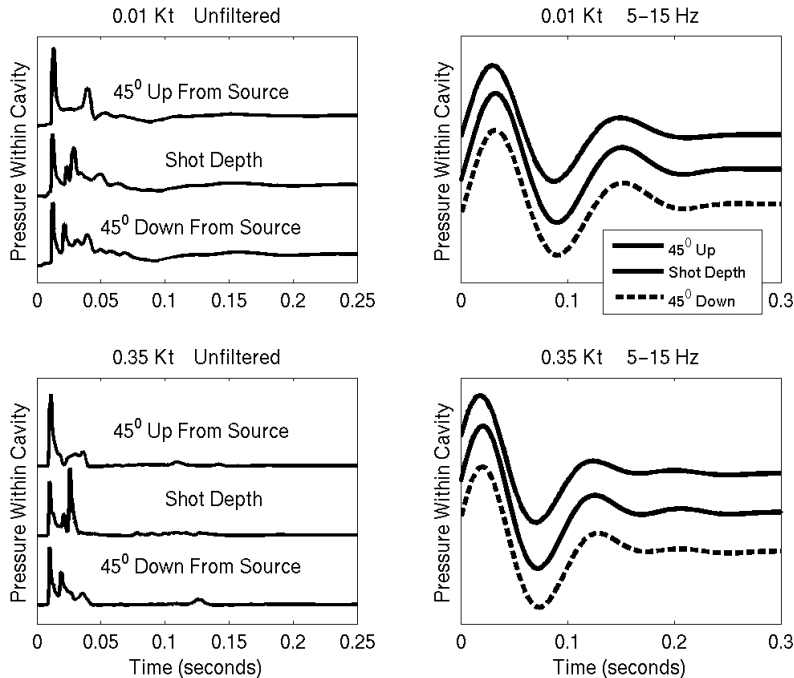


Figure 50. Pressure within the cavity for the 0.01 Kt (top) and 0.35 Kt (bottom) simulations at 3 locations, each 20 meters from the source. The unfiltered pressure signals are in the left column. The right column shows the same records filtered from 5 to 15 Hz.

6.8.5 Fracture calculations

The high pressure within the cavity could have driven open cracks, which would generate shear waves. We estimate the extent of both hydrofracturing and opening of a pre-existing horizontal crack, and the shear waves such fracturing could generate.

In an explosion, preexisting cracks connected to the cavity are driven open by penetration of the high-pressure gas. The extension of these explosively driven fractures depends on the interaction between the flow of gas into the fractures and the nonlinear stress wave dynamics of the surrounding solid. The stress wave dynamics are important in controlling the global stress field, the expansion of the cavity and the pressure within the cavity, and the effects of dynamic fracturing involve mass transfer from the cavity and fluid pressure in the nonlinear rock elements. A root finder method was developed and tested (Nilson et al., 1991) to model the dynamic fracture propagation due to explosions in a nonlinear inelastic constitutive material. This method can handle the important features controlling the speed and extent of explosively driven hydrofractures, such as effects of heat transfer from the fluid to the rock, and seepage of fluid from the crack into the rock.

With overburden pressure of about 130 bars and peak cavity pressure for the 0.35 Kt explosion at 269 bars, the dynamic region in this calculation extends only 3m into the salt and has no obvious preferred direction (Figure 51, right). The results are similar for the offset sources.

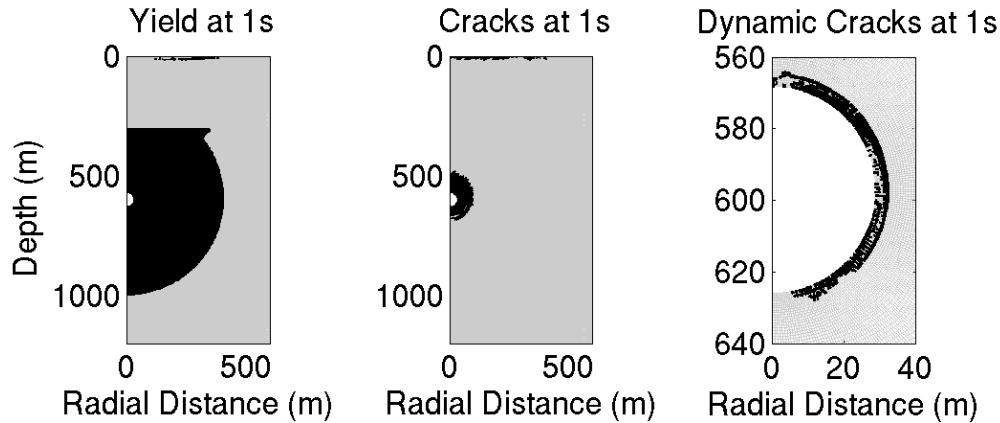


Figure 51. The yield region (left), the tensile cracking region (middle), and the dynamic cracking area (right) for fully pressurized fractures. The dynamic fracture region is restricted to about 3 m into the salt.

We also performed a calculation similar to the symmetric one (Figure 46), but with the addition of a horizontal crack radiating out from the cavity. As with the hydrofracture calculation, the peak cavity pressure of 269 bars overcomes the overburden of 130 bars, and so opens the crack outward. The results are not shown since the yield and tensile crack distribution is similar to those in Figure 46. The preexisting crack was opened just 50 m into the salt in the initial 300 ms and then closed to within 1 m. of the cavity due to depletion of the cavity pressure. There was no shear movement on the crack and the size of the opening was too little to affect the waveforms outside of the near field, which, like those of the previous nonlinear calculations are similar to those of a spherical explosion source.

6.8.6 Analytic Offset source calculations

As discussed above, the purpose of the coupled Eulerian/Lagrangian calculations is to propagate the shock wave into the external material to calculate the nonlinear response and corresponding motion. Xu et al (2009) performed similar calculations for the Sterling decoupled explosion in salt, and were able to match the near field waveforms quite well. In that case, the near field shear waves were found to be generated by the interaction between the shock wave and the non-spherical cavity wall. However, it was also observed that there was a longer duration shear wave that had the same polarity both above and below the cavity that was not reproduced by the calculations. This type of motion corresponds to a dipole and results from differences in pressure on the cavity wall that cause an up and down motion of the entire cavity (Stevens and Baker, 2009).

In the calculations described above as well as the earlier calculations, the cavity is rezoned to a single pressurized zone at the time of overlay to the Lagrangian code, so any cavity reverberations and the corresponding response of the cavity are excluded. As described above, we also ran Stellar for a longer period of time to try to reproduce this type of motion, but were unable to unambiguously separate out the longer period shear waves that correspond to this motion. The dipole generates shear waves similar to the CLVD, and may exist without any nonlinear deformation, and so may be a relatively stronger source in the smaller explosions. The dipole must vanish in the long period limit, but may generate substantial shear waves in the 5-15

Hz frequency band of the observations analyzed in this paper. To show this, we calculated the far field P and S waves for an offset explosion in a 28.9 meter radius spherical cavity using the method of Stevens and Baker (2009), and using the same technique for modeling cavity reverberations discussed in that paper. Figure 52 shows the simulated pressure time history at opposite points on the cavity wall (left), and the corresponding P and S spectra (right), which are comparable in the frequency band of interest. We suggest therefore that a vertical dipole source caused by cavity reverberations and differences in amplitude and timing of pressure pulses on the cavity wall, and the corresponding cavity response, may generate a significant component of the shear waves from the water-filled cavity explosions.

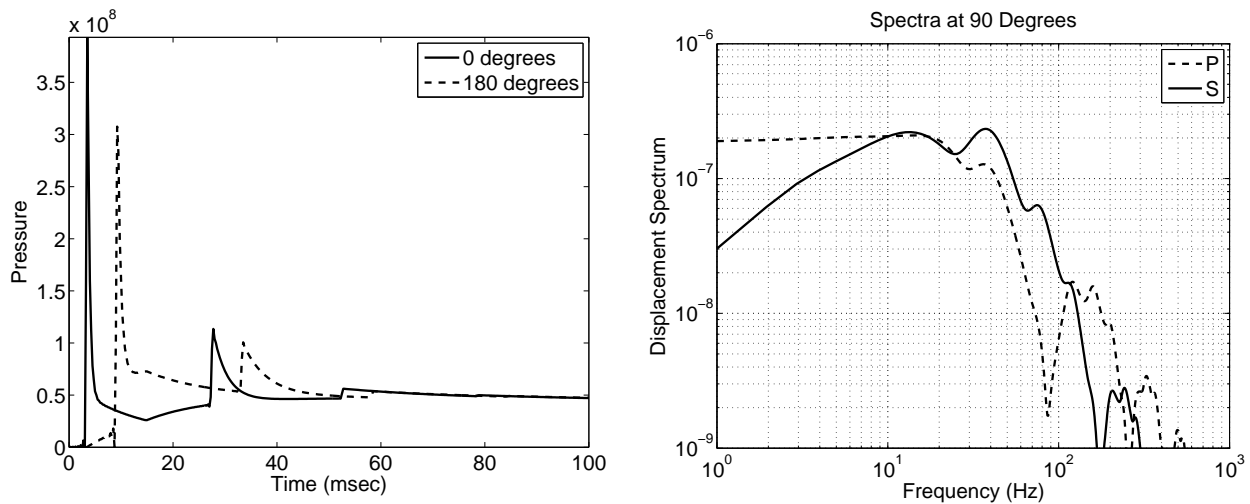


Figure 52: Left: pressure time history on cavity wall closest to (0 degrees) and farthest from (180 degrees) the explosion. Right: Far field P and S spectra at 90 degree takeoff angle.

Note that if the S-waves are dominantly generated by cavity motion resulting from asymmetric time and amplitude pressure variations inside the cavity, we would not expect to see the bubble pulse peak in the S-wave spectra. That is, while the P-waves may be dominated by the spherically symmetric bubble pulse pressure waves, the S-waves are dominated by approximately vertical pressure reverberations within the cavity.

6.8.7 Point force, tangential data and more prominent S2

Just as the CLVD provides an approximation to the often inverted cone shaped region of nonlinear deformation above an explosion source, a vertical point force provides an approximation to the vertical cavity motion described in the previous section. While both generate S-waves, the CLVD and vertical point forces have different radiation patterns. In this section we address whether either source better predicts observations. There are two observations in particular that may bear on this.

The first observation was seen in Figure 33. While all three of the water-filled cavity explosions had similar S-to-P amplitudes ratios for S1, the S2 amplitude seems to decrease with explosion size. Also, S2 persists much longer in the smallest explosion record. Figure 53 shows the 0.01 Kt vertical component record (top trace, the same seismogram as in Figure 33), compared with the sum of an explosion plus CLVD synthetic (middle trace) and an explosion

plus vertical point force synthetic (bottom trace). Both S-wave sources are at 597 m, the same depth as the spherical explosion. The initial S arrival is similar in both synthetics, but while the CLVD generates a short-lived arrival, the S-wave of the point force synthetics persists for much longer. The CLVD S-wave radiation pattern has a horizontal null, where the point force S-wave radiation pattern is peaked. This affects the modal excitation of the two sources, bringing about the changes seen in Figure 53. That the size and persistence of S2 are greater for smaller events would be consistent with a relatively larger role of vertical oscillations of the cavity for those events.

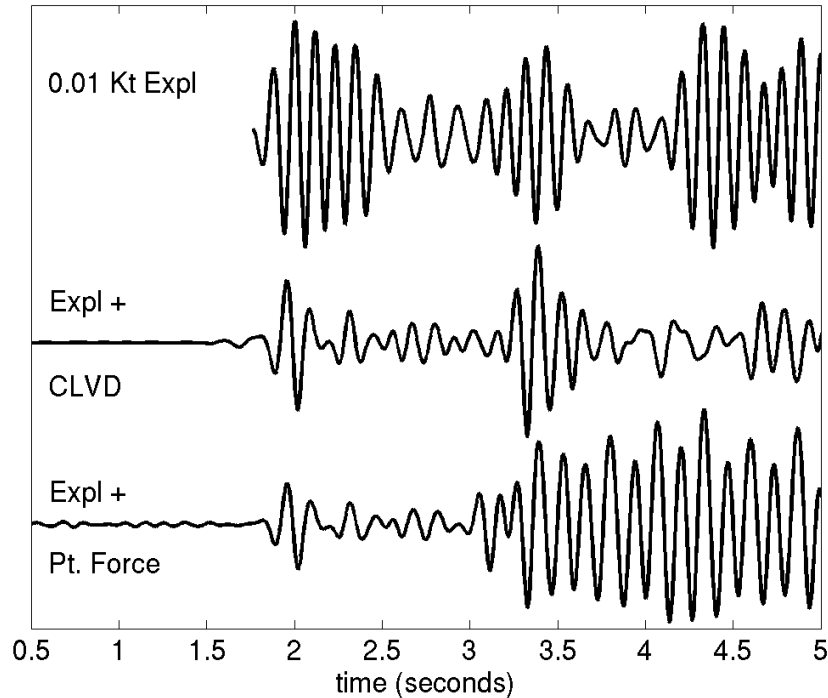


Figure 53. Vertical component data at 7.8 km for the 0.01 Kt explosion (top), a spherical explosion plus CLVD (middle), and a spherical explosion plus a vertical point force (bottom).

There was just one three component record at local distance, at 4.64 km. Figure 54 shows all three components of those velocity records, filtered from 5 to 10 Hz (left). The vertical (solid, lower trace) and Hilbert transformed radial (dashed, lower trace) are overlain, and come into alignment at 1.9, indicating the S-arrival. That is exactly the predicted S minus P time. There is a very distinct S arrival on the tangential component (upper trace), but it is later than the radial S and is somewhat smaller. To assess whether the later arrival time of the tangential S-wave is consistent with source generation, we compare the observations with point force synthetics (right). The tangential component (upper trace) is due to a horizontal point force, and the vertical and radial are due to a vertical point force. In this velocity structure, tangential S generated at the source does propagate more slowly than the SV, consistent with the observation. A horizontal point force would be an appropriate model for a horizontal offset of the explosion source or asymmetry of the cavity.

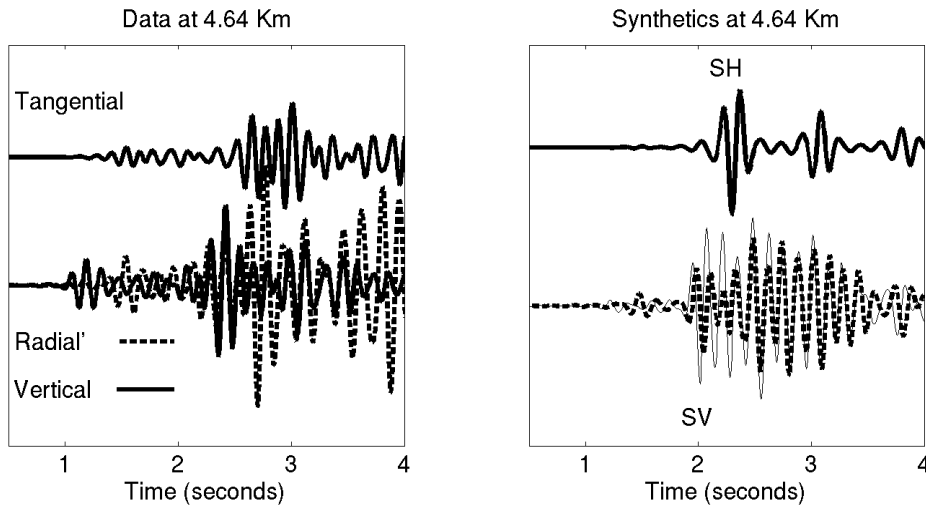


Figure 54. Observed (left) and synthetic (right) tangential (upper trace) and overlain vertical (lower trace, solid) and Hilbert transformed radial (lower trace, dashed) seismograms at 4.64 km from the 0.08 Kt explosion, filtered from 5 to 10 Hz. The tangential synthetic S from a horizontal point force arrives later than the radial and vertical S from a vertical point force.

6.8.9 Summary of Conclusions from Calculations

Nonlinear source calculations indicate the extent to which decoupling varies, as the radii of the nonlinear volumes range from approximately 10 to 3 cavity radii from the largest to the smallest explosion. The similarity of the waveforms to those generated for a spherical point explosion indicates that asphericity of the nonlinear volume about the cavity predicted by the calculations is insufficient to generate the shear waves observed in the data. Similarly, while emplacement of the source near the top or bottom changes the shape of the yield volume and the small area of tensile cracking, and generates significantly different near field shear waves, the local seismograms are not strongly affected. Simulations that incorporate a flat floor and the ellipticity of the cavity also produce complicated high frequency waveforms in the near-field, but longer period shear waves that were observed at local distances could not be clearly identified. Cracking simulations, either by hydrofracturing or opening of a pre-existing horizontal crack, similarly do not produce the shear waves observed in the data.

Analytic calculations that simulate the variation in amplitude and timing of pressure around the cavity due to an offset source do predict S-waves at the frequencies observed. Such a source causes vertical oscillations of the cavity. Point force calculations, which simulate a similar source, are consistent with the persistence of the second S-wave arrival for smaller explosions, and so are consistent with a relatively larger role for cavity oscillations for the smaller events. Simulations of a horizontal S-wave source at the same location as the P and SV sources predict a later SH than SV arrival, consistent with the one tangential component record available.

6.9 Discussion

The important result demonstrated by analysis of the data is that significant shear waves are generated by small explosions in an approximately spherical water-filled cavity, independent of contributions from P or Rg scattering. The data are matched approximately by a point explosion plus a CLVD at the same source depth with the same moment. However, 2 dimensional

nonlinear source calculations in a laterally homogeneous model do not generate a sufficiently large aspherical component of the source volume to produce the shear waves observed, even for an offset source. Calculations also indicate that the asymmetry of the cavity, that is, its ellipticity and flat floor, is too small to generate the shear waves observed. Simulations of hydrofracturing and opening of pre-existing cracks also fail to produce the shear waves observed.

A dipole source caused by variations in the amplitude and timing of pressure on the cavity wall is a likely source for additional shear waves since it would be unusual for the cavity to be exactly spherical and the source exactly centered, and any other configuration will generate some motion of this type.

6.10 Conclusions

S waves are generated at or very close to the source by explosions in an approximately spherical water-filled cavity. The P but not the S spectra of the explosions have a 9 Hz bubble pulse. This spectral difference is inconsistent with shear wave generation by P-wave scattering. The high frequencies and 597 m depth are inconsistent with generation by Rg scattering. The observed P and S travel times are consistent with generation at the source. While the travel times are not inconsistent with scattering to S, such scattering would have to be nearly instantaneous and occur only very close to the source, as the S arrivals are impulsive, temporally compact, and move out smoothly with distance.

Nonlinear axisymmetric numerical simulations of deformation about the cavity do not generate shear waves as large as the observed shear waves, even when taking into account the near source earth structure, the possibility of an offset source in the cavity, or an elliptical and flat-floored cavity. Similarly, simulations predict that even the largest water-filled cavity explosion is too small to generate the observed shear waves by hydrofracturing or opening of a pre-existing crack. While there could be more asymmetry in the source than we have modeled in these simulations, observation of shear waves from cavity decoupled explosions appears to be the rule rather than the exception (Stevens et al, 2006a), so the physical mechanisms that cause them cannot be unusual or dependent on the particular characteristics of one event or location. The simplest explanation for source generated shear waves from the water-filled cavity explosions are oscillations of the cavity, due to some asymmetry. Simulations for one type of asymmetry, an offset source in a spherical cavity, produce shear waves at the frequency observed. The elliptical cavity with a flat floor also produces variations in the pressure field around the cavity. Relatively greater contributions from such oscillations for the smaller explosions is consistent with the more pronounced bubble pulse peak in the smaller explosions, and the greater consistency of smaller records with point force vs. CLVD synthetics.

7. ISRAELI ORON DECOUPLING EXPLOSIONS

7.1 Introduction: Source Parameters, Previous Work, and Local Spectra

The Israeli Oron decoupling experiment of 2006 was described in detail in Gitterman et. al, 2007a and 2007b. We summarize briefly here. The explosions consisted of one tamped and two partially decoupled explosions of 1240 kg of ANFO, equivalent to 1000 Kg of TNT (Table 5). All were recorded on a common set of local to regional stations. Using peak amplitudes from 40 to 140 km, Gitterman et. al (2007b) find decoupling factors of 6.4 (explosion 1) and 2.8 (explosion 2) from 1 to 20 Hz. For the same set of stations, they observe higher S-to-P ratios for the fully tamped explosion, and the smallest ratios for the deepest and most decoupled explosion. The S-to-P ratio of explosion one matches that of explosion two at two stations, and is very similar to that of explosion three at two other stations, which must reflect either source radiation, very near source propagation differences, or the limit of accuracy of the measurements.

Table 5: Source parameters of the three Israeli decoupling explosions.

Event ID	Depth (m)	Cavity Size			Vp (km/s)	Vs (km/s)	P (g/cm ³)
		Volume (m ³)	Width (m)	Height (m)			
1	26.5	4	2.2-2.4	1.6-1.7	1.71-1.82	0.87	2.4-2.5
2	63	14	2.7-3.0	3-3.3	1.71-1.82	0.87	2.4-2.5
3	30	tamped	tamped	tamped	1.95-2.13	1.02	2.2-2.4

We focus our analysis on near source acceleration records, where attenuation has the least effect. Figure 55 shows the relative locations of the sources and stations.

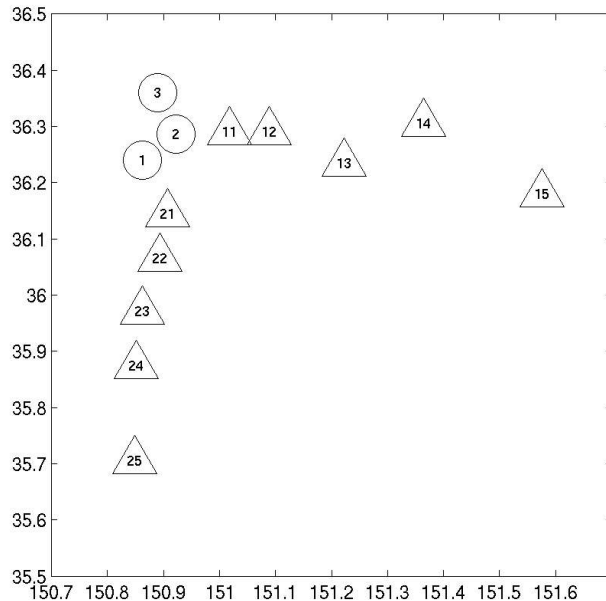


Figure 55. Location of explosions (circles) and accelerometers (triangles).

The spectra of each event is distinct, with explosion two, the least tamped explosion, producing smaller amplitudes below 10 Hz but the largest amplitudes above 25 Hz. Figure 56 shows the same spectra as interpreted by Gitterman et al (2007b), although we use a multi-taper estimate. Cavity reverberations are offered as an explanation for the spectral peaks at 40, 70, and

100 Hz in explosion 2 records, and the overall larger high frequency amplitudes, although Gitterman et al. (2007b) also note the greater source depth and the difference in the source medium (phosphate marl for explosion two vs chalky marl for the shallower explosions).

It is important to try to understand these spectral differences if we later hope to identify and use differences between P and S spectra to better understand their generation. There are some contradictions with the proposed interpretation of spectral peaks in the explosion two records. At 40 Hz, there is a spectral peak not only in explosion two records, but also in records of the tamped explosion, which suggests that it's a structural effect rather than due to cavity reverberations. Also, all three events have apparent spectral peaks at 100 Hz, which appear more likely due to an anti-aliasing filter. That however still leaves the higher frequency of explosion two unexplained.

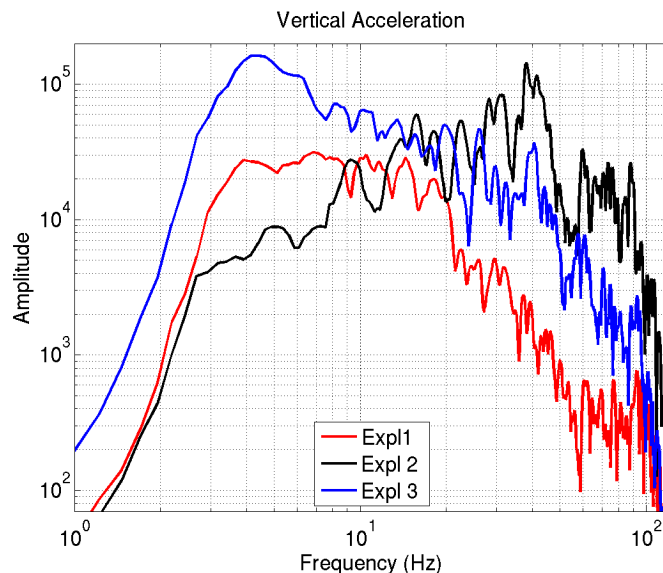


Figure 56. Vertical acceleration spectra at station 25, 506, 585, and 655 m respectively from explosions 1, 2, and 3.

In addition to the greater depth, and different source media, we expect the partial decoupling to reduce the apparent yield of the explosion. Figure 57 (left) shows the Mueller-Murphy source spectra for the known source velocities, densities, depths, and yields, with the yields scaled by the decoupling factors determined by Gitterman et al. (2007b). The observations (Figure 56) are consistent with the smaller amplitudes at low frequency of explosion two and the higher frequencies above the corner of the tamped explosion 3 and less strongly decoupled explosion 1 of the Mueller-Murphy source. The Mueller-Murphy predicted corner frequencies however are lower than those observed. This is in part because the parameters associated with source media properties have not been estimated for marl, so we substituted the corresponding parameters for tuff. Marl however is softer and weaker than tuff, so the predicted corner frequencies for marl would actually be higher than those shown, so more consistent with observations. Furthermore, the Mueller-Murphy source was not developed for such shallow explosions, and likely underestimates the corner frequencies on that account as well. To address this, we also determine the RVP spectra based on a numerical calculation (upper right). The RVP-based corner frequencies are much higher, and closer to those observed for the partially decoupled explosions, although the prediction is higher than observed for the tamped explosion.

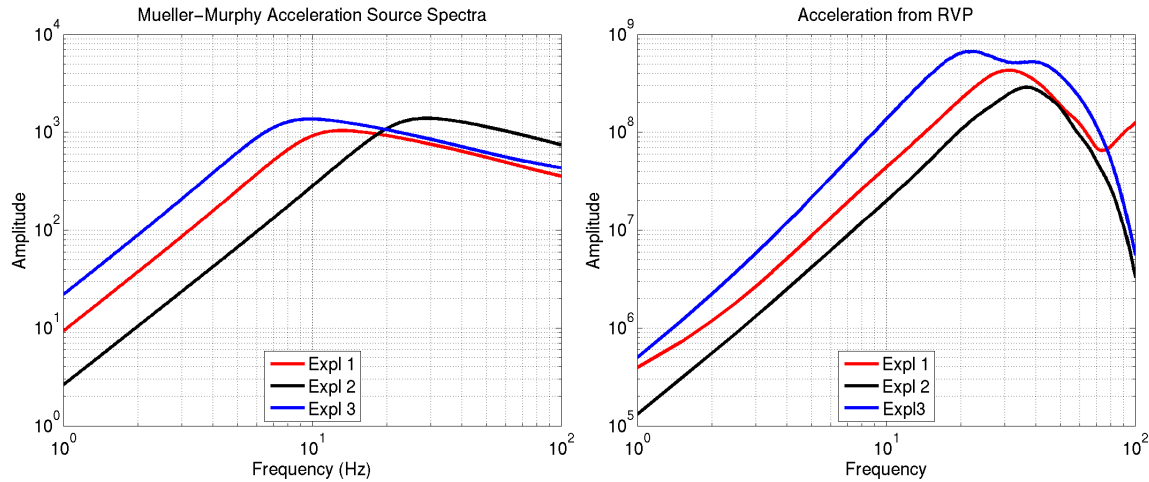


Figure 57: Predicted (Mueller-Murphy) acceleration spectra for the depth and yield, scaled by the decoupling factor, of the explosions (left), and RVP acceleration spectra from numerical calculations (right), for comparison with the observed acceleration spectra of the three explosions at station 25 (Figure 56). The Mueller-Murphy source is based on the parameters for tuff.

Greater excitation of higher modes by explosion 2 provides another possible explanation for its higher frequencies. Figure 58 (left) shows the earth structure at the site of the three explosions. The structures are essentially identical for the three sites except for a small difference in the depth of the shallowest layer. Also shown in Figure 58 are the shot depths. Notice that Shot 2 is close to the material interface between the lower velocity “Chalky Marl” above and the higher velocity, but less dense, “Phosphate Marl” below. This interface has a significant effect on the modal structure and excitation of high frequency surface waves. Figure 58 (right) shows the excitation function of the first few surface wave modes at a frequency of 40 Hz in this structure, plotted as a function of depth. Notice that the excitation function increases substantially near the 50 meter interface. Shot 2 is just below the region of higher excitation, however the nonlinear region of explosions generally extends higher than the shot depth, so if Shot 2 deformed the material between shot depth and 50 meters, it would have generated larger higher mode surface waves.

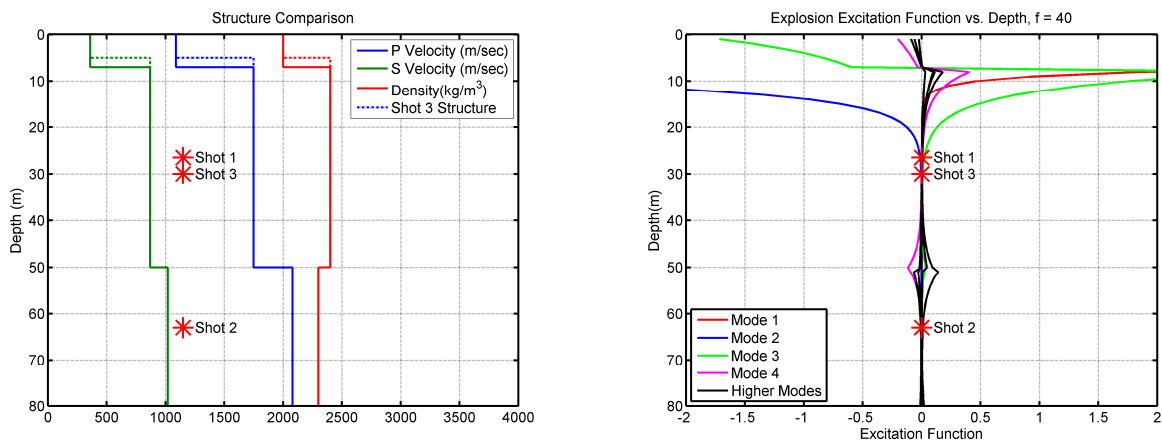


Figure 58. Left: Earth structure and source depth of the 3 decoupled explosions. Right: 40 Hz modal excitation by a point explosion source in this structure.

Figure 59 compares the acceleration spectra recorded at station 25 with synthetic spectra. The synthetic spectra were generated with a modal code using the first 50 modes and the earth structures shown above, for point explosion sources at the given source depths, and for a shallower depth (55 meters) for Shot 2. Even for the actual shot depth, there is an enhancement of high frequencies vs. low frequencies compared to Shots 1 and 3. For the 55 meter depth source, the enhancement of high frequencies is substantial.

The low frequency offset observed in the data is not apparent in the synthetics, and this shows that there is some decoupling in these explosions, even though they are substantially overdriven.

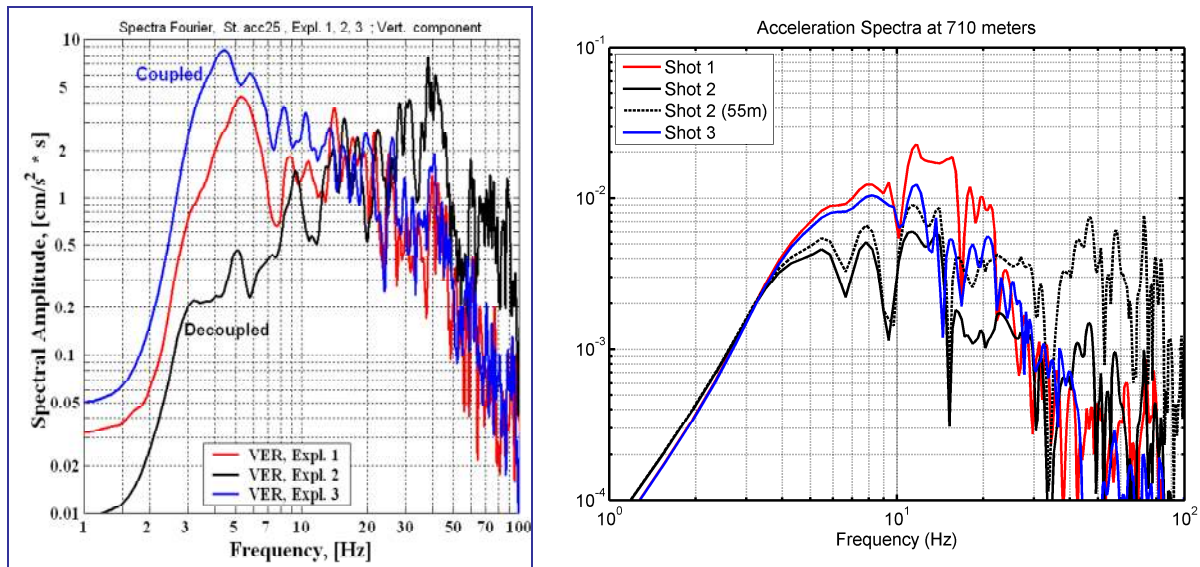


Figure 59. Observed acceleration spectra (left) and synthetic acceleration spectra (right) for the three explosions described in the text, and for explosion 2 moved to a shallower depth. High frequency spectral differences are due to source depth and structure; low frequency differences are caused by decoupling.

7.2 Identifying the shear waves: Particle traces and record sections

Our goal is to identify the mechanisms that generate shear waves from the decoupled explosions. To do so, we must isolate the shear waves, so they can be compared with the corresponding P waves, and with shear waves from the tamped explosion. Nine 3-component accelerometers recorded the three explosions from 100 to 700 m from the sources. These provide good resolution up to very high frequency. We will use group velocities and particle motion to identify the shear waves.

One problem we must address in isolating P and S arrivals is that at lower frequencies they overlap in time. Figure 60 shows records for explosion 2 at stations 21 to 25, from 3 to 7 Hz. We cannot unambiguously identify and separate P and S phases from these records into separate time windows.

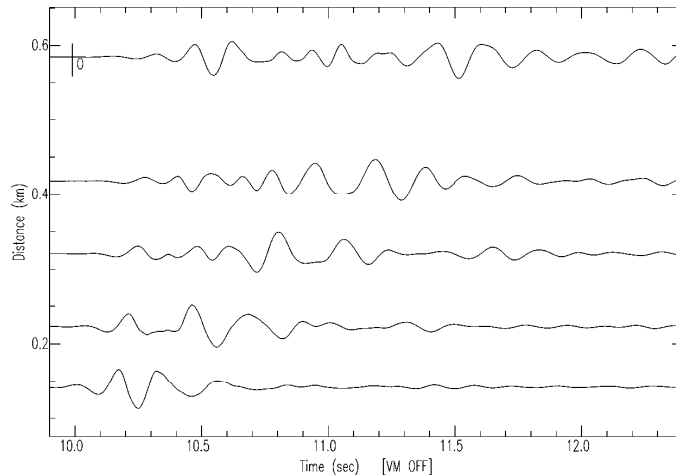


Figure 60. Vertical component records of explosion 2 from stations 21 to 25, filtered from 3 to 7 Hz.

The shear waves are made up of higher mode Rg, and generally have retrograde elliptical particle motion, so the vertical component and the Hilbert transformed radial component are in phase for shear wave and the fundamental mode Rg arrivals, but are out of phase for P waves. This is illustrated in Figure 61, which shows the vertical component and Hilbert transformed radials of explosion 2, filtered from 3 to 7 Hz and overlain. To isolate the fundamental and higher mode Rg phases, we introduce a special type of product trace record section. This product trace is the point-by-point product of the vertical component and the Hilbert transformed radial component, which effectively reduces the magnitude of the out-of-phase P arrivals and accentuates the Rg (Figure 62). This is small for P-waves and strongly positive for higher mode (i.e. S) and fundamental mode Rg. The large oscillations between initial arrival and the Rg in the vertical component records (Figure 60) are gone. We can use this type of record section to help identify the shear waves and isolate them from the P-waves when the phases overlap in time. The particle motion becomes more complex at higher frequencies, so we use the product trace record sections to identify higher mode Rg mostly below 10 Hz. Fortunately, that is where it is most needed, as at higher frequencies the phases don't overlap.

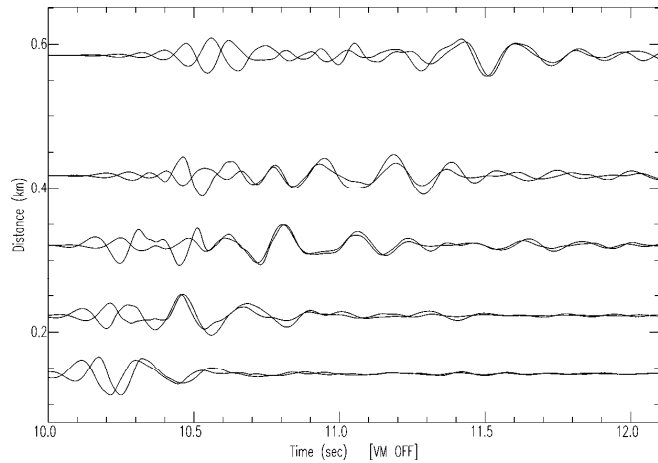


Figure 61. Vertical and Hilbert transformed radial record section, from 3 to 7 Hz, from stations 21 to 25.

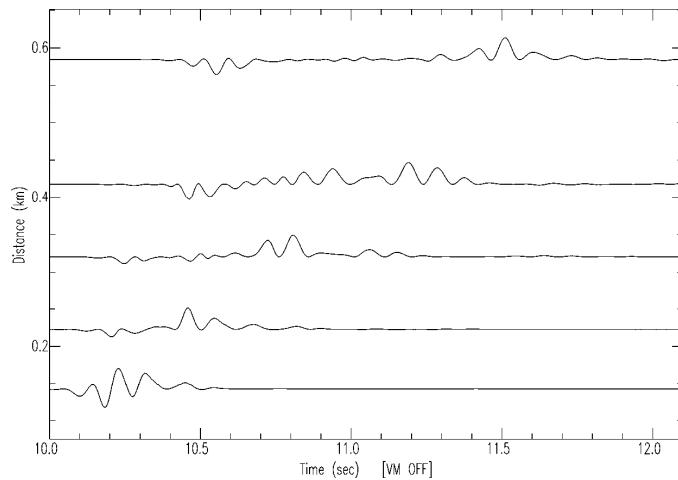


Figure 62. Product trace record section at 3 to 7 Hz, from stations 21 to 25.

The reported time of the records appears to be incorrect, as the origin time reported is later than the P arrival in the records. For stations south of the explosions, the relative timing appears to be accurate, based on consistent moveout of all phases. All those records begin at the same time. For stations east of the explosions, relative times reported for the records are incorrect, as apparent arrival times do not correspond to relative distances, with the first arrival 15 seconds later than the others. Those records have different reported begin times. Station 13 malfunctioned, and the particle motion at station 15 is complex, presumably due path effects, making phase identification problematic there. Although data from some of the eastern line of stations will be used, we illustrate separation of the S phase with record sections from just the southern line, stations 21 through 25.

Figure 63 shows product trace record sections for the tamped explosion in a range of passbands. At the lower frequencies, the fundamental mode is dominant. At higher frequencies, the arrivals are earlier. This is not likely reverse dispersion of the fundamental mode, as the velocity structure there does not decrease with depth. Rather, it appears that the first higher mode, or possibly multiple higher modes, begin to dominate. This is highlighted by a comparison of the product trace in different passbands at station 24, 488 meters from explosion 3 (Figure 64).

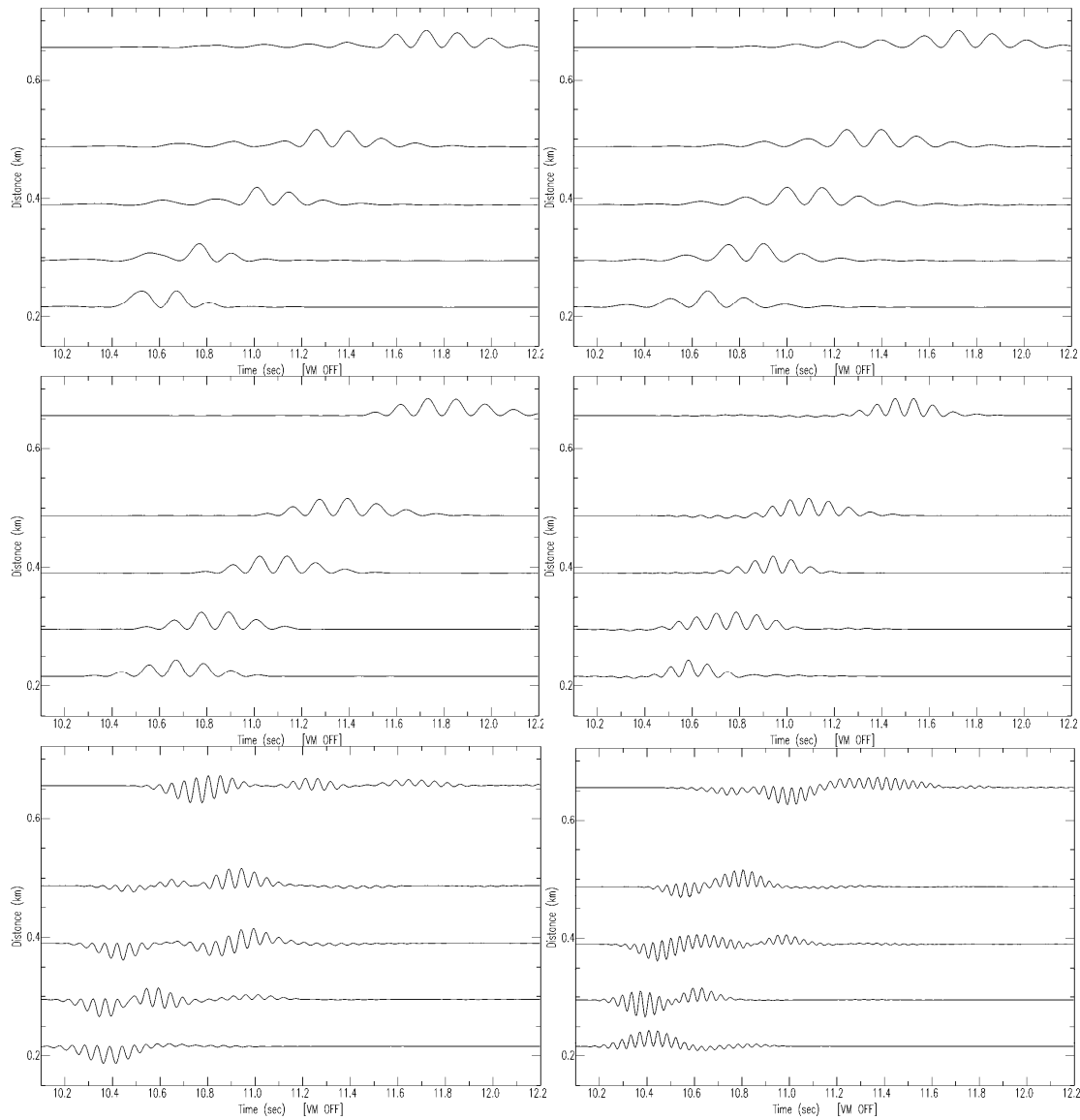


Figure 63. Product trace record sections for stations south of the explosions, at 0.5 - 1.5, 1.5 - 3, 3 - 5, 5 - 8, 8 - 11, and 11 - 15 Hz from left to right and from the top down.

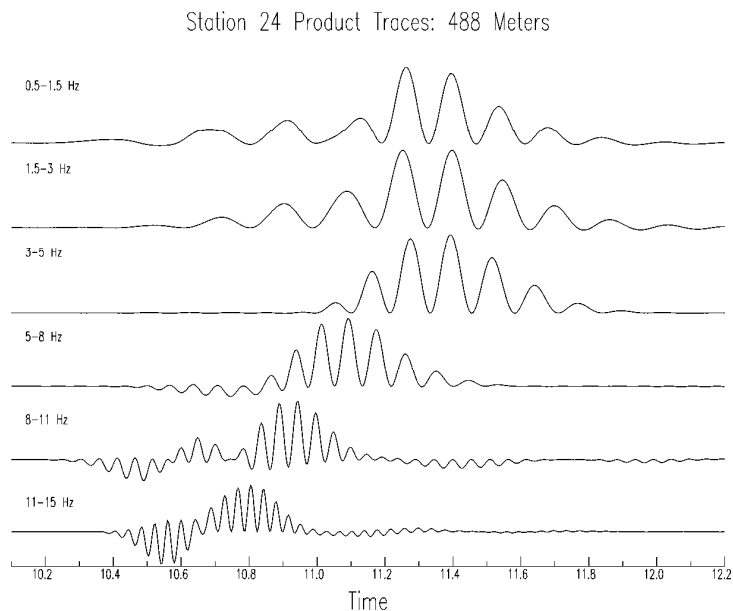


Figure 64. Product traces for explosion 3 at station 24, 488 meters from the source, in 6 passbands.

The tangential component records also assist in identification of shear waves, but complicate the explanation of their existence, as the usual mechanisms invoked generate only SV. All three components of explosion 3 recorded at station 25 (655 m), in the same passbands as previous figures, show prominent tangential arrivals between the P and fundamental mode Rg arrivals (Figure 65). Below 3 Hz, the earlier tangential arrival is even larger than the Rg. Above 8 Hz it is also very clear. At 3 to 5 and 5 to 8 Hz, it is clear, and in the latter passband, it coincides with a radial arrival, although it is smaller than the radial and vertical fundamental mode Rg arrival. While this strongly supports an interpretation of the arrival as an S-wave, it brings up two questions. What is the mechanism behind the tangential S-wave, and is it the same as the mechanism behind the SV? We can most easily isolate the shear wave for comparison with P, and with S from the other explosion, by using the tangential component, but to assess whether it has a common source with SV, we must compare it with S on the radial, which is more prominent than the vertical S arrival.

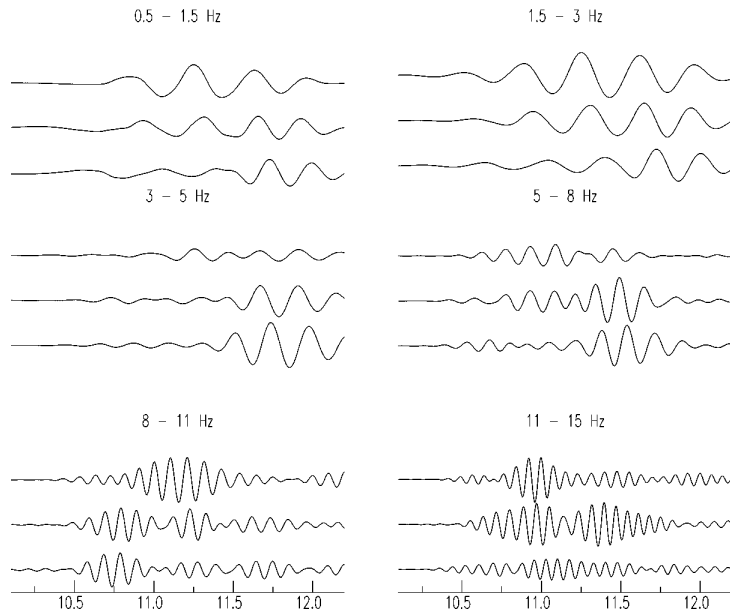


Figure 65. Three component records of explosion 3 at station 25 (655 m) in 6 passbands. All components in each passband are plotted on the same scale.

We next examine the same set of product trace record sections and individual seismograms for explosions 1 and 2, in the same passbands. Figure 66 and Figure 69 show product trace record sections for the same passbands and stations as Figure 63, but for explosions 2 and 1. Figure 67 and Figure 70 show the explosion 2 and 1 records at station 24, in the same passbands as Figure 64. Figure 68 and Figure 71 are similar to Figure 65, showing the 3-component explosion 2 and 1 records at station 25 in the same passbands.

The similarity of the S-waves in these figures is much greater than their differences. It is difficult to discern a distinct radial or vertical component S-wave below 5 Hz in these records. Only at 5 to 8 Hz does a clear arrival, preceding the fundamental mode Rg time, emerge. At lower frequencies, the record sections have a single arrival. The fundamental mode also dominates the product traces at station 25 up through 5 Hz, as evidenced by the normal dispersion. Only at 5 to 8 and 8 to 11 Hz does an earlier arrival stand out in the product traces. Similarly, no strong tangential arrival can be identified as a clear S wave until we reach 5 to 8 Hz, although the tangential arrival begins to emerge in the 3-5 Hz passband for each event. The arrival also persists, although not dominantly, at higher frequencies.

The greatest difference is between the explosion 2 records and those of explosions 1 and 3. At 0.5 to 1.5 Hz, distinct arrivals from explosion 2 are unclear. This may be due to much smaller signal amplitude due to the greater decoupling of explosion 2. The amplitude is also diminished by the greater overburden, as explosion 2 is at twice the depth of the other explosions. The greater depth may also reduce the amplitude of Rg, which is the dominant phase at 0.5 to 1.5 Hz. An alternate explanation is that lower frequency seismic energy was not generated, due to the small volume of the nonlinearly yielding region outside the cavity. If that is so, a lower frequency cutoff of the source spectra than predicted given the observed amplitude may help to identify decoupled explosions. Another difference is in the relative prominence of the S-wave. It is most dominant relative to P and Rg at 5 to 8 Hz, and is the only phase apparent in the explosion 3 product traces in that passband. It is still dominant in the explosion 1 product traces

in that passband, but, while still apparent, it is not always the largest amplitude arrival in the explosion 2 product traces.

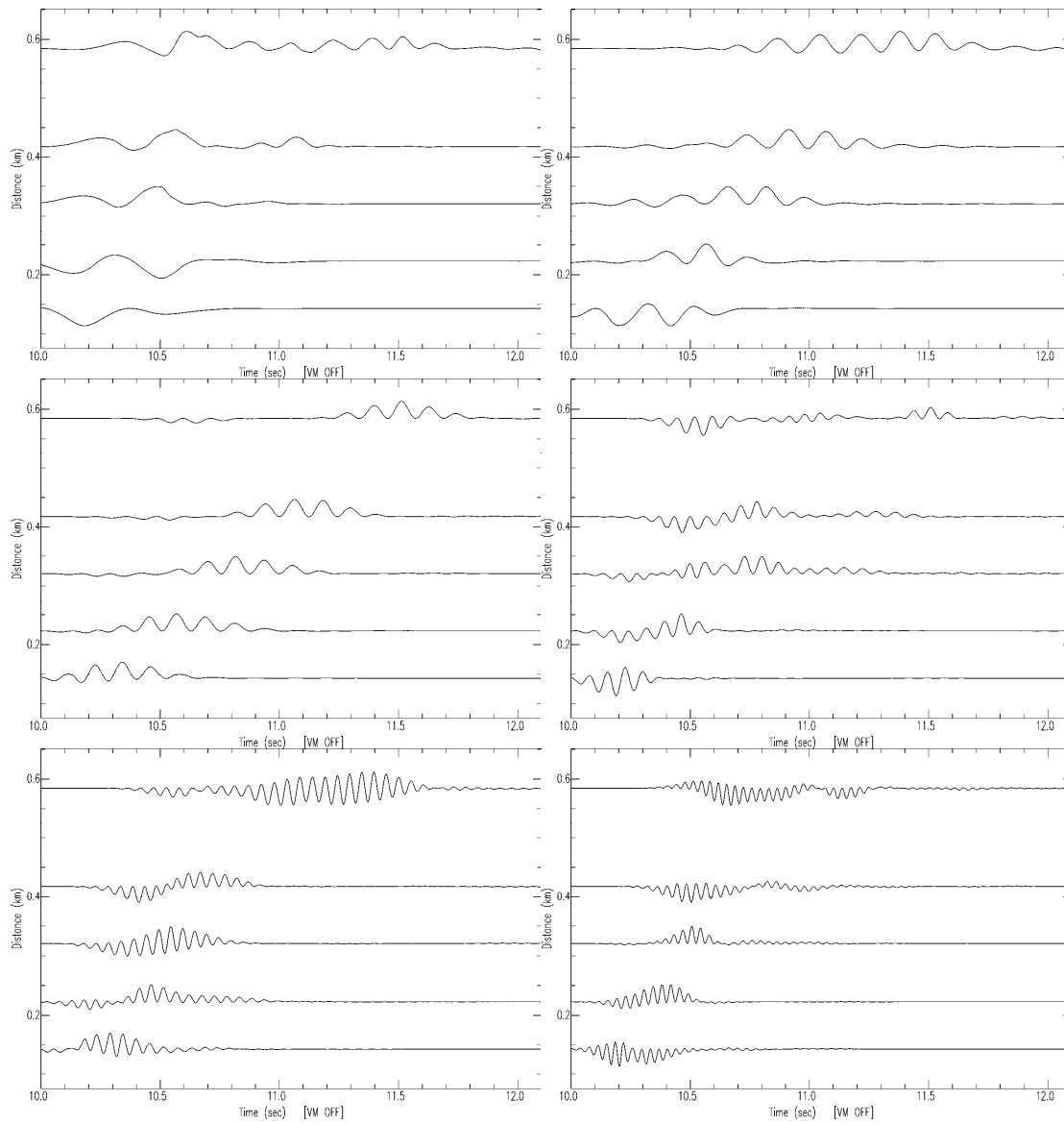


Figure 66. Product traces of the vertical and Hilbert transformed radial records of explosion 2 for stations south of the source, at 0.5 - 1.5, 1.5 - 3, 3 - 5, 5 - 8, 8 - 11, and 11 - 15 Hz from left to right and from the top down.

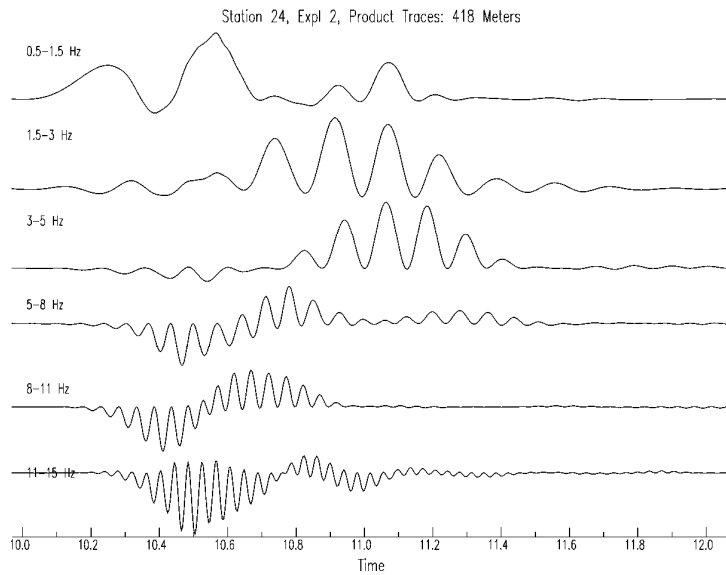


Figure 67. Product traces for explosion 2 at station 24, 418 meters from the source, in 6 passbands.

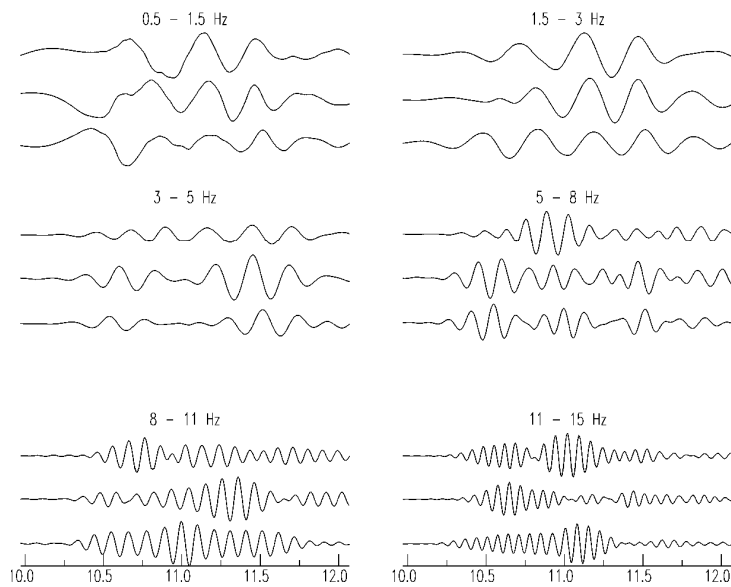


Figure 68. Three component records of explosion 2 at station 25 (585 m) in 6 passbands. All components in each passband are plotted on the same scale.

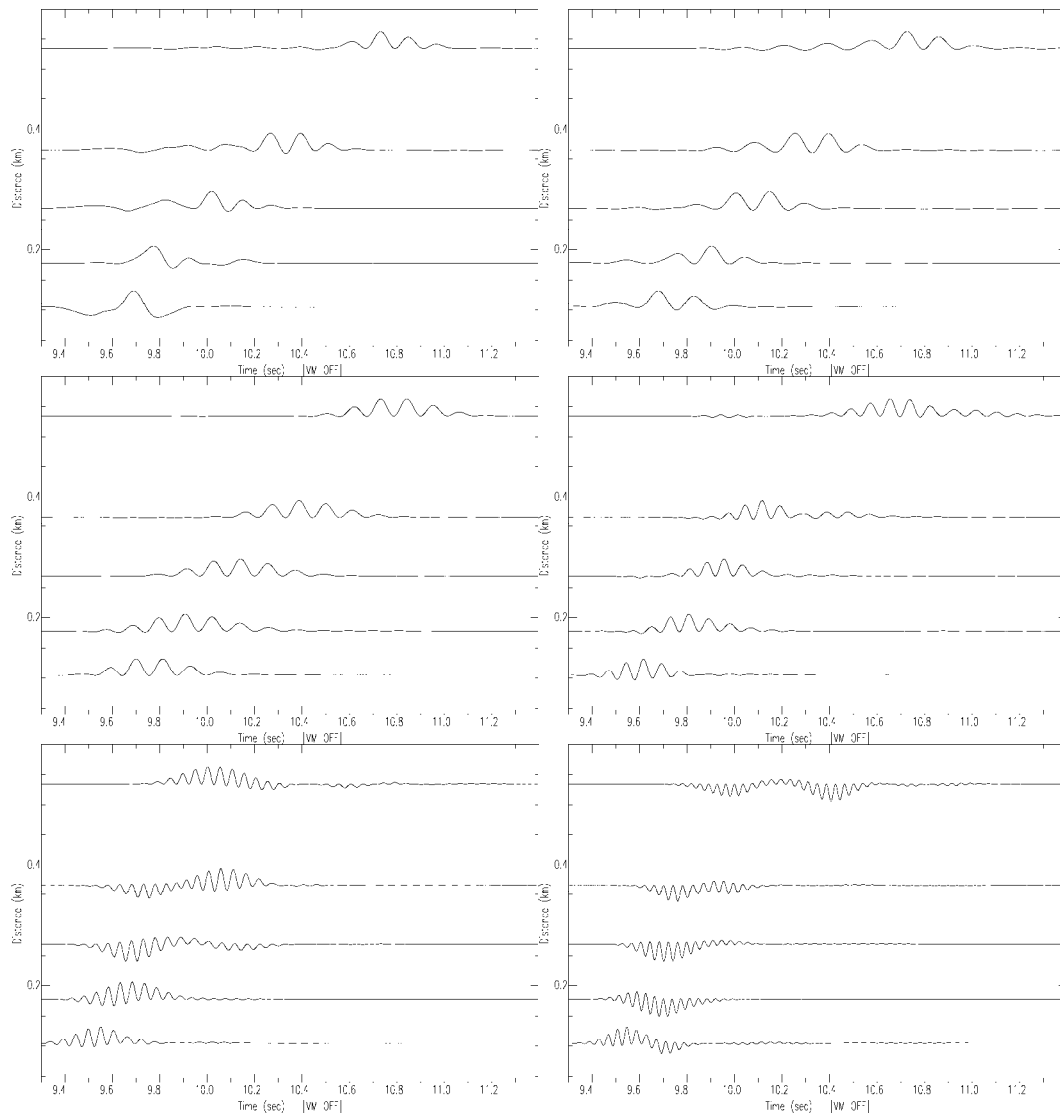


Figure 69. Product traces of the vertical and Hilbert transformed radial records of explosion 1 for stations south of the source, at 0.5 - 1.5, 1.5 - 3, 3 - 5, 5 - 8, 8 - 11, and 11 - 15 Hz from left to right and from the top down.

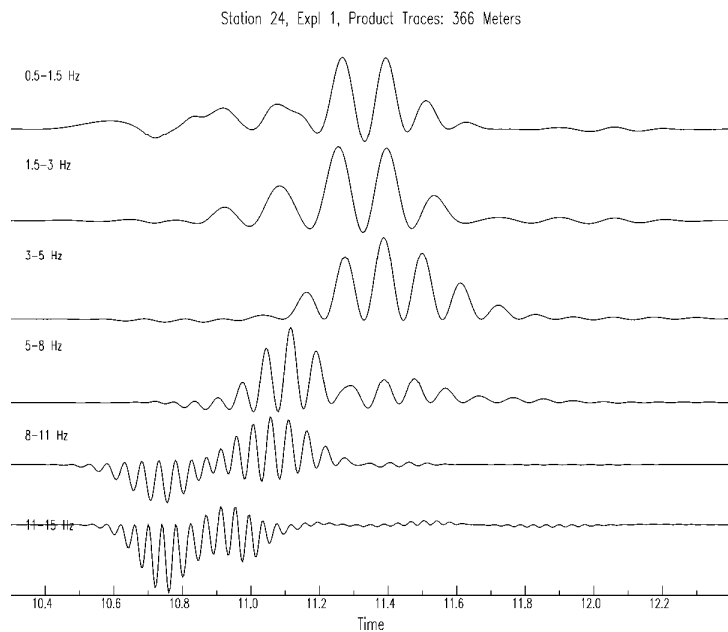


Figure 70. Product traces for explosion 1 at station 24, 366 meters from the source, in 6 passbands.

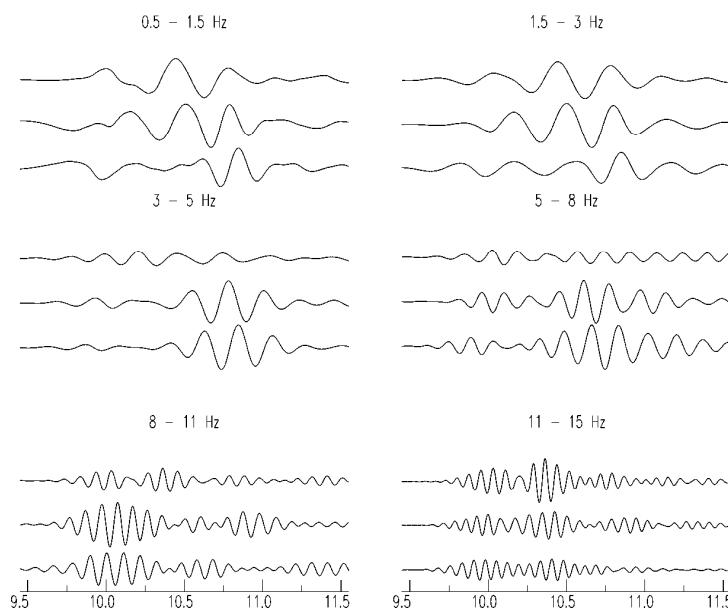


Figure 71. Three component records of explosion 1 at station 25 (534 m) in 6 passbands. All components in each passband are plotted on the same scale.

We use these results to confirm the identification of shear waves in individual records, so we can compare P with S spectra, and compare waveforms between events in various passbands, with some confidence in the phase identification.

7.3 Analysis of the P and S waves: P, SV, and SH spectra

Using the known P and S velocities from Gitterman et al. (2007b), we select P and S windows. We confirm those by comparison with the phases in the record sections of the previous section and by examining the particle motion of both windows. Figure 72 (upper left) shows the S (blue) and P (red) windows on the tangential and vertical seismograms of explosion two recorded at station 15. We compare the tangential S to vertical P spectra (upper right) because those components provide the least contamination of S by P, and of P by S energy respectively. The P particle motion is linearly polarized in the vertical-radial plane (lower left), confirming the lack of S-wave energy in the window. The S particle motion starts out briefly on the tangential component (the first 0.05 seconds are plotted in red), but thereafter tangential and radial particle motions are comparable (lower right). The S and P spectra are dissimilar, with a large P null at 50-60 Hz not mirrored in the S spectra, which has a null around 80 Hz (upper right).

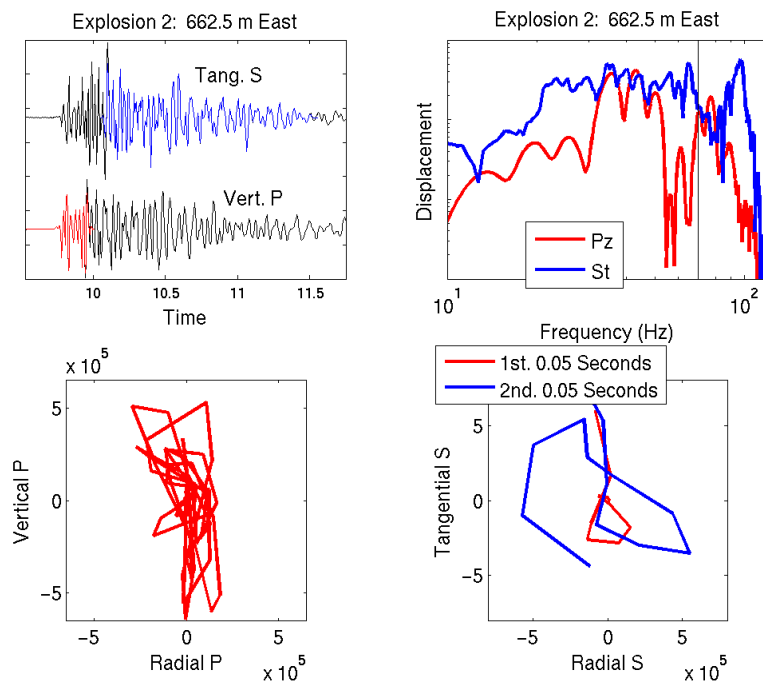


Figure 72. Upper left plot shows vertical P (red, lower trace) and tangential S (blue, upper trace) seismograms at the most distant station, 15. Corresponding spectra are shown in the upper right. The P-wave particle motion in the vertical-radial plane is linear and vertically oriented (lower left). The S particle motion in the tangential-radial plane begins tangentially polarized and quickly becomes circular.

Before we compare the vertical P with the tangential S spectra at other stations and for the other explosions, we recall that there were some differences between tangential and radial S waveforms (e.g. Figure 65), which pose the question of whether the SH and SV share the same generation mechanism. To address that, we compare spectra of radial with tangential S. For explosion 2 at three of the four most distant stations, the SH and SV spectra are very similar (Figure 73). At just one station, station 25, peaks and nulls occur at different frequencies (Figure 73, upper left). That SH and SV spectra are more commonly similar proves nothing about the

source, except that SV and SH source spectral differences or radiation patterns do not dominate the seismograms. The observations at station 25 may be due to scattering along the path.

Figure 74 shows the SV and SH spectra of the other explosions at station 15, the most distant station. They are also similar, and most strikingly, they are similar to each other and to the SV and SH spectra of explosion 2 at station 15 (Figure 73, bottom left) with peaks at 60-70 Hz and nulls at 80-90 Hz, indicating that the spectral shapes there are most likely controlled by the local structure, rather than the sources.

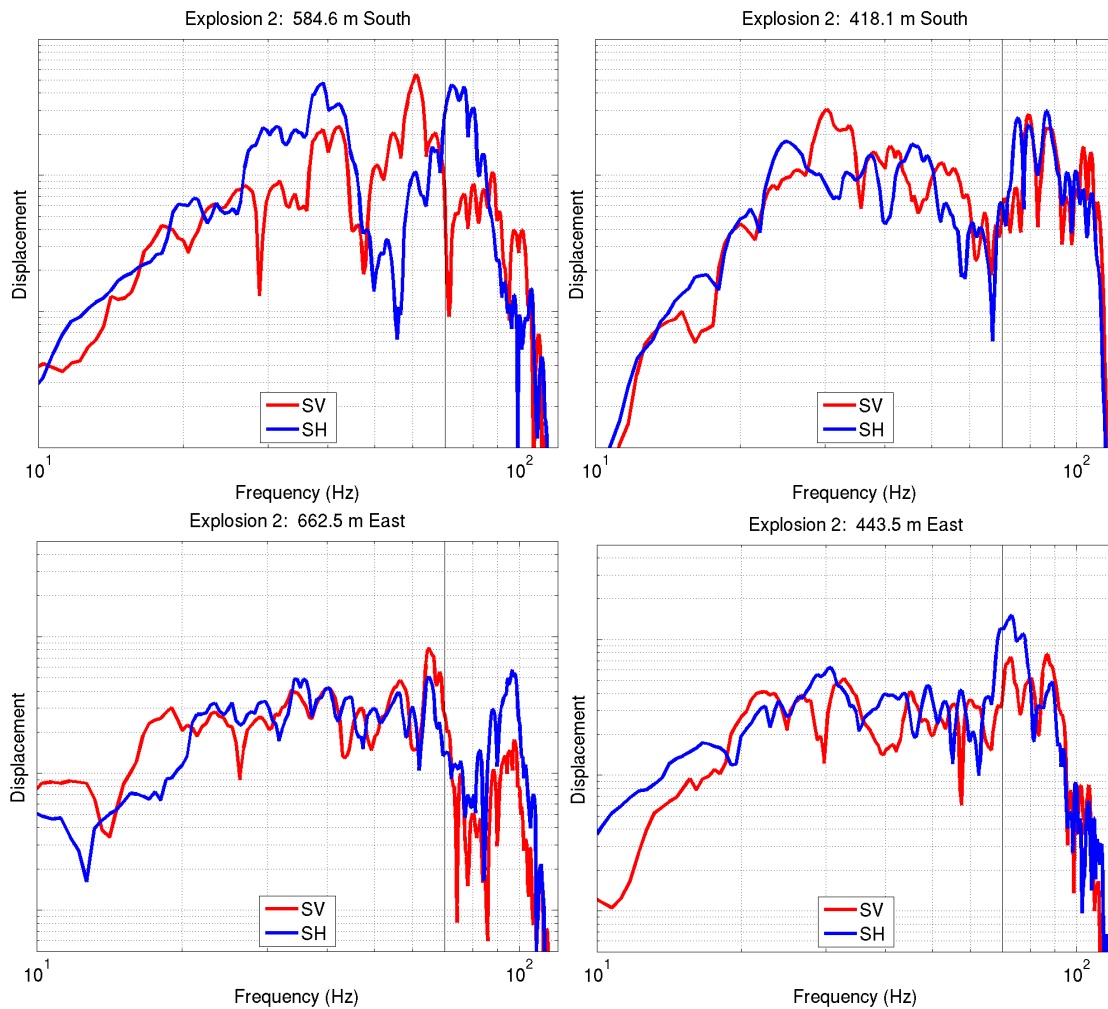


Figure 73. SV and SH spectra of explosion 2, recorded at four stations.

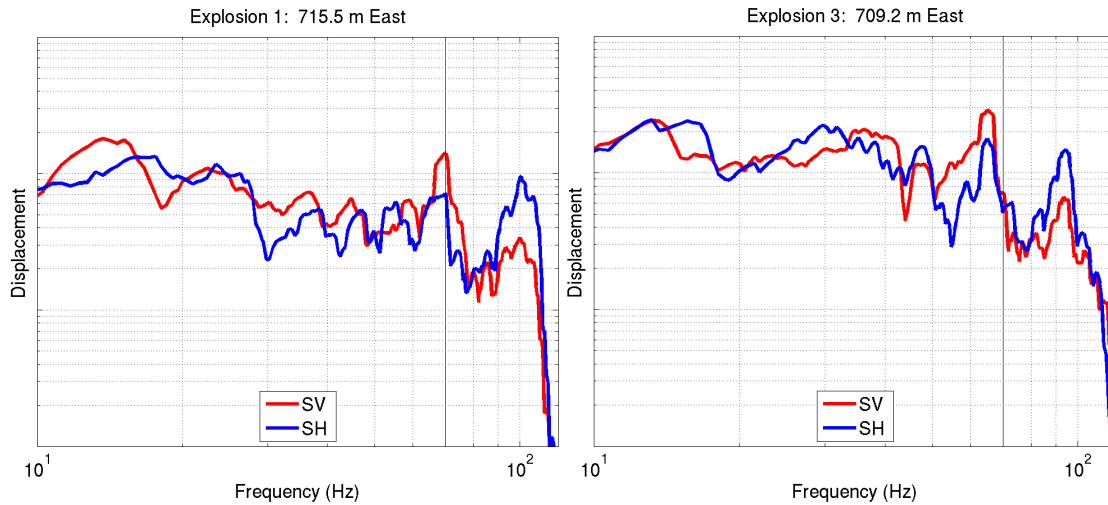


Figure 74. SV and SH spectra of explosions 1 (left) and 3 (right), recorded at station 15.

Figure 75 has similar plots to Figure 72 for each explosion, except that in the bottom right of each set it shows the S-to-P spectral ratio, which proves to be useful in identifying why the S and P spectra differ. Each explosion's record has a null in the P spectra and 60 Hz, and an S null at 80 Hz. We don't expect identical source spectra given the different depths, scaled depths, and extent of decoupling of the explosions, and indeed the spectra do differ between explosions (e.g. Figure 57). The similarity of S-to-P spectral shapes of all three events however indicates that the biggest differences we observe between the S and P spectra are controlled by structure rather than sources.

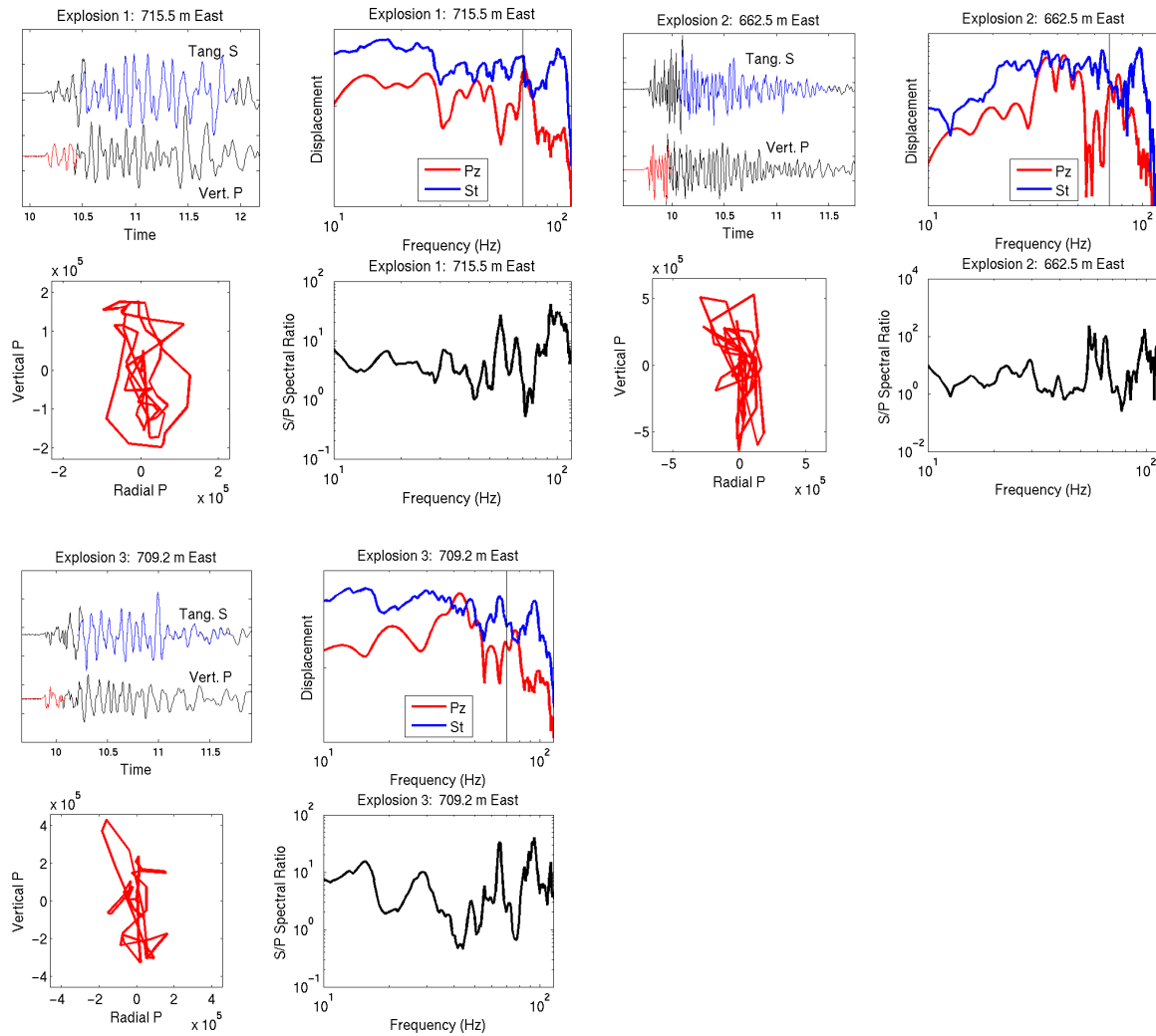


Figure 75. Plots for each explosion at station 15, similar to Figure 72 except that the bottom right plot of each set shows the S-to-P spectra ratio.

Let us summarize the observations thus far. The most significant spectral difference between the events is the greater amplitude at higher frequencies of the most decoupled explosion. This higher frequency energy, is likely due to both the greater decoupling reducing the RVP relative to the tamped explosion and differences in the excitation of modes by the deeper explosion. Particle traces based on the Hilbert transformed radial and the vertical component proved to be an effective means of separating local S and P records that overlap in time, based on their particle motion, and we use them to help identify shear waves in record sections of the Israeli explosions. Having identified the shear waves, we have found that the largest peaks and nulls of their local P and S spectra, which are between 60 and 100 Hz, are controlled by local structure rather than by the source spectra. We next focus on somewhat lower frequencies, and examine the waveforms in different passbands.

7.4 Analysis of the P and S waves: Comparison of waveforms

Figure 76 shows overlain explosion 3 (solid) and explosion 1 (dashed) vertical component records from station 11 in different passbands. The records are integrated to velocity from the accelerograms. The waveforms are very similar, with a slight decrease in amplitude for the partially decoupled explosion up to 30 Hz. Above 30 Hz however, there is a large arrival only from the decoupled explosion, at approximately 0.2 seconds after P. The station is 145.4 and 163.2 m respectively from the two sources.

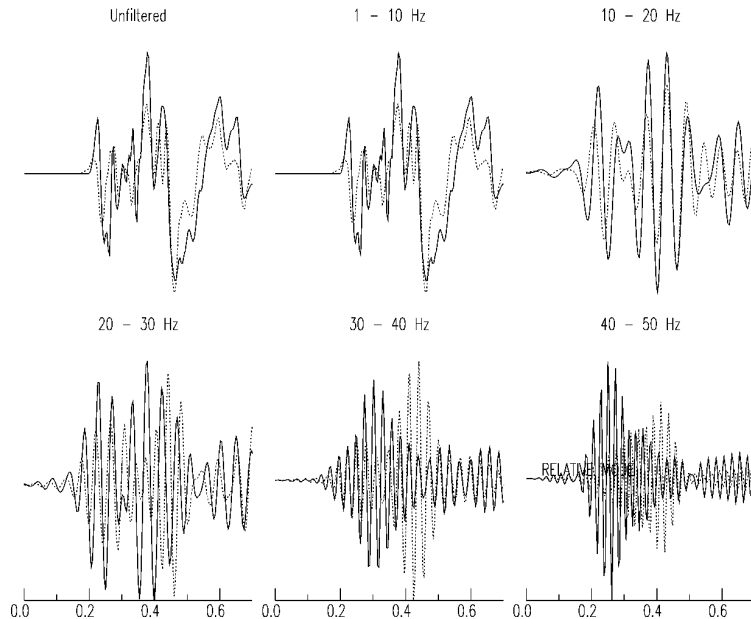


Figure 76. Vertical component records of the tamped (solid) explosion and the shallower partially decoupled explosion, at 145.4 and 163.2 m respectively. Initial P arrivals are aligned at 0.2 seconds.

Figure 77 shows records from the same two events at just over 700 m. Again, the records are similar at lower frequencies, with slightly smaller amplitudes for the partially decoupled explosion. At 20 to 30 Hz the initial P is smaller for the partially decoupled explosion, but later phases are closer in amplitude. The coda amplitudes are almost identical in amplitude. This indicates that the coda is not scattered from earlier phases, but is dominated by shallow higher mode surface waves generated at the source. The same observation is made at 30 to 40 Hz. There, the amplitudes are much smaller for the decoupled explosion until 0.4 to 0.5 seconds after P. This is unlikely to be related to cavity resonance, which should be at a much higher frequency and should affect P as well.

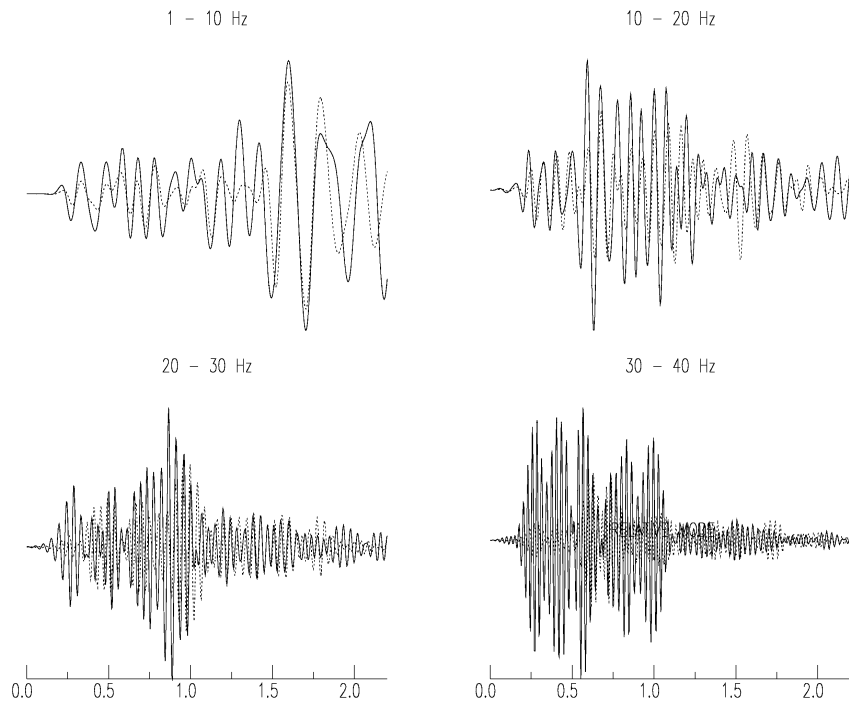


Figure 77. Vertical component records of the tamped (solid) and partially decoupled explosion at station 15, 709.2 and 715.5 m distance respectively. Initial P arrivals at aligned at 0.2 seconds.

We use both velocity and particle motion to identify the phases. In simple records, local Sg is often identifiable as higher mode Rg by its retrograde particle motion. To identify such motion, we overlay vertical and Hilbert transformed radial records (Figure 78, lower sets of traces) for the tamped (left) and partially decoupled (right) explosions, filtered from 30 to 40 Hz. Those records for the shallower partially decoupled explosion are out of synch for the P-wave, and abruptly come into synch at approximately 0.3 seconds, so 0.1 seconds after P. This is consistent with the predicted S-P time of approximately 0.09 seconds, given the distances and the velocities reported in Gitterman et al. (2007b), that is, $V_p=1.71$ to 1.82 km/s and $V_s=0.87$ km/s. The vertical and Hilbert transformed radial are close, but a bit out of synch during the large arrival that is only present in the partially decoupled explosion record. The coda following is perfectly in synch. The tamped explosion records are never quite in synch. They are closest during the large arrival, beginning to align at just 0.05 seconds into the record, and are the most in synch from 0.35 to 0.45 seconds, the same time as the large later possible S-wave from the partially decoupled explosion. This suggests that a secondary S phase may be generated by both sources, but is larger from the partially decoupled explosion. Note that the filtering is acausal, with initial P on the unfiltered records set at 0.2 seconds, but the filtered record also beginning ~ 0.05 seconds earlier, so precise timing is difficult to determine. The coda of the tamped explosion does not have retrograde particle motion, in contrast to that of the partially decoupled explosion coda. This supports our earlier identification of the larger coda of the decoupled explosion as very shallow, so slow, surface waves coming from the source, rather than as scattered P-waves.

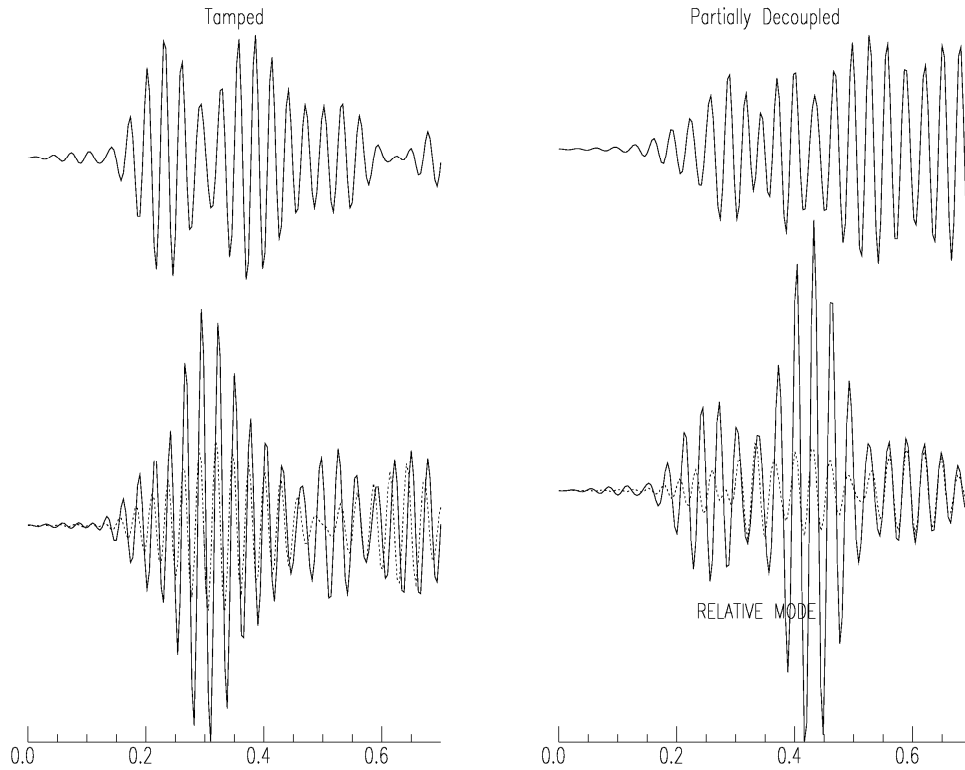


Figure 78. Tangential (upper traces) and overlain vertical (solid) and Hilbert transformed radial (dashed) records (lower traces) at station 11, 145.4 and 163.2 m distance respectively from the tamped (left column) and partially decoupled (right column) explosions. Initial P arrivals are aligned at 0.2 seconds.

Figure 79 is similar to Figure 78, but for the more distant station 15 (same records as Figure 77). The predicted S-P time for these data is approximately 0.35 seconds, which is when the vertical and Hilbert transformed radial records for both events align, again indicating a shear wave. There is a large tangential component arrival at the same time. After that time, the alignment is erratic. From 0.8 to 1.0 seconds, the partially decoupled explosion's traces align. Again, alignment is less consistent and the phase is smaller for the tamped explosion. Also, the particle motion of the partially decoupled explosion's coda is again retrograde, but the tamped explosion's coda is not.

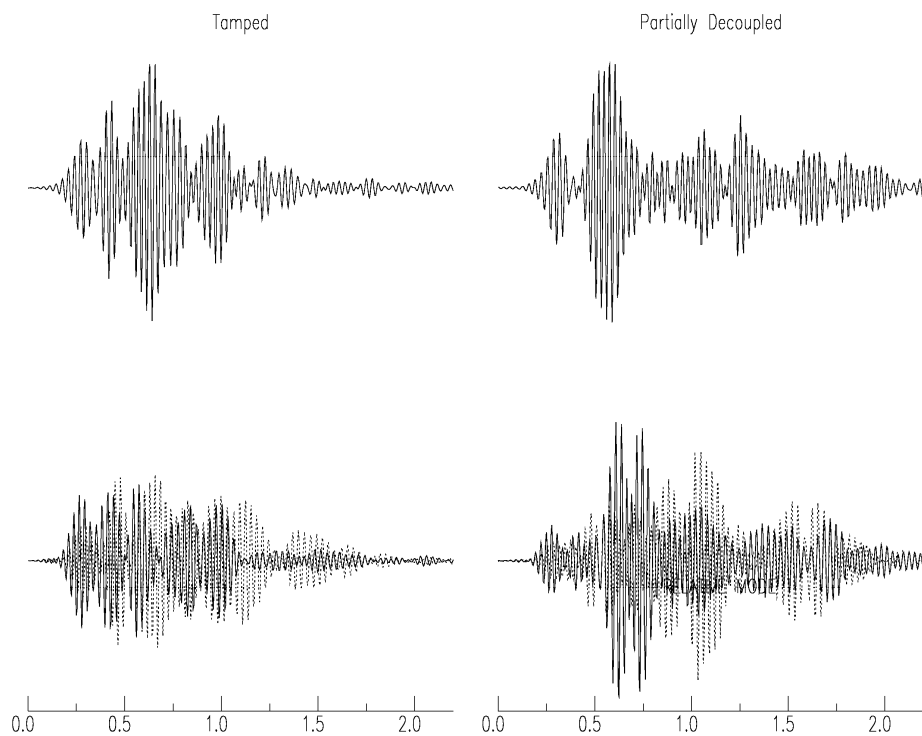


Figure 79. Tangential (upper traces) and overlain vertical (solid) and Hilbert transformed radial (dashed) records (lower traces) at station 15, 709.2 and 715.5 m distance respectively from the tamped (left column) and partially decoupled (right column) explosions. Initial P arrivals are aligned at 0.2 seconds.

Our hypothesis is that the large later arrival is an S phase generated at the source by the decoupled, but not the tamped explosion. That would also explain the much larger coda (relative to P) of shallow, slow mode arrivals from the decoupled explosion. An alternate explanation is that 30-40 Hz is below the P corner of both events, and above the S corner of the tamped, but not the decoupled explosion. The spectral observations, while complex and difficult to unambiguously interpret, do not appear to support that hypothesis. Figure 80 shows the tangential S to vertical P ratios of each event from 10 to 50 Hz. There is no clear drop like that predicted by the Mueller-Murphy source, assuming that the S spectra scales as the ratio of the S-to-P source velocities. Similarly, the ratio of S-to-P ratios from the decoupled events to the tamped (Figure 81, upper right and lower left), and the more decoupled to the less decoupled (lower right) do not resemble the predictions. The prediction for the most decoupled to the tamped explosions' S-to-P ratios is shown on the upper left. We do not draw conclusions from details of these observations, except that the spectra do not support a simple explanation of relative S-to-P corner frequencies as the explanation for the additional S-phase observed at 30 to 40 Hz.

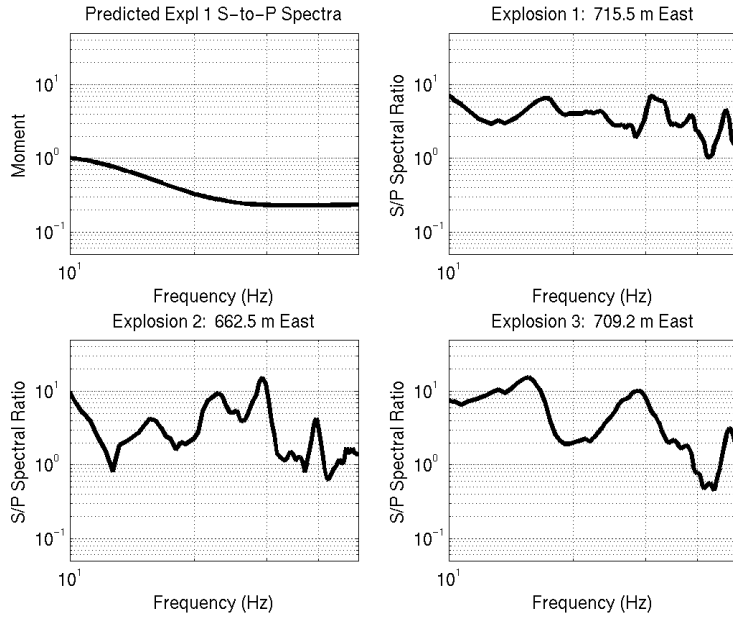


Figure 80. S-to-P ratios (tangential S to vertical P) predicted for the explosion 1 Mueller-Murphy source (upper left) and for each explosion, from 10 to 50 Hz.

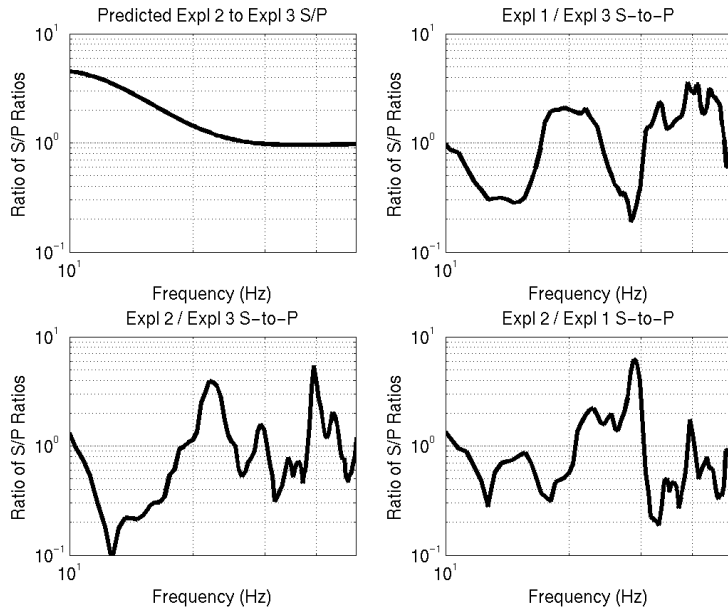


Figure 81. Relative S-to-P spectral ratios of one event to the next. Upper left is the Mueller-Murphy prediction for the explosion 2 to explosion 3 S-to-P ratios.

These observations suggest that higher mode S-waves are more strongly excited by the partially decoupled than by the tamped explosion. Although the sources are quite close, and the path is very similar, the difference could be due to structure. The partially decoupled explosion is 3.5 meters shallower, and the sediments thicker (the transition from alluvium to chalky marl is at 6.5 m above the partially decoupled explosion source, and is at 4.5 m above the tamped explosion. To address this, we next make similar observations of the more fully decoupled explosion 3. As it was detonated at 63 m depth, in a slightly higher velocity phosphate marl, it is

more difficult to separate the depth and source material effects on the waveforms from the effects of decoupling, but consistent observations from the two partially decoupled explosions would indicate that they are due to the decoupling, not structure.

Figure 82 shows the overlain vertical component records of explosion 2 (the deeper decoupled explosion, dashed) and explosion 3 (the tamped explosion, solid) at 320.7 and 295 m respectively (stations 23 and 22 respectively). The greater decoupling at low frequency of explosion 2 is evident, as is its greater amplitude at high frequency. The important observation however is that while the P-waves of the two events are approximately the same amplitude at 30 to 40 Hz, a secondary phase at approximately 0.4 seconds after P has increased even more in amplitude. By 40 to 50 Hz, while the P-waves are still comparable, at 0.6 seconds the decoupled explosion record is much larger than that of the tamped explosion. Also, at .15-.2 seconds after P, the predicted initial S minus P time, the decoupled explosion record is much larger. The observations at 478 and 444 m are similar (Figure 83).

Figure 84 shows all three components of the records in Figure 82. The lower traces are the overlain vertical and Hilbert transformed radial. The decoupled explosion records align beginning at 0.15 to 0.2 seconds, identifying a higher mode Rg arrival.

The most striking observations from this comparison of waveforms are that 1) both decoupled explosions, despite differences in depth and source media, have additional S-waves relative to P at 30 to 40 Hz, and 2) the decoupled explosions' coda, which can be identified as shallow surface wave modes, also increases relative to P, as compared with that of the tamped explosion. Both observations point to the decoupled explosion sources generating more shear waves relative to compressional waves at these higher frequencies than the tamped explosion.

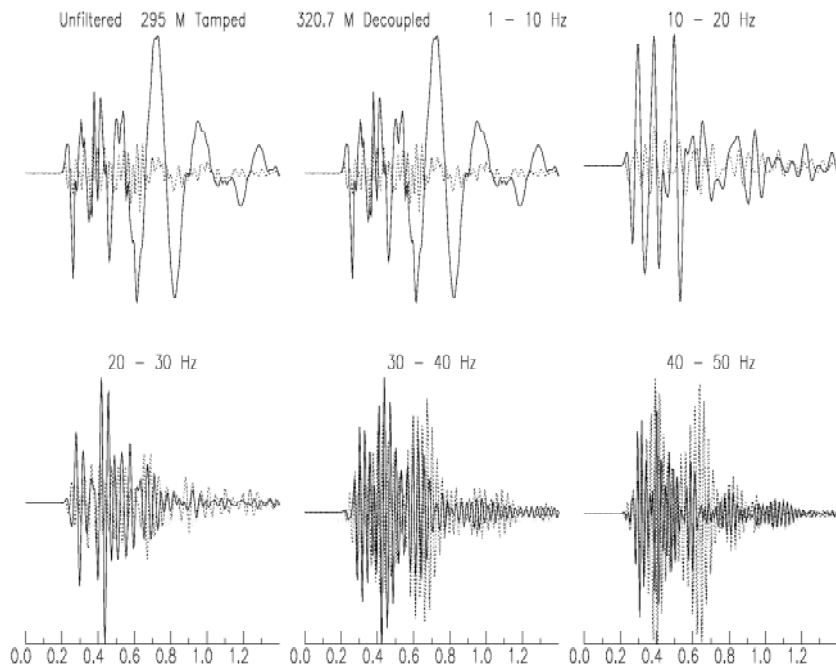


Figure 82. Vertical component records of the tamped (solid) explosion and the deeper partially decoupled explosion, at 295 and 320.7 m respectively. Initial P arrivals are aligned at 0.2 seconds.

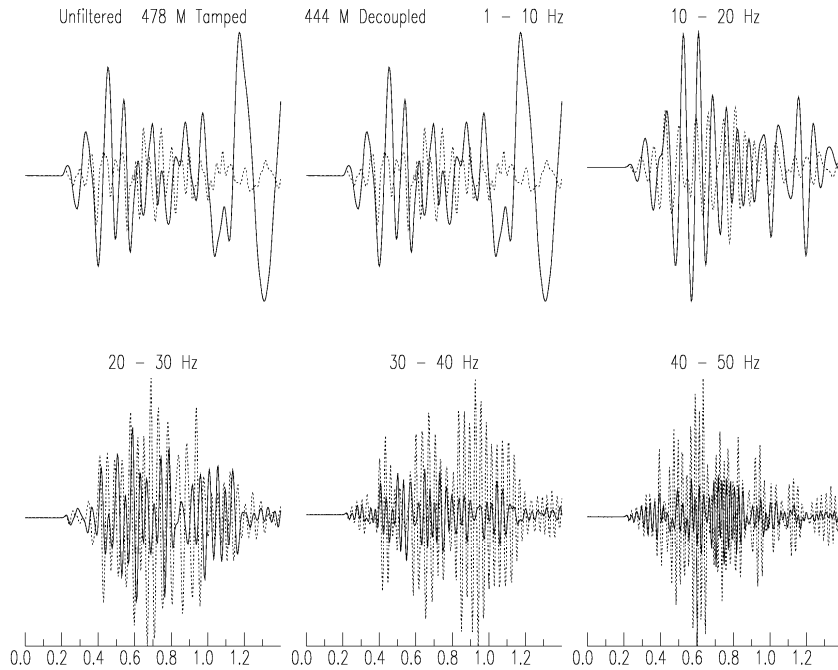


Figure 83. Vertical component records of the tamped (solid) explosion and the deeper partially decoupled explosion, at 478.1 and 443.5 m respectively. Initial P arrivals are aligned at 0.2 seconds.

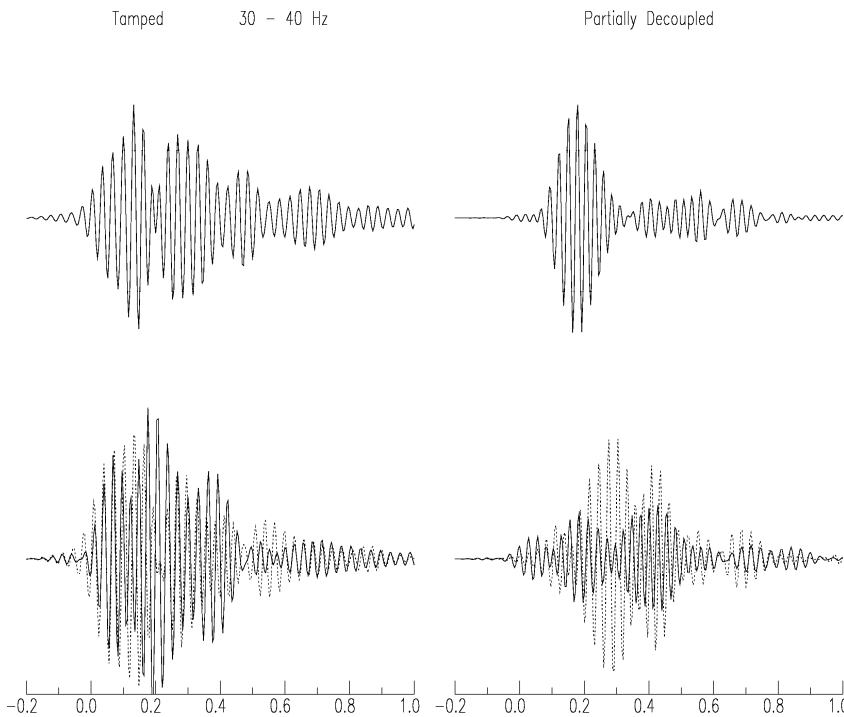


Figure 84. Tangential (upper traces) and overlain vertical (solid) and Hilbert transformed radial (dashed) records (lower traces) at 295 and 320.7 m distance respectively from the tamped explosion 1 (left column) and the deeper partially decoupled explosion 2 (right column) explosions. Initial P arrivals are at aligned at 0.0 seconds.

7.5 Waveform Modeling

Calibration of the records: Absolute amplitudes

While it is useful to just compare waveforms without consideration of matching absolute amplitudes, we may learn more if we compare predictions with the absolute amplitudes measured. To do so, we must first digress and describe how the absolute amplitudes are determined. The data are available in evt format. We converted them to SAC format using the K2SAC routine available from Kinematics via their website. The resulting SAC files are in counts. SAC header lists the sensor as an EpiSensor with default parameters. At least up to 50 Hz the response is flat, although the phase response is not (Figure 85). The amplitude response is nearly flat to 50 Hz and drops by ~ 0.3 dB at 100 Hz, so $20\log(A_1/A_0) = -0.3$, or the amplitude drops to $10^{(-.3/20)} = 97\%$ of the original amplitude. For our purposes, we can assume it's flat.

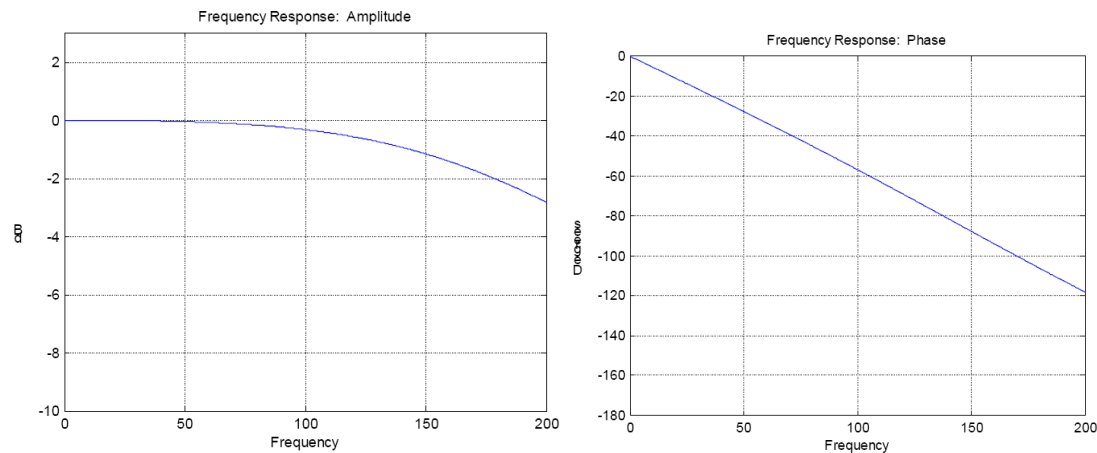


Figure 85. Amplitude and phase response of the episensor, to acceleration, from the EpiSensor's user's manual. Y axes are dB and degrees.

We used the Kinematics program SMA to read the binary (and otherwise inaccessible) header information, plot the data in units of cm/sec^2 , and zoom in to find the peak amplitude. Comparison with counts in SAC allows us to empirically estimate the conversion from counts to cm/sec^2 . At station 25 for example, we find the same conversion for all three events. The conversion is essentially identical to that for station 15. The gain appears to be different at station 11, although it is again consistent from event to event.

Vertical component amplitudes for each event at station 25 (after demeaning)

	Event 1	Event 2	Event 3
SAC counts	9.726409e+05	2.137831e+06	1.346694e+06
SMA cm/sec^2	28.43	62.49	39.36
$\text{cm}/\text{sec}^2/\text{count}$	2.923e-5	2.923e-5	2.923e-5

Vertical component amplitudes for each event at station 15 (after demeaning)

	Event 1 (715.5 m)	Event 2 (662.5 m)	Event 3 (709.2 m)
SAC counts	7.217126e+05	7.347594e+05	8.574782e+05
SMA cm/sec^2	21.128	21.5086	25.101
$\text{cm}/\text{sec}^2/\text{count}$	2.9275e-5	2.9273e-5	2.9273e-5

Vertical component amplitudes for each event at station 11 (after demeaning)

	Event 1 (163.2 m)	Event 2 (96.1 m)	Event 3 (145.4 m)
SAC counts	1.470100e+06	8.328372e+06	2.619365e+06
SMA cm/sec ²	343.72	1947.246	612.43
cm/sec ² /count	2.3381e-04	2.3381e-04	2.3381e-04

To compare seismograms from station 15, for example, with synthetics we first multiply the counts by $2.9274e-7$ to obtain m/s^2 , and correct the observation amplitudes to 710 m. That is, we make a $1/r$ amplitude correction to the actual data for distance to 710 m (explosions 1 through 3 are 715.5, 662.5, and 709. m respectively from station 15).

We calculate wavenumber (PROSE) synthetics at 710 m. The output of PROSE represents displacement for a delta function source with a moment of one Nt-m. We scale them with a predicted moment rate spectra of the source, which is intended to convert the synthetics to velocity with realistic source spectra. We have used both the Mueller-Murphy source and the RVP determined from numerical calculations.

Comparison of Synthetics with Tamped Explosion Records

Figure 86 shows Prose velocity synthetics at 710 meters for a point spherical explosion source and data from the tamped explosion recorded at 710 meters. The synthetics are calculated for the models of Figure 58 and are scaled by the Mueller-Murphy source spectrum. As we don't know the material properties, we used those of tuff, which will be somewhat inaccurate. Also, the model is not appropriate for such shallow depths. To match P amplitudes at 5 to 15 Hz, we had to reduce the scaled synthetics' amplitudes by a factor of three, which is quite close under the circumstances. The data are integrated to velocity.

The important result here is that the S to P amplitude ratios at 5 to 10 and at 10 to 15 Hz, are consistent with those of the synthetics. That is, a spherical explosion source produces the shear waves observed relative to P, so there is no need of an additional S-wave source (e.g. a CLVD). The S is most likely due to a combination of pS, given the very low near surface velocity in which the explosion was detonated, and S*, given the shallow source depth. Discrepancies between synthetics and data are a result of shortcomings of the simple modeling. The large fundamental mode Rg seen in the synthetics at 5 to 10 Hz is not observed in the data. It is common in modeling that Rg is larger in synthetics. The late arriving energy (at ~1 second) in the data at 20 to 30 Hz is likely higher mode energy that, at such high frequency, has very shallow eigenfunctions. That is, the energy is likely trapped in a very shallow surface layer that is not accurately modeled.

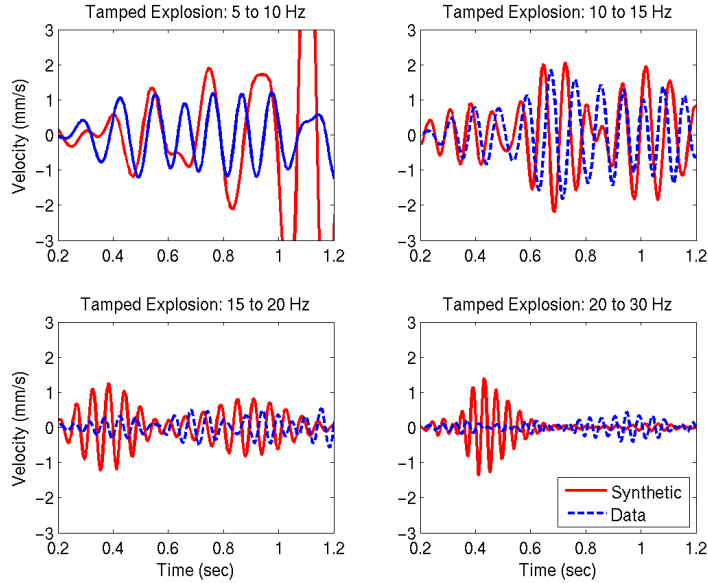


Figure 86. Synthetic (red) and actual records (blue) of the tamped explosion at 710 meters in 4 passbands.

Results are similar for the decoupled explosions. Figure 87 is similar to Figure 86, but for explosion 1. The Muller-Murphy source used to scale the synthetics was based on a depth of 26.5 meters, and the yield was reduced by a factor of 2.8, the decoupling factor found by Gitterman et al. (2007). The synthetics were again reduced by a factor of 3, for consistency with the processing of the tamped explosion synthetics. Results are very similar to those for the tamped explosion (Figure 86). The P and S amplitudes match the synthetics below 15 Hz, but the synthetic Rg is larger than predicted. The observed P-wave amplitude drops dramatically relative to the synthetics at higher frequency.

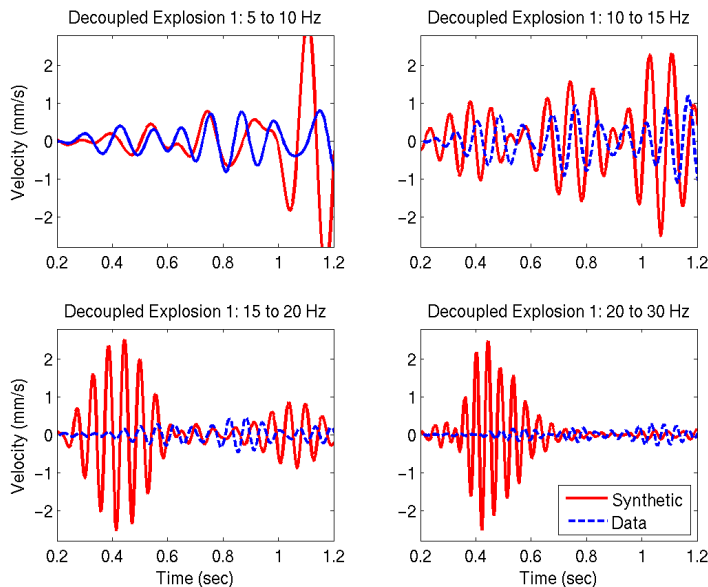


Figure 87. Synthetic (red) and actual records (blue) of the deeper, more decoupled explosion 1 at 710 meters in 4 passbands.

Figure 88 is similar to Figure 86 and Figure 87, but for explosion 2. The Muller-Murphy source used to scale the synthetics was calculated for 63 meters depth, the yield was reduced by a factor of 6.4, the decoupling factor found by Gitterman et al. (2007b), and the synthetics were reduced by a factor of 3. The fit of the S and P waves at 10 to 15 Hz to the synthetics verifies that the decoupling factor determined from regional data is consistent to that observed locally. For this deeper event, the predicted Rg is not greater than the observed. Again the observed P amplitudes drop dramatically relative the predictions above 15 Hz. For both the shallower tamped and the less decoupled event, the observed S amplitudes dropped significantly. For this event, the observed S-waves are much larger than the predictions above 15 Hz, suggesting that while no secondary source is necessary below 15 Hz, the data would be better fit with a CLVD at high frequency.

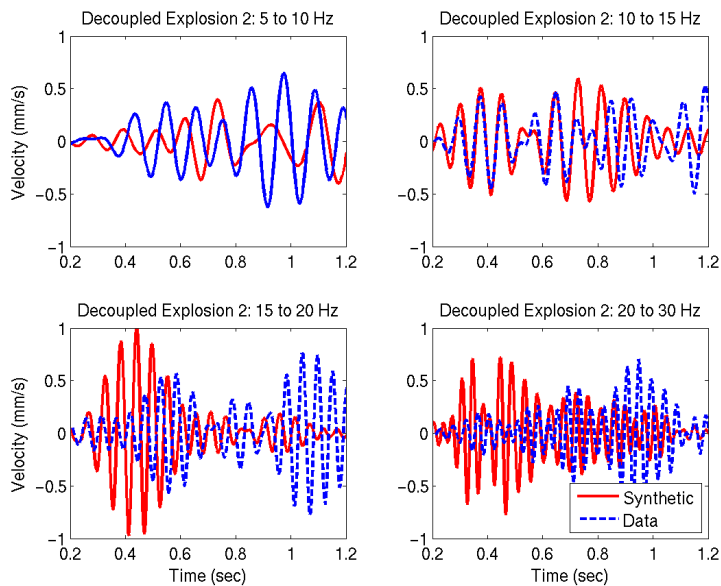


Figure 88. Synthetic (red) and actual records (blue) of the deeper, more decoupled explosion 2 at 710 meters in 4 passbands.

7.6 Conclusions

Below 15 Hz, the shear waves observed from all three explosions can be modeled accurately with a point spherical explosion source. Above 15 Hz, the increased S-to-P ratio of all three explosions would require a secondary S-wave source to match observations. That is most strongly the case for the deepest decoupled explosion, but that does not necessarily mean that additional CLVD, spall, or reverberation sources of S are required to match observations from that event. The deeper explosion has much more high frequency energy than the other explosions. This could be explained in part by the depth and yield dependence of the RVP, but can also be explained by the depth dependence of modal excitation. The actual source will be extended, and so will be quite near a structural boundary, which will lead to much greater excitation of higher modes for that event. At 30 to 50 Hz, both partially decoupled explosions have relatively more S-to-P energy, indicating that there is an additional S source at those frequencies that is absent from the tamped explosion source.

8. CONCLUSIONS

We have completed a detailed study of shear wave generation by decoupled explosions using essentially all of the data that is available from such events, including data from water-filled cavity experiments. We conclude that shear waves from decoupled explosions are generated primarily by asymmetries in the interaction between the shockwave or cavity reverberations and the cavity wall. There are of course other shear waves generated by phase conversion, but in all the cases we studied shear waves existed that were clearly source generated. We modeled these explosions using axisymmetric Eulerian and Lagrangian numerical simulations that included the effects of gravity, nonlinear material deformation, variable placement of the explosion within the cavity and cavity shape. We find the following sources for shear wave generation:

1. Interaction between the explosion shock and cavity walls. In the case of Sterling, we are able to match the early time part of near-field records very well using this mechanism alone.
2. Nonlinear deformation outside the cavity. This type of source can be modeled as an explosion plus a CLVD, with the asymmetry caused by any combination of gravity (variation of overburden pressure with depth), source offset from the cavity center, and cavity shape that result in asymmetric nonlinear deformation. We find that this explains part of the shear wave generation for partially coupled explosions, but is insufficient to generate all the shear waves observed, particularly for smaller, nearly fully decoupled explosions.
3. Long duration cavity reverberations, in particular vertically oriented reverberations between the top and bottom of the cavity. This type of source has the form of a dipole and corresponds to the whole cavity moving up and down. It must go to zero in the long period limit, but may persist for some time, and was clearly observable in Sterling near field data. This source has the radiation pattern of a vertical point force, and we found that a sum of CLVD and point source waveforms better explained the water-filled cavity data, with the point source becoming a larger part of the source for smaller events.

To the best of our knowledge, #3 above has not been suggested previously as a source mechanism for shear waves from decoupled explosions, and it appears to be quite important. It is possible that a similar effect occurs for tamped explosions. Although tamped explosions do not in general have internal cavity reverberations, asymmetries in the medium surrounding the explosion can lead to a similar dipole motion, which again must vanish in the long period limit, but could be important at frequencies important to nuclear monitoring.

9. REFERENCES

- Baker, G. E., H. Xu, and J. L. Stevens (2009), Generation of Shear Waves from Explosions in Water-Filled Cavities, submitted to *Bull. Seism. Soc. Am*
- Ben-Menahem, A. and J. Singh, Eigenvector expansions of Green's Dyads with applications to geophysical theory (1968), *Geophys. J. R. Astr. Soc.*, **52**, 65-96.
- Brune, J. N. and P. W. Pomeroy (1963), Surface wave radiation patterns for underground nuclear explosions and small-magnitude earthquakes, *J. Geophys. Res.*, **68**, 5005-5028
- Brune, J. (1970), Tectonic Stress and the Spectra of Seismic Shear Waves from Earthquakes, *J. Geophys. Res.*, **75**, 4997-5009
- Colella, P. and P. R. Woodward (1984), The Piecewise Parabolic Method (PPM) for Gas-Dynamical Simulations, *Journal of Computational Physics*, **54**, 174-201.
- Denny, M. D and Dennis M. Goodman (1990), A case study of the seismic source function: Salmon and Sterling reevaluated, *J. Geophys. Res.*, **95**, 19705-19723.
- Denny M.D. and L R Johnson (1991), The explosion seismic source function: models and scaling reviewed, *AGU Geophysical Monograph 65: Explosion Source Phenomenology*, S.R. Taylor, H. J. Patton and P. G. Richards (Eds)
- Fisk, M. D. (2006). Source Spectral Modeling of Regional P/S Discriminants at Nuclear Test Sites in China and the Former Soviet Union, *Bull. Seis. Soc. Am.*, **96**, 2348–2367
- Fisk, M. (2007), Corner frequency scaling of regional seismic phases for underground nuclear explosions at the Nevada test site, *Bull. Seismol. Soc. Am.*, **97**, 977-988
- Gitterman, Y., R. Hofstetter, and V. Pinsky (2007a), Depth-Of-Burial And Decoupling Explosion Experiments In Israel: Near-Source And Near-Regional Seismic Energy Generation, Proceedings of the 29th Annual Monitoring Research Review
- Gitterman, Y., V. Pinsky, and R. Hofstetter (2007b), Seismic energy generation and partitioning into various regional phases from different seismic sources in the Middle East region, Final Report to AFRL for contract AFRL-VS-HA-TR-2007-0000
- Glenn, L. A. and M. D. Denny (1987), Sterling revisited: the seismic source for a cavity-decoupled explosion, *Geophys. Res. Lett.*, **14**, 1103-1106
- Glenn, L., and P. Goldstein (1994), Seismic decoupling with chemical and nuclear explosions in salt, *J. Geophys. Res.*, **99** (B6), 11723-11730
- Gupta, I.N. and C. Kisslinger (1964), Model study of seismic waves from explosions in rectangular cavities, *Bull. Seismol. Soc. Am.*, **54**, 1105-1113
- Gupta, I.N. and K. L McLaughlin (1989), Strain and frequency-dependent attenuation estimates in salt based on Salmon and Sterling near-field recordings, *Bull. Seismol. Soc. Am.*, **79**, 1111-1112

- Healy, J. H., C-Y King, and M.E. O'Neill (1971), Source parameters of the Salmon and Sterling nuclear explosions from seismic measurements, *J. Geophys. Res.*, **76**, 3344-3355
- Heard, H. C, A. E. Abey, B. P. Bonner and A. Duba (1975), Stress-strain behavior of polycrystalline NaCl to 3.2GPa, Lawrence Livermore Laboratory report, UCRL-51743
- Langston, C. A. (1983), Kinematic analysis of strong motion P and SV waves from the Sterling event, *J. Geophys. Res.*, **88**, 3486-3497.
- Larson, D. B. (1982), Inelastic wave propagation in sodium chloride, *Bull. Seismol. Soc. Am.*, **72**, 2107-2130
- Latter, A. L., R. E. Lelevier, E. A. Martinelli, and W. G. McMillan (1961), A method of concealing underground nuclear explosions, *J. Geophys. Res.*, **66**, 2929
- Masse, R. P. (1981), Review of seismic source models for underground nuclear explosions, *Bull. Seismol. Soc. Am.*, **71**, 1249-1268
- McCator, G. D., and W. R. Wortman (1988), Nonlinear attenuation mechanisms in salt at moderate strain based on Salmon data, Rep.AFGL-TR-89-0013, Mission Res. Corp., Santa Barbara, Calif
- McCator, G. D., and W. R. Wortman (1990), Analysis of Nuclear Explosion Salmon Free-Field Ground Motion Data for Nonlinear Attenuation, *J. Geophys. Res.*, **95**(B13), 21,805–21,821
- Morse, P. M. and H. Feshbach (1953), *Methods of Theoretical Physics*, McGraw-Hill, New York
- Mueller, R. A. and J. R. Murphy (1971), Seismic Characteristics of Underground Nuclear Detonations, I: Seismic Spectrum Scaling, *Bull. Seism. Soc. Am.*, **61**, 1675-1692
- Murphy, J. (1969), Discussion of Paper by D. Springer, M. Denny, J. Healy, and W. Mickey, 'The Sterling Experiment: Decoupling of Seismic Waves by a Shot-Generated Cavity', *J. Geophys. Res.*, **74**(27), 6714-6718
- Murphy, J. R. (1977), Seismic source functions and magnitude determinations for underground nuclear detonations, *Bull. Seismol. Soc. Am.*, **67**, 135-158
- Murphy, J. R. (1991), Free-Field Seismic Observations from Underground Nuclear Explosions, 25-33, *AGU Geophysical Monograph 65: Explosion Source Phenomenology*, S. R. Taylor, H. J. Patton, P. G. Richards (Eds)
- Murphy, J. R. and B. W. Barker (1994), Seismic identification analysis of cavity decoupled nuclear and chemical explosions, SSS-TR-94-14399, S-cubed, Maxwell laboratories, Incorporated, La Jolla
- Murphy, J. R., I. Kitov, N. Rimer, D. Sultanov, and B. Barker (1995), Analysis of the Seismic Characteristics of U.S. and Russian Cavity Decoupled Explosions, *Final Report by Maxwell Labs Inc, to Phillips Lab., Air Force Systems Command*

- Murphy, J., N. Rimer and J. Stevens (1996), Comment on Seismic Decoupling with Chemical and Nuclear Explosions in Salt by L. Glenn and P. Goldstein, *J. Geophys. Res.* **101**, 845-850
- Murphy, J.R., I. O. Kitov, N. Rimer, V. V. Adushkin and B. W. Barker (1997), Seismic characteristics of cavity decoupled explosions in limestone: An analysis of Soviet high explosive test data, *J. Geophys. Res.*, **102**, 27,393-27,405
- Murphy, J. R., D. D. Sultanov, N. Rimer, and B. W. Barker (2001). Seismic source characteristics of nuclear explosions in water-filled cavities, *Pure Appl. Geophys.* **158**, 2,105–2,121.
- Nilson, R., N. Rimer and E. Halda (1991), Dynamic modeling of explosively driven hydrofractures, *J. Geophys. Res.*, **96**, 18081-18100
- Patterson, D. W. (1966), Nuclear coupling, full and partial, *J. Geophys. Res.*, **71**, 3427-3436
- Perret, W. R. (1968a), Shear waves from a nuclear explosion in a salt cavity, *Bull. Seismol. Soc. Am.*, **58**, 2043-2051
- Perret, W.R. (1968b), Free-field particle motion from a nuclear explosion in salt, part I, Final report VUF-3012, Sandia Laboratory
- Rawson, D.R, R.W. Taylor and D. L. Springer (1967), Review of the Salmon experiment: a nuclear explosion in salt, *Naturwissenschaften*, **54**, 525-531
- Rimer, N and J. T. Cherry (1982), Ground motion predictions for the Grand Saline experiments, S-CUBED VSC-TR-82-25
- Stevens, J. L. (1980), Seismic radiation from the sudden creation of a spherical cavity in an arbitrarily prestressed elastic medium, *Geophys. J. R. Astr. Soc.*, **61**, 303-328
- Stevens, J. L., J. R. Murphy, and N. Rimer (1991a), Seismic source characteristics of cavity decoupled explosions in salt and tuff, *Bull. Seism. Soc. Am.*, **81**, 1272-1291
- Stevens, J. L., N. Rimer, J. R. Murphy, T. G. Barker, E. Bailey, E. J. Halda, W. Proffer, S. H. Rogers, and B. Shkoller (1991b), Simulation of seismic signals from partially coupled nuclear explosions in spherical and ellipsoidal cavities, S-Cubed final report SSS-FR-91-12735, August
- Stevens, J. L, J. R. Murphy and N. Rimer (1991c), Seismic source characteristics of cavity decoupled explosions in salt and tuff, *Bull. Seismol. Soc. Am.*, **81**, 1272-1291
- Stevens, J. L., T. G. Barker, S. M. Day, K. L. McLaughlin, N. Rimer, and B. Shkoller (1991d), Simulation of teleseismic body waves, regional seismograms, and Rayleigh wave phase shifts using two-dimensional nonlinear models of explosion sources, *AGU Geophysical Monograph 65: Explosion Source Phenomenology*, S. Taylor, H. Patton, P. Richards, editors, ISBN 0-87590-031-3, pp. 239-252
- Stevens, Jeffrey L., Norton Rimer, Heming Xu, John R. Murphy, Brian Barker, Evan Bailey, Stevens Gibbons, Conrad Lindholm, Frode Ringdal, Tormod Kvaerna, and Ivan Kitov (2004), Analysis and simulation of cavity-decoupled explosions, Final Report for USAF contract DTRA01-01-C-0069

- Stevens, J. L., H. Xu, and G. E. Baker (2006a), Analysis of Shear Wave Generation by Decoupled and Partially Coupled Explosions, Proceedings of the 28th Annual Seismic Research Review, Orlando, FL
- Stevens, Jeffrey L., G. Eli Baker, and Heming Xu (2006b), The physical basis of the explosion source and generation of regional seismic phases, Final Scientific Report for AFRL contract FA8718-04-C-0025
- Stevens, J. L., S. Gibbons, N. Rimer, H. Xu, C. Lindholm, F. Ringdal, T. Kvaerna, and J. R. Murphy (2006c), Analysis and simulation of chemical explosions in nonspherical cavities in granite, *J. Geophys. Res.*, **111**, B04306, doi:10.1029/2005JB003768.
- Stevens, J. L., H. Xu and G. Eli Baker (2009), “An upper bound on Rg to Lg scattering using modal energy conservation,” *Bull. Seism. Soc. Am.*, **99**, No. 2A, pp. 906–913, doi: 10.1785/0120080213.
- Stevens, J. L. and G. E. Baker (2009), Seismic wave generation by a non-isotropic explosion source, *J. Geophys. Res.*, in press
- Taylor, S. R., Regional seismic observations from NTS explosions, *AGU Geophysical Monograph 65: Explosion Source Phenomenology*, S. Taylor, H. Patton, P. Richards (editors) ISBN 0-87590-031-3, pp. 185-196, 1991.
- Wilkins, M. L. (1964), Calculation of Elastic-Plastic Flow, *Methods in Computational Physics*, Vol. 3: Fundamental Methods in Hydrodynamics, (Ed.) Berni Alder, 211-263
- Wortman, W. R., and G. D. McCartor (1989), Nonlinear seismic attenuation from Cowboy and other explosive sources, in *Seismic Coupling of Nuclear Explosions*, vol. 2, edited by D. B. Larson, Rep. UCRL-21086, Def. Adv. Res. Proj. Agency, Arlington, Va.
- Xu, H., J. L. Stevens, and G. E. Baker (2009), An Analysis of Shear Waves Generated by the Sterling Explosion, *J. Geophys. Res.*, **114**, B03307, doi:10.1029/2008JB005966
- Zhao, L. and D. G. Harkrider (1992), Wave fields from an off-center explosion in an embedded solid sphere, *Bull., Seismol. Soc. Am.*, **82**, 1,927–1,955